Multi-scale biomechanical study of transport phenomena in the intervertebral disc

Andrea Malandrino

Institute for Bioengineering of Catalonia

Technical University of Catalonia

Doctoral Thesis

2012

Biomedical Engineering Doctoral Program

Supervised by Dr. Damien Lacroix and Dr. Jérôme Noailly

Abstract

Intervertebral disc (IVD) degeneration is primarily involved in back pain, a morbidity that strongly affects the quality of life of individuals nowadays. Lumbar IVDs undergo stressful mechanical loads while being the largest avascular tissues in our body: Mechanical principles alone cannot unravel the intricate phenomena that occur at the cellular scale which are fundamental for the IVD regeneration. The present work aimed at coupling biomechanical and relevant molecular transport processes for disc cells to provide a mechanobiological finite element framework for a deeper understanding of degenerative processes and the planning of regenerative strategies.

Given the importance of fluid flow within the IVD, the influence of poroelastic parameters such as permeabilities and solid-phase stiffness of the IVD subtissues was explored. A continuum porohyperelastic material model was then implemented. The angles of collagen fibers embedded in the annulus fibrosus (AF) were calibrated. The osmotic pressure of the central nucleus pulposus (NP) was also taken into account. In a parallel study of the human vertebral bone, microporomechanics was used together with experimental ultrasonic tests to characterize the stiffness of the solid matrix, and to provide estimates of poroelastic coefficients. Fluid dynamics analyses and microtomographic images were combined to understand the fluid exchanges at the bone-IVD interface. The porohyperelastic model of a lumbar IVD with poroelastic vertebral layers was coupled with a IVD transport model of three solutes - oxygen, lactate and glucose - interrelated to reproduce the glycolytic IVD metabolism. With such coupling it was possible to study the effect of deformations, fluid contents, solid-phase stiffness, permeabilities, pH, cell densities of IVD subtissues and NP osmotic pressure on the solute transport. Moreover, cell death governed by glucose deprivation and lactate accumulation was included to explore the mechanical effect on cell viability.

Results showed that the stiffness of the AF had the most remarkable role on the poroelastic behavior of the IVD. The permeability of the thin cartilage endplate and the NP stiffness were also relevant. The porohyperelastic model was shown to reproduce the local AF mechanics, provided the fiber angles were calibrated regionally. Such back-calculation led to absolute values of fibers angles and to a global IVD poromechanical behavior in agreement with experiments in literature. The inclusion of osmotic pressure in the NP also led to stress values under confined compression comparable to those measured in healthy and degenerated NP specimens. For the solid bone matrix, axial and transverse stiffness coefficients found experimentally in the present work agreed with universal mass density-elasticity relationships, and combined with continuum microporomechanics provided poroelastic coefficients for undrained and drained cases. The effective permeability of the vertebral bony endplate calculated with fluid dynamics was highly correlated with the porosity measured in microtomographic images. The coupling of transport and porohyperelastic models revealed a mechanical effect acting under large volume changes and high compliance, favored by healthy rather than degenerated IVD properties. Such effect was attributed to strain-dependent diffusivities and diffusion distances and was shown to be beneficial for IVD cells due to the load-dependent increases of glucose levels. Cell density, NP osmotic pressure and porosity were the most important parameters affecting the coupled mechano-transport of metabolites. This novel study highlights the restoration of both cellular and mechanical factors and has a great potential impact for novel designs of treatments focused on tissue regeneration. It also provides methodological features that could be implemented in clinical image-based tools and improve the multiscale understanding of the human spine mechanobiology.

Ai miei genitori, Giuseppe e Giuseppina, ai miei fratelli, Mimmo e Federico e ad Asma.

Possibly the people who are trying to discover how to set up a computer to learn to play good chess, or bridge, are among those most likely to make a major contribution to the fundamental theory of evolution.

C. H. Waddington

Acknowledgements

I would like to express my sincere gratitude to those who have contributed to this thesis. First of all, I would like to thank the European Commission (DISC REGENERATION-NMP3-LA-2008-213904) and the Spanish Ministry of Science and Innovation through the pre-doctoral fellowship (FPU program AP2008-03317), for financing the research.

I would like to thank my supervisors Prof. Damien Lacroix and Dr. Jérôme Noailly for their support, patience and professionalism. With their competences and suggestions, they have highly shaped and improved the present work and continuosly stimulated my curiosity and passion for research.

I would like to thank the institutions that welcomed me from the beginnig and were I worked during my thesis: the BIBITE group at the Technical University of Catalonia (UPC), directed by Prof. Maria Pau Ginebra, and the Institute for Bioengineering of Catalonia (IBEC), directed by Prof. Josep Planell. The former and current group members of the Biomechanics and Mechanobiology group at IBEC, Andy, Clara, Martin, Ramiro, Jean Louis, Sara, Aura,Cécile, Carlos, Themis. I would also like to thank all the people from the Biomaterials for regenerative therapies at IBEC, and from the BIBITE group at UPC, Tiziano, Marta, Pablo, Nathalia, Gemma, Emiliano, Oscar, Miguel, Riccardo, Melba, Noelia. They have been office mates and friends, and all our experiences together, discussions, conference travels, jokes, parties, and laughs have really enriched my life.

I am indebted and thankful to Prof. Christian Hellmich, and to his collaborators, for their encouragement, guidance and support during my stay at the Institute for Mechanics of Materials and Structure at the Vienna University of Technology (TU Wien). For the experiments, I am also grateful for the support of Enrico Dall'Ara from the Interfacultary Laboratory for

Micro- and Nanomechanics of Biological and Biomimetical Materials at TU Wien.

I would like to thank my previous supervisors at the Istituti Ortopedici Rizzoli in Bologna, Prof. Marco Viceconti, Dr. Fulvia Taddei, Dr. Enrico Schileo and Prof. Luca Cristofolini, for transmitting me their enthusiasm for biomechanics, and all the people related with this first research experience, particularly Martino, Matteo, Caroline and Fernando.

I am grateful to all my friends of my town Noto, my friends from Bologna, and Barcelona, particularly to my roommates Andy and Tiziano, and Lucilla and Ettore. They were an important part of my daily life in Barcelona, always present and helpful.

Finally, I owe my deepest gratitude to my parents and my brothers for their continuous support, and to Asma, for her love and encouragement. I dedicate this thesis to them.

Andrea, Barcelona 2012

Contents

List of Figures

LIST OF FIGURES

List of Tables

LIST OF TABLES

Glossary

AF	Annulus fibrosus
AI	anterior inner
ALL	Anterior Longitudinal Ligament
AO	anterior outer
BEP	Bony endplate
CFD	Computational Fluid Dynamics
ECM	Extracellular matrix
FE	Finite Elements
GAGs	Glycosaminoglycan
IVD	Intervertebral disc
NP	Nucleus pulposus
PI	posterior inner
PLL	Posterior Longitudinal Ligament
PO	posterior outer
RVE	Representative Volume Element

1

Introduction

1.1 Problem and motivation

The industrialized countries are often experiencing diseases that are consequences of changes in lifestyle and increase of life expectancy. For instance, back pain is a very common pathology, influenced by the sedentarism of the activities of modern societies combined with bad postural habits (1, 2). Low back pain is highly related to IVD aging and degeneration (3). Ageing of the disc is a normal process characterized by a series of changes in its structure and function, but the cascade of events that converts normal aging of the tissue into degenerative disease is still not clear. Complications such as limited cell nutrition and other coupled cellular responses make the issue intricate and multi-factorial.

Given the enormous economic burden involved (4, 5, 6), the disc degenerative disease has been increasingly investigated. For instance, the medical research has contributed to relate a high incidence of disc degeneration with microcirculation disturbances at the vertebra-disc interface, in conditions such as smoking, vascular disease, and vascular insufficiency (7, 8). Such results, if taken together with the low cellularity and avascularity of the intervertebral joints, strongly suggest that disc maintenance is highly dependent on a proper cell nutrition. Apparently, both mechanical and cell nutritional facts are involved in disc aging and degeneration (9).

The biomechanics of spinal segments has been thoroughly explored, to answer questions such as "How do mechanical loadings affect the disc integrity?" or "Is a particular loading regime or mechanical onset the cause of disc degeneration?" (10, 11). How-

ever their intricate connections are still not clear, in terms of factor relevance, and cause-effect relationship in general. Such concerns are required to address and to speed up the cutting-edge research in the field of regeneration of the intervertebral disc, which involves innovative techniques such as tissue engineering and advanced material science. In parallel with the application of kinematics and structural/mechanical principles to the study of the spine, a massive research has been conducted to address the *local* mechanics of the human intervertebral disc. For instance, the multiscale interaction of muscle coordination, bone loading and intervertebral tissue deformation can be mandatory for the understanding of several diseases, such as spinal stenosis - where the bulging of the intervertebral disc, thickening and buckling of the ligaments, degeneration of the zygapophysial joints and narrowing of the spinal canal are involved, or the degenerative spondylolisthesis, which arises when the degenerate discs allow posterior or anterior motion of one vertebral body over the one below. Fundamental to refine locally the mechanics of the human intervertebral disc is the biphasic nature of the disc itself. In this direction, the time-dependent mechanical behavior of the disc has been studied considering explicitly the fluid movements within the disc itself. Indeed, the high amount of interstitial fluid significantly contributes to the non-linear mechanical response of the intervertebral joints and both movement and pressurization of the joint have non-negligible effects on the cell response to loading (12).

At the molecular scale, cell nutrients and waste products are intricately connected with the interstitial fluid. All together, mechanical loading, interstitial fluid, transport of biomolecule as well as cell mechanobiology are factors that need to be considered, but their interactions are too complicated or impossible to address with experiments. A way to afford such a multi-scale and multi-factorial problem is to use mathematical models.

Numerical approaches have produced *in silico* models that have been used to study the local biphasic biomechanics of the spine and intervertebral disc, the transport of biomolecules within the disc (13, 14, 15, 16, 17, 18, 19). Those models, especially when combined with experiments, increase our understanding of both disc degeneration and regeneration. However, to build an approach towards IVD cell mechanobiology, more links between tissue degeneration, cell metabolism and tissue mechanics need to be deciphered. Therefore, a multi-scale integrated model that combines as many of the mechanical and biological aspects above-mentioned, would be particularly relevant to

spine research, and, the study of the model response to mechanical and biological parameters used as inputs would be of a great interest to explore disc aging and degeneration processes.

1.2 Aims and outline of the thesis

The translation of biological and mechanical concerns relevant to the intervertebral disc - such as glycolytic metabolism and biphasic mechanics - towards an integrated predictive modeling approach is the ambition of the present thesis. The present work is aiming to apply a multi-scale and multi-factorial methodology to the study of the human spine. The main objective of the proposed approach is to relate the local mechanics of the intervertebral disc to the transport of relevant molecules (i.e. nutrients and waste products) for cell metabolism. The objective involves multi-scale techniques in order (i) to assess the load transfers from the vertebrae to the disc, (ii) to relate disc deformations with fluid movements and (iii) to link both deformations and fluid movements to molecular transport. The general aim is diluted throughout the chapters that address several aspects:

- **Chapter 2** is a brief description of the biological system studied in the present thesis, the human intervertebral disc, with a literature review focused on the IVD physico-chemical properties in healthy and degenerated states and on biphasic models used to study the disc mechanical behavior. The biphasic mixture theory and the poromechanical theory to study both solid and fluid fields in a continuum approach will be detailed. The pertinent literature in the field of biphasic IVD modeling and experiments will be reviewed.

- In **Chapter 3**, a sensitive study which considers healthy and degenerated poroelastic parameters will be described and the results will be presented and discussed.

- In **Chapter 4** the poromechanical model is refined for the two main disc subtissues: the AF and the NP by adding the non-linear elasticity (hyperelasticity) of the solid matrix. Furthermore, the AF collagen fiber description is modified following a continuum approach for fiber-reinforced composite materials, whereas

the non-negligible NP swelling characteristic is included in the constitutive material formulation. Further verifications of both mesh discretization and FE implementation in a commercial software are presented.

- **Chapter 5** is dedicated to the poroelastic model of bone material. In the line of improving the characterization of human vertebral bone, the basis of a multi-scale micromechanical model is detailed with a special focus on micro-poromechanics. An experimental work conducted at the Technical University of Vienna to characterize experimentally the extracellular bone material will be described together with the derivation of important poroelastic quantities through a combined experimental-micromechanical modeling approach. Moreover, the permeability of bone at the interface with the intervertebral disc will be evaluated by using "computational" experiments from μCT images.

- **Chapter 6** presents a new approach that couples the poromechanical model with a transport/metabolism model that considers oxygen and glucose (nutrients) and lactate (waste product) as basic biomolecules involved. The basic biological principles, the coupling procedure, the computational verification will be presented in this chapter. A sensitivity study will be presented by applying the coupled model to study healthy and degenerated IVDs mechanical and transport properties. Also, the model will be integrated with cell viability and the multiscale concern of relating mechanics to cell processes will be explored as final application.

- In **Chapter 7** the general discussion and conclusions which took shape throughout the present thesis as a whole will be summarized.

2

Physico-chemical properties of the IVD and modeling approaches

2.1 Functional anatomy of the human lumbar spine

The human *spine* or *vertebral column* usually consists of 24 articulating vertebrae and 9 fused vertebrae in the sacrum and the coccyx. The spine can be compared to an articulating flexible column anchored at the basis (sacrum), undergoing different loading combinations (compression, flexion, axial rotation, shear) while equilibrated by muscles and ligaments. The lumbar spine portion (Fig. 2.1) is fully dependent on the adjacent segments. Thus, the lumbo-sacral segment is always to be referred to a more complex functional system, i.e. vertebral column together with the pelvis (which comprises sacrum, os coxa, and coccyx). The functional unit of the spine, i.e. each motion *segment*, comprises two vertebrae with passive soft tissues in between. Within each segment it is possible to distinguish: (i) an anterior part (see for instance Fig. 2.2) which comprises two vertebrae, the interposed IVD, the longitudinal ligaments (ALL and PLL) and (ii) a posterior part which contains the pedicles, the laminae, the transverse and spinous processes, the zygapophysial (or facet) joints (for a simplified schematic view see Fig. 2.3), and the posterior ligaments[1]

[1] In a antero-posterior order, the dorsal ligaments are the supraspinous, the interspinous, the capsular ligaments and the ligamentum flavum.

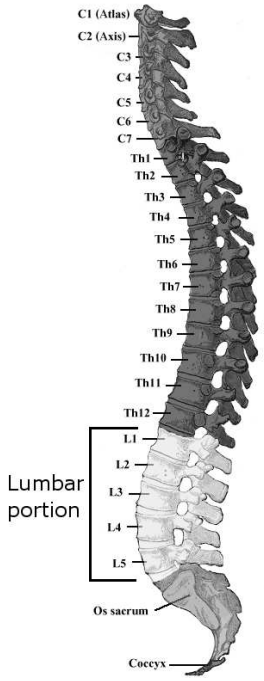

Figure 2.1: Human spine representation (figure adapted from (20)). The lumbar portion is indicated.

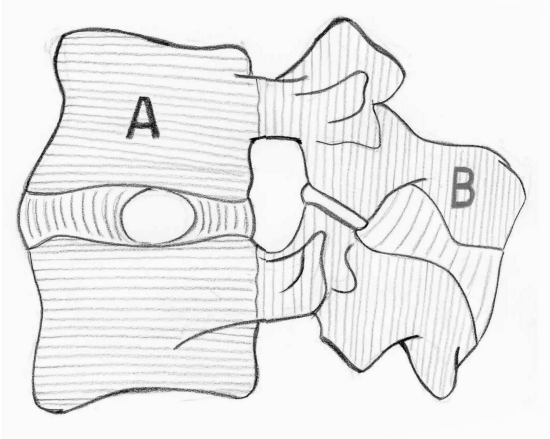

Figure 2.2: Motion segment. A: anterior part; B: posterior part (sketched from (21)).

The vertebral body can be divided into a layer of cortical bone-like as a shell surrounding a core of trabecular (or spongy) bone (Fig. 2.4). The superior (cranial) and inferior (caudal) of the cortex is called vertebral endplate or bony endplate. The characteristic of the vertebral bone at different observation scales will be detailed in Chapter

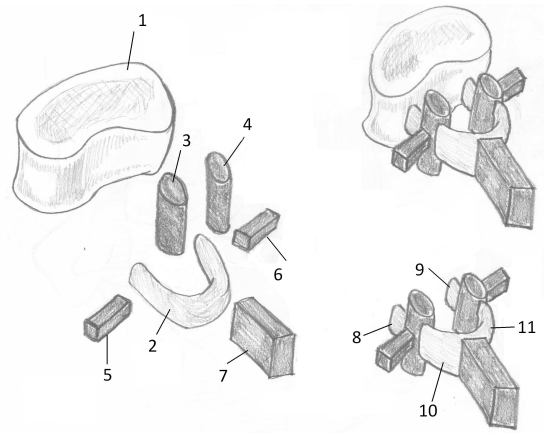

Figure 2.3: Schematic representation of the anatomical details of the vertebra: the vertebral body (1),the pedicles (8-9), the laminae (10-11), the articular processes (3-4), the transverse processes (5-6), and the spinous processes (7). The pedicle and laminea form together the vertebral arch (2) which comprises the postero-lateral wall of the spinal canal. Such a canal encompasses the spinal cord, which ends at the L2 level (sketched from (21)).

5.

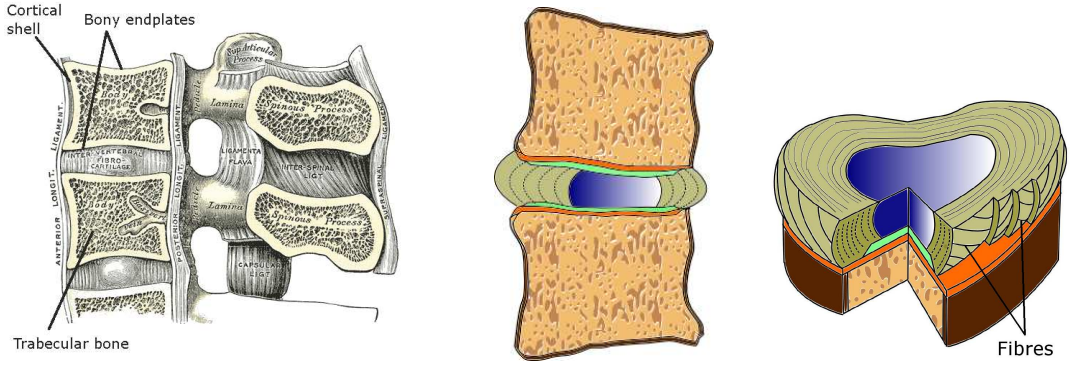

(a) (b) (c)

Figure 2.4: a): Sagittal section (image from (22))of two lumbar vertebrae with the respective ligaments (intervertebral disc is visible on the left) ; b and c): Disc organization is showed in a section with the NP (blue), AF (dark green), CEP (green). Additionally, cortical bone (dark brown), BEPs (orange) and trabecular bone (light brown) are visible.

2.2 The healthy intervertebral disc

The IVD consists of three histologically different cartilaginous subtissues (Fig. 2.4 b, c): annulus fibrosus (AF), nucleus pulposus (NP) and cartilage endplate (CEP). Together, these components form a functional unit capable of supporting and distributing high loads while controlling intervertebral motion. Relevantly, in healthy discs, compressive axial forces - the most frequent in the lumbar part - produce an increase in hydrostatic pressure in the gelatinous and highly hydrated nucleus pulposus, and this pressure is transmitted to the annulus where it generates tensile stress (23).

2.2.1 Nucleus pulposus

Disc nucleus is mainly composed by water, about 80% of its weight, proteoglycans, and collagen primarly type II in the extracellular matrix (ECM). In normal conditions, proteoglycans account for 65% of the dry weight (24) while collagen accounts for 25% of the dry weight. Proteoglycans are macromolecules containing negatively charged polysaccharide chains called glycosaminoglycans (GAGs) that have a high molecular weight, involved in binding cations (such as sodium, potassium and calcium) and retain water (osmotic effect), especially when the disc is compressed. The tissue organization provides fluidity and viscoelasticity to the structure, acting as a shock absorber, and protecting against compressive loads in IVDs.

2.2.2 Annulus fibrosus

In healthy discs, there is a clear transition between NP and the AF (Fig. 2.4b). After a reduced transition zone of wispy fibrocartilage encompassing the NP, a compositional radial gradient of the annular ring, from the NP to the external disc boundary can be observed, with a possible distinction between an inner AF and an outer AF (23, 24). On average, the human AF is mainly composed of water, 65% in total weight, proteoglycans, 20% of dry weight and collagen, 66% of of dry weight (24). Type I and II collagen fibers (36% and 64% of total collagen content, respectively (24)) are arranged primarily in concentric layers (lamellæ); the direction of the fibers in successive layers alternates from one lamella to another at angles of ±30-60 degrees (Fig. 2.4 c); at the periphery some annular fibers extend beyond the cartilage edge plate to enter the bone as Sharpey's fibers. The presence of translamellar elastin bridges has also been

observed (25) and they are thought to have a non-negligible mechanical role, although the elastin content - constant throughout the IVD - in nondegenerate tissue has been reported as the 2.0% of the dry weight (26). The microstructure of the annulus fibrosus is highly responsible for the IVD mechanical function, due to its anisotropy, given by the structure and the orientation of the collagen fibers embedded in the hydrated matrix of proteoglycans.

2.2.3 Cartilage Endplate

The cartilage endplate consists of hyaline cartilage (27). In the adult disc, the endplate thickness is lower than 1 mm, and it tends to be thinnest in the central region adjacent to the nucleus pulposus (28). The CEP is important for the mechanical function of the spine: under high compressive loads the CEP is pressed toward the vertebral bodies, and since the "normal" CEP is relatively porous, it provides one route via which metabolites can move out of the disc, the other one being through the outer annulus fibrosus. Conversely, when load is removed during relaxation/standing, the reverse mechanism provide an entrance for metabolites moving from the vertebra to the disc. A direction-dependence of the fluid flow resistance has been observed and correlated to the solid- and fluid-phase interactions occurring through the endplate route (29, 30)

2.2.4 Cells of the intervertebral discs and nutrient transport

In general, the IVD is populated by chondrocytes in the endplates, vacuolated notochordal cells (only present in immature IVD tissues) and/or chondrocyte-like cells in the NP, and fibroblast-like cells in the AF (31). Cell of the AF and transition zone originate from the mesenchyme and express synthesis of types I and II collagen and aggregating proteoglycans, which are characteristics of fibroblasts and chondrocytes (32). In humans, cells are originally derived from the notochord in the NP, which is dominated by chondrocyte-like cells as the IVD matures. The adult NP of the IVD becomes similar to hyaline cartilage, expressing markers of chondrocytes such as collagen II, collagen IX and aggrecans. (32, 33). The intervertebral disc is the largest avascular tissue in the body and presents a low cell density (4000-9000 cells/mm^3(34)) that is not homogeneous throughout the disc, being higher at the annulus edge compared to the central IVD region. Essential cell nutrients such as oxygen and glucose are supplied to the disc by the blood supply at the disc's margins (Fig. 2.5). These nutrients then

diffuse from the surrounding capillaries through the dense extracellular matrix of the disc to the cells. Metabolic waste products, such as lactate, can be removed from the tissue by the reverse route (9), since during compression, interstitial fluid flows out of the disc transporting metabolites. The nutritional environment of the cells varies throughout the disc, the oxygen concentration and pH around cells in the disc center being different from that around cells at the disc periphery. Cell density is higher closest to the nutrient supply and steeply fall with distance. Also, average cell density through the nucleus is higher in small animals where diffusional distances are small and falls exponentially with increase in disc height (9). Thus, the number of viable cell density throughout the disc seems to be regulated by nutritional constraints.

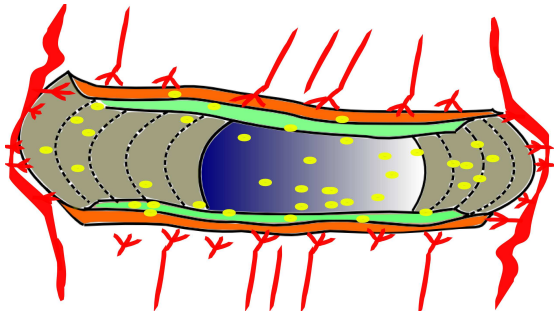

Figure 2.5: Schematic representation of the nutrient supply by vascular network at the disc margins.

2.2.5 Cellular energy metabolism within the disc

Carbohydrate assimilation in the intervertebral disc is dominated by the conversion of glucose to lactate via glycolytic pathways, a process which takes place rapidly in discs in air-saturated media, with a theoretical lactate/glucose mol-ratio of 2/1. Since oxygen consumption is low (35), the combination of rapid glycolysis and low oxygen consumption has led to the view that glycolysis is the principal source of Adenosine Triphosphate (ATP) in disc cells, in order to obtain energy: this process generate 2 mol of ATP per mol of glucose and generates lactic acid as resulting metabolite, or waste product. The overall process of glycolysis is:

$$glucose + 2NAD^+ + 2ADP + 2Pi \rightarrow 2\ pyruvate + 2NADH + 2H^+ + 2ATP + 2H_2O,$$

where NAD^+ stands for Nicotinamide Adenine Dinucleotide, a coenzyme found in all living cells that carries electrons from other molecules reducing to $NADH$, ADP is the Adenosine Diphosphate, product of ATP dephosphorylation. Pi is phosphate a group. If glycolysis were to continue indefinitely, all of the NAD^+ would be used up, and glycolysis would stop. To allow glycolysis to continue, organisms must be able to oxidize $NADH$ back to NAD^+. One method of doing this is to simply have the pyruvate do the oxidation. The pyruvate is thus converted to lactate (the conjugate base of lactic acid) in a process called lactic acid fermentation:

$$pyruvate + NADH + H^+ \rightarrow lactate + NAD^+.$$

Lactic acid fermentation happens in anaerobic conditions (36).

The cellular aerobic respiration includes other energy-conversion and metabolic pathways: Krebs cycle (or citric acid cycle) and oxidative phosphorylation, which happen following glycolysis. In particular, in oxidative phosphorylation the electrons removed from molecules are transferred to oxygen and the energy released would be used to produce ATP much more efficiently than glycolysis alone. However, oxidative phosphorylation in the IVD appears to contribute to about 15% of the total ATP formed at most (35). In the IVD, mainly low oxygen concentrations (less than 5% oxygen) are present so that oxygen consumption falls while the rate of glycolysis accelerates to maintain the energy supply. Nevertheless, it seems that a dramatic deficiency of oxygen has clear disadvantageous effects on disc cells, since proteoglycan and protein synthesis markedly decrease at very low levels of oxygen (37).

2.3 Aging and Degenerative disc disease

Back pain is a major problem challenging the workforce in industrialized countries today. It has been stated that eight out of ten people will have a problem with back pain at some time during their lives. Back pain is more likely to occur during the most productive period of most people's lives. Intervertebral disc degeneration - a condition affecting the intervertebral disc, caused by tissue weakening due to genetic and/or environmental factors - is one of the major causes of low back pain. For instance, as a consequence of disc herniation, the nerve roots are sometimes the cause of pain. In fact, pain in the lower back, or in one or both legs, or radicular symptoms other than

leg pain may occur when the nerve roots are irritated or pinched by the disc or bone spurs.

To characterize disc degeneration, several grading systems have been proposed. A common five-category grading scheme for assessing the gross morphology of midsagittal sections of the human lumbar IVD was developed by Thompson *et al.* (38). Another widely-accepted five-category system was proposed by Pfirrmann *et al.* (39) to grade reliably disc degeneration using T2-weighted magnetic resonance images. For instance, following the latter scheme, the main characteristics on which the grading is based are the differentiation of NP and AF, the signal intensity of NP and the disc height. A normal (grade I) IVD manifests a clear differentiation of AF and NP while having a hyperintense signal intensity, with horizontal dark bands. A mild degenerated (grade II) IVD has a blurred AF-NP differentiation and the signal is slightly decreased with minor irregularities. In both grade I and II, the disc height is in its normal range. A moderate degenerative disc (grade III) has no AF-NP distinction while the signal is moderately decreased with hypointense zones. The disc height can be either normal or slightly decreased. A severely degenerated IVD (grade IV) has the same characteristic as the previous III-grade but the NP signal intensity is hypointense with or without horizontal bands (black disc). Finally, the difference between grades IV and V is the presence of a collapsed disc space in grade V. Disc degenerative changes reported in the literature (loss of aggrecan (7), loss of fluid content and material properties changes (40, 41, 42) and loss of disc height (43)) are often determined using one of the previously described grading schemes, or similar. Table 2.1 reports some examples with the corresponding degenerative grades and main degenerative changes observed. In general, with aging and degeneration, the amount of NP proteoglycan composition declines, leading to a decreased osmotic water binding capacity and to a loss of compressive resistance of the whole disc. A loss of aggrecan, the primary proteoglycan of the nucleus pulposus, has been indicated as one of the earliest known degenerative changes (7). The NP progressively desiccates so that total NP water content decreases (24, 44). The nucleus becomes more fibrotic, and experiences a net loss of flexibility. Biomechanically, while the healthy nucleus behaves similar to a viscous fluid, with aging and degeneration it shows characteristics of an elastic solid, with an increase in shear modulus and a general stiffening (40).

Table 2.1: Review of studies in which degenerative changes are quantified together with the reported grading classification of the IVD degenerative state.

Study	Subtissue	Grading system	Degenerative change measured
Iatridis *et al.* (40)	NP	Thompson system (38)	Dynamic shear modulus increased with degeneration. Instantaneous shear modulus increased 3 times and water content decreased by 10% from grade I to grade IV and V.
Johannessen and Elliott (41)	NP	Thompson system (38)	Swelling pressure decreased by 73%, effective aggregate modulus decreased by 56%, permeability increases by 50%, s-GAG content decreased by 66 % and water content decreased by 6% from non-degenerated (grade<2.5) to degenerated (grade>2.5) discs.
Iatridis *et al.* (45)	AF	Thompson system (38)	Swelling pressure decreased by 61%, aggregate modulus increased by 96% and no effect on parameters describing strain-dependent permeability from non-degenerated (grades I and II) and degenerated (grades III-V)
Gu *et al.* (42)	AF	Thompson system (38)	With disc degeneration (from grade I to grade III), the radial AF permeability decreased by 13%, the axial permeability increased by 7%, the circumferential permeability increased by 41% and the water content decreased by 17%
Rodriguez *et al.* (46)	NP and CEP	Pfirrmann system (39)	Pfirrmann grade increased with age, with Grades 1, 3, and 4 being statistically different. With increasing degeneration, subchondral bone porosity increased and disc height decreased (height of Grade 3 discs was less than Grade 2, and heights of Grades 4 and 5 discs were less than Grades 2 and 3). Cell density increased by 75% while a measure of cell function (GAGs/cell) decreased by about 75% from grade I to grade V.

In the AF, both water content and osmotic pressure have also been reported to decrease (40), while tissue permeability has either been reported to stay constant (40), or increase axially and circumferentially and decrease radially (42). Annulus fibrosus can also fail mechanically with or without signs of degeneration. Annular tears, weakening and fissures are the major defects, which can eventually lead to herniations due to NP leakage.

Regarding CEP, it has been postulated that with increasing age and in some diseases, such as scoliosis, the permeability of CEP can be affected, thereby impairing the transport of both large and small solutes (9). Other relevant changes to the endplate

that take place during degeneration are related to matrix disorganization, reduction in endplate vascularity and marrow contact channels, cartilage calcification (47).

The poor IVD self-repair capability, due to low cellularity and avascularity, has put the lights on the maintenance of an adequate nutrient supply as essential condition for preventing disc degeneration (9). For instance, in the center of the nucleus in an adult human lumbar disc, cells could be as far as 7-8 mm from the nearest blood supply (35). As will be detailed in Chapter 6, nutrient availability for cells rely mainly on diffusion. It has been shown that endplate degenerative changes have an important limiting effect on diffusion, therefore pointing out that endplate disturbance could be highly responsible for lack in nutrient supply and thus accelerating the IVD degenerative cascade (48). However, recent measurements of permeability and porosity changes at the human endplate with aging and degeneration *in vitro* (46) found increased values of both permeability and porosity with degeneration, suggesting that endplate sclerosis could not be as fundamental as previously thought for disc degeneration and that other factors, such as the quality of vertebral capillaries could have a major role. Finally, among the three main IVD subtissues, it has been stated that degeneration affects more the NP and the CEP than the AF (7, 49).

2.4 Continuum Biphasic models

2.4.1 Conceptual continuum mechanics

Biological components such as organs, tissues, and cells, have been studied under the concept of deformable continuous media, wherein *continuity* deals with the geometrical evolution, i.e. two physically marked neighbors material elements must remain neighbors over time. It involves the notion of *scale* of the problem, which is defined based on the kind of information that will be extracted from the analyzed system. Certain classes of problems can be analyzed on a macroscopic scale and following, at the same time, the assumptions of microscopic physics.

Tissues and organs are complicated sub-structured materials which cannot be reproduced exactly at all scales. The continuous approach describes their macroscopic behavior analytically by averaging, homogenizing or mixing the microstructural behavior and introducing variables defined throughout the material. Such a concept is valid once it is possible to identify a “material element”. The characteristic length of

the material elements, or constituents, need to be small in comparison to the scale of the system (or mixture) so that differential calculus can be used. At the same time, the characteristic length of the constituents must be large enough so that a continuum description over the material element makes sense, i.e. a reasonable average (or mixing or homogenization) of the material properties can be made.

2.4.2 Two ways of applying the continuum concepts: the biphasic model and the poroelastic model

The IVD is a multiphasic material containing a fibrous network of collagen and elastin. The interfibrillar matrix is composed principally of varying amounts of glycosaminoglycans, interstitial fluid, salts, glycoproteins and cells. A simplification consists in considering that such material contains **two phases**: (i) a solid phase made up of structural macromolecules (namely, collagen, elastin and proteoglycans) and cells, and (ii) a fluid phase consisting in water and solutes. Starting from the concepts of continuum mechanics, two different techniques can be adopted to describe the mechanical behavior of a multiphase biological material, such as the IVD:

- The *mixture* or *biphasic* (50) model, which considers that each place in a spatial frame is occupied by two particles, solid and fluid. Under this scheme, a series of properties (density, body forces, partial stress, etc.) are assigned to each particle to derive the necessary and sufficient conditions (balance of mass, momentum, energy) that need to be satisfied for the mixture (51). As pointed out by Cowin (52), the material element, or representative volume element (RVE) under the biphasic theory is just the "Eulerian" point in the fixed spatial frame occupied by the particles.

- The *poroelastic* model considers a different kind of RVE. To quote Biot, the major contributor of the poroelastic theory (53): *"Consider a small cubic element of soil, its sides being parallel with the coordinate axes. This element is taken to be large enough compared to the size of the pores so that it may be treated as homogeneous, and at the same time small enough, compared to the scale of the macroscopic phenomena in which we are interested, so that it may be considered as infinitesimal in the mathematical treatment."*. The length scale here is much more defined: a small material element with finite dimension is now the continuum

point, many times larger than the size of the microstructure (i.e. the pore size), being thus an *average* or *homogenization* of its microstructural combination of phases.

In the mixture theory the averaging procedure is density-weighted on the basis of the density of each species in the mixture, while, in the poroelastic approach the average encompasses a finite volume of the porous solid.

2.4.2.1 Theoretical framework: the mixture theory

It is assumed that both the fluid and the solid particles are intrinsically incompressible, immiscible, and chemical inerts. Furthermore, the mixture is assumed to be isothermal. Under these assumptions, the mass balance of each phase is:

$$\frac{\partial \phi^{\alpha}}{\partial t} + \boldsymbol{\nabla} \cdot (\phi^{\alpha} \mathbf{v}^{\alpha}) = 0, \alpha = s, f \tag{2.1}$$

being ϕ^{α} the volume fraction and $\mathbf{v}^{\alpha}$ the velocity of phase α (where s=solid and f=fluid). If saturation is assumed, then

$$\phi^{s} + \phi^{f} = 1 \tag{2.2}$$

In usual applications of fluid-filled porous media, the notation

$$\phi = \phi^{f}$$

is used and ϕ is simply referred as *porosity*, while the quantity $\phi^{s} = 1 - \phi$ is called *solidity*.

Summation of the equation 2.1 gives the balance of mass of the whole mixture, i.e.:

$$\boldsymbol{\nabla} \cdot \mathbf{v}^{s} + \boldsymbol{\nabla} \cdot \left(\phi^{s} \left(\mathbf{v}^{f} - \mathbf{v}^{s} \right) \right) = 0. \tag{2.3}$$

In continuum mechanics, it is useful to describe the current state of a material element with respect to its initial state, or reference configuration (subscript "0"). A deformation gradient second-order tensor $\mathbf{F}^{s}$ is introduced and maps each infinitesimal line segment of a material element in its initial state onto the corresponding segment in the current state. The determinant of the deformation gradient tensor represents the relative solid volume change of the solid porous skeleton J^{s} from the initial to the current state

$$J^{s} = det \mathbf{F}^{s}.$$

We use the deformation gradient of the solid phase, since it characterizes entirely the the changes in both volume fractions thanks to the assumption of intrinsic incompressibility of both solid and fluid particles. Thus, since the density for the intrinsically incompressible solid phase must remain constant, it is:

$$\phi^s = \frac{\phi_0^s}{J^s}$$

and

$$\phi^f = 1 - \frac{\phi_0^s}{J^s},$$

which can be conveniently expressed only as a function of the porosity ϕ:

$$\phi = \left[1 - \frac{(1-\phi_0)}{J^s}\right] \tag{2.4}$$

Because of low mass values relative to the external forces studied, body force and inertia in soft tissue are negligible when compared to the diffusive drag forces. Under such view, the momentum balance can be written as:

$$\boldsymbol{\nabla} \cdot \boldsymbol{\sigma}^\alpha + \boldsymbol{\pi}^\alpha = 0 \tag{2.5}$$

where $\boldsymbol{\sigma}^\alpha$ is the Cauchy stress tensor and $\boldsymbol{\pi}^s$ is the diffusive momentum exchange. If we further consider the entropy inequality (not reported) (54) it follows:

$$\boldsymbol{\pi}^s = -\boldsymbol{\pi}^f = p\boldsymbol{\nabla}\phi^s + \boldsymbol{\xi}\left(\mathbf{v}^f - \mathbf{v}^s\right) \tag{2.6}$$

where $\boldsymbol{\xi}$ is the diffusive drag, which measures the frictional resistance against fluid flow through the solid matrix.

The constitutive relations can be written as

$$\boldsymbol{\sigma}^s = -\phi^s p\mathbf{I} + \boldsymbol{\sigma}^s_{eff} \tag{2.7}$$

and

$$\boldsymbol{\sigma}^f = -\phi^f p\mathbf{I} \tag{2.8}$$

The Cauchy stress has two contributions: (i) the *effective* Cauchy stress $\boldsymbol{\sigma}^s_{eff}$, entirely determined from the deformation and (ii) the *hydrostatic* or *pore* pressure p. If we substitute eq. 2.8 and eq. 2.6 into eq. 2.5 with $\alpha = f$ we obtain:

$$\boldsymbol{\nabla} p = -\frac{1}{\phi^f}\boldsymbol{\xi}\left(\mathbf{v}^f - \mathbf{v}^s\right) \tag{2.9}$$

that if $\boldsymbol{\xi}$ is assumed to be invertible, yields to

$$\mathbf{k} \cdot \boldsymbol{\nabla} p = -\phi^f \left(\mathbf{v}^f - \mathbf{v}^s \right), \tag{2.10}$$

where $\mathbf{k} = \phi^{f2} \boldsymbol{\xi}^{-1}$ is defined as the *intrinsic permeability* second-order tensor.

2.4.2.2 Theoretical framework: linear poroelasticity

In Biot poroelasticity (53) the same concept of porosity is used, but the averaging procedure is different. Among others, Simon (55), and Huyghe and Jansson (56) have shown for both linear and non-linear (finite deformation) cases that the biphasic and poroelasticity theories are equivalent when incompressible fluid and solid constituents are assumed. The differences between both theories derive only from the difference in the continuum concepts above explained. Such equivalence can be visualized by defining a series of relations between the two theories, the most important relation being that in Biot poroelasticity the displacement (and velocity) of the fluid is *relative* to the solid. To give an idea of this, we report in Table 2.2 the equivalence showed in (55) for linear poroelasticity and linear biphasic mixture theory.

Table 2.2: Example modified from (55) of the equivalence between linear biphasic mixture theory and linear poroelasticity. Equilibrium equations and Darcy's law have been omitted because they are commented in the main text.

	Poroelasticity	Biphasic	Relation
Displacement	$\mathbf{u}$, $\mathbf{w}$ (relative fluid/solid)	$\mathbf{u}^s$, $\mathbf{u}^f$	$\mathbf{u} = \mathbf{u}^s$, $\mathbf{w} = \phi(\mathbf{u}^f - \mathbf{u}^s)$
Strain-displacements	$\boldsymbol{\epsilon} = \frac{1}{2}[\boldsymbol{\nabla}\mathbf{u} + (\boldsymbol{\nabla}\mathbf{u})^T]$; $\boldsymbol{\zeta} = \frac{1}{2}[\boldsymbol{\nabla}\mathbf{w} + (\boldsymbol{\nabla}\mathbf{w})^T]$	$\boldsymbol{\epsilon}^s = \frac{1}{2}[\boldsymbol{\nabla}\mathbf{u}^s + (\boldsymbol{\nabla}\mathbf{u}^s)^T]$; $\boldsymbol{\epsilon}^f = \frac{1}{2}[\boldsymbol{\nabla}\mathbf{u}^f + (\boldsymbol{\nabla}\mathbf{u}^f)^T]$	$\boldsymbol{\epsilon} = \boldsymbol{\epsilon}^s$;$\boldsymbol{\zeta} = \phi(\boldsymbol{\epsilon}^f - \boldsymbol{\epsilon}^s)$
Stress-strain	$\boldsymbol{\sigma} = \mathbb{C} : \boldsymbol{\epsilon} - p\mathbb{I}$	$\boldsymbol{\sigma}^s = \mathbb{C}^s : \boldsymbol{\epsilon}^s - \alpha p\mathbb{I}$	$\mathbb{C} = \mathbb{C}^s$;$\alpha = \frac{\phi^s}{\phi^f}$

By summation of the solid (eq. 2.7) and fluid (eq. 2.8) stress, in poromechanics it is convenient to express the *total* stress σ as a decomposition into a pore pressure component p and the effective stress in the solid skeleton $\boldsymbol{\sigma}^s_{eff}$, which must be seen as a *drained* and *compressible* porous matter:

$$\boldsymbol{\sigma} = \boldsymbol{\sigma}^s_{eff} - p\mathbf{I} \tag{2.11}$$

To give an example specific to *linear* poroelasticity, the effective stress follows the linear (isotropic or anisotropic) elasticity form:

$$\boldsymbol{\sigma}^s_{eff} = \mathbb{C} : \boldsymbol{\epsilon} \tag{2.12}$$

where $\mathbb{C}$ is the fourth-order elasticity tensor and $\boldsymbol{\epsilon}$ is the strain tensor.

Except for the omission of the body force potential, eq. 2.10 is the classical Darcy's law used also in poroelasticity. However, a slightly different definition of permeability is used commonly in Biot poroelasticity, i.e. the intrinsic permeability is replaced with the *macroscopic* permeability

$$\mathbf{K} = \mu_f \mathbf{k} \tag{2.13}$$

where μ_f is the dynamic viscosity of the fluid.

Thus, the fluid flow behaviour follows:

$$\mathbf{q} = \phi \left(\mathbf{v}^f - \mathbf{v}^s \right) = -\frac{\mathbf{k}}{\mu_f} \boldsymbol{\nabla} p \tag{2.14}$$

2.4.3 Applications of biphasic modeling to bioengineering

Poroelasticity and mixture theory have been often used in both civil and biomedical engineering in the past decades. The first to use a linear biphasic theory was Terzaghi (57) who included both solid and fluid phases to assess the consolidation of soils, a geological process whereby the soil settles gradually due to fluid expelling. Such a view was formally and mathematically extended to tridimensional systems by Biot (53), who provided a robust theoretical framework and who is credited as the founder of the poroelasticity. Poroelasticity has been early used to model the articular cartilage (58), the cornea (59), the arterial endothelium (60) and the intervertebral disc (61). In the latter, Simon and coworkers used the Biot consolidation theory to reproduce the experimental creep and steady-state IVD responses by using a spinal motion segment FE model. They estimated a relatively low value for the permeability of the intervertebral disc and proposed that an increased permeability could be associated with degeneration. Moreover, the importance of this work rely on the pioneer implementation of the analytical Biot model by using the FE method to study the mechanical behavior of the IVD.

The mixture theory approach evolved in parallel. The theoretical framework originally provided by Truesdell and Topin (51) was applied first by Mow *et al.* (50) in 1980 to model the behavior of the articular cartilage. The theory was able to give a very accurate description of the stress and strain fields under a variety of loading conditions. The non-linearity was introduced by Holmes and Mow in 1990 (62) and the anisotropy by Almeida and Spilker in 1998 (63). Soft tissues permeability has been

found as highly strain-dependent, and different exponential constitutive laws have been proposed (64, 65) to relate the isotropic hydraulic permeability with the porosity and the volumetric strains. Multiphasic assume that a superimposition can be made in a given point of the continua. Given that the articular cartilage, as well as the intervertebral disc, are hydrated and charged soft tissues, the number of phases could be increased for instance to account for swelling phenomena occurring in articular cartilage. As such, Lai and Mow in 1991 (66) proposed a triphasic model by adding a phase (ion phase, representing both cation and anion of a single salt) that accounted for the fixed charge density and distribution. In particular, the total mixture stress presented, under this scheme, a chemical-expansion stress which derived from the assumption of charge-to-charge repulsive forces within the solid matrix. The work pioneered the analytical introduction of the well known concept of "pre-stress" in the solid matrix of proteoglycan-rich tissues that depends on the relative volume fraction of phases and is relevant to determine the overall tissue stiffness. The triphasic theory was generalized by Huyghe and Janssen (56) in 1997 as "quadriphasic theory" (solid, fluid, anions and cations phases) and extended to finite deformations. The theoretical approach provided in the two cited studies was however difficult to implement in finite element codes and in particular in commercial packages. More recently Wilson and coworkers (67) tested the hypothesis of Lanir *et al.* (68) that electrolyte flux in articular cartilage can be neglected (for being quasi instantaneous) in mechanical studies, which implies that the swelling behavior of cartilage ca be only determined by the solid deformation and the fluid flow. Thus, Wilson and colleagues described the cartilage response by adding a deformation-dependent pressure term to the standard biphasic equations. By demonstrating the reliability of such approach, they provided an alternative to the more complex mechano-electrochemical models.

2.4.4 Biphasic experiments on intervertebral disc

One of the fundamental and early recognized evidence of the biphasic nature of the IVD is the fact that its mechanical response to compressive stress involves a controlled exudation of water and generates relatively high, hydrostatic-like intradiscal pressures. Nachemson was the first that extensively investigated the pressures experienced within the IVD by inserting a pressure sensitive needle into the NP. In a series of papers, he reported the lumbar intradiscal pressures resulting from external loads on the disc,

both *in vitro* (69) and *in vivo* (70). He showed that, except from severely degenerated tissues, the stress in the NP is hydrostatic and the pressure is almost always between 1.3 and 1.5 times the applied load per unit disc area. Good correlation with the data of Nachemson were found later by Wilke and coworkers (71) except that the intradiscal pressure was less during sitting than in erect standing, which could be due to single-subject study design or to the use of different transducers (71). These studies, when seen in the context of biphasic material characterization, were used to argue that the NP can be seen as a fluid, since it experiences hydrostatic pressures. Further insight on the IVD subtissues characterization were provided by the *stress profilometry* technique, developed by McNally and Adams in 1992 (72): a pressure transducer was pulled through disc specimens along the mid-sagittal diameter, while the specimens were subjected to sustained mechanical loads. Such technique was validated (73) and showed that the values of compressive "stress" measured corresponded approximately to the average axial compressive stress acting perpendicular to the transducer membrane. Both superior-inferior (i.e., crano-caudal) and transversal (to the IVD) stress measurements were possible to measure, depending on the transducer orientation. Interestingly, the stress profilometry revealed that in the central region stress did not vary with either location or transducer orientation, suggesting that the NP behaves like a pressurized fluid. With this technique, fluid behavior was observed in the inner and middle AF in young subjects whereas steep gradients of compressive stress were measured in the outer AF. In degenerated subjects the stress profilometry has shown exaggerated changes: NP was decompressed, and large stress concentrations appeared in the AF, usually posterior to the NP (74).

It is thus intuitive that a distinction in mechanical behavior of the subtissues within the IVD would depend on the amounts and relative proportions of biochemical constituents, such as water, proteoglycans, and collagen, which vary spatially (NP, AF, CEP) and temporally (with age and degeneration). A large amount of experimental work has been done with further analyses based on the biphasic mixture theory. Such work allowed both providing biphasic mechanical properties for single IVD subtissues, and studying the relative changes with age or degeneration, as reviewed in Table 2.1. For instance, Best and coworkers (75) analyzed the compressive properties (compressive modulus, hydraulic permeability, swelling pressure) of human AF through the linear biphasic theory, and correlated regional variations within the AF subtissue with the

local biochemical composition. In the same line, but focusing more on the kinetics of fluid, thus on the permeability, is the work of Gu *et al.* (42). Iatridis and coworkers in 1996 (76) studied experimentally the human NP, and stated that the nucleus exhibited the properties of both solid and fluid material phases. They stated that the nucleus may be best characterized as a biphasic material, since it is viscous and capable of sustaining significant shear stresses, suggesting that the assumption of the nucleus pulposus as an incompressible and inviscid fluid in models may be inappropriate. Perie and coworkers (77) studied experimentally both linear and non-linear biphasic properties of both the AF and the NP, suggesting the use of confined swelling pre-test conditions and non-linear biphasic model as a proper combination to minimize the relative variance in the results under water contents representative of physiological conditions.

3

Study of the sensitivity of the physical properties of the disc

3.1 Introduction

In the previous chapter, it was stressed that fluid flow plays a key role in the form, the function and the pathologies of IVDs. For example, around 25% of the disc fluid is expelled and re-imbibed over a diurnal cycle, causing a loss and regain of around 1-2 cm in height (35). Also, loss of water and progressive solid-phase disruption alter the normal nutrition of intervertebral disc which is fundamental in the understanding of disc degeneration (41, 45, 78). Poroelastic theories implemented in finite element (FE) analyses allow investigating the fluid flow paths and the pressure distributions within the disc, to draw valuable clinical conclusions (13, 16) for the treatment of disc degeneration including the design of new regenerative strategies (79, 80). FE parametric studies can be performed to help with the design of such engineered structures, since they allow the determination of the most sensitive structural parameters. To these purposes, the inclusion of fluid flow, coupled with stress and strain field distributions is particularly relevant in a spinal segment FE model. However, the influence of each fluid and solid parameter on the poromechanical model response should be priorly explored.

Several poroelastic models of lumbar motion segments (or only IVD) have been published in the literature, compared to experimental data and partially validated (13, 16, 81, 82, 83, 84). These models have clearly shown the link between fluid flow and mechanical response within spinal segments for clinically relevant investigations, such

as the study of disc degeneration. These works included strain-dependent permeability and swelling pressure as important modeling features.

However, the clinical use of computational models depends on their validation (85). The model geometry and the choice of fluid- and solid-phase poroelastic parameters from experimental literature should be properly addressed to accurately represent a physical problem. Important parameters used in poroelasticity - hydraulic permeability, porosity, and Young's modulus - show a high experimental scatter. This is usually due to the intrinsic difficulty associated with the reproducibility of experiments involving soft tissues, the anatomical and inter-subject variability, and different measurements techniques. Moreover, highly variable phenomenology of disc degeneration makes difficult any comparison of model results with experimental measurements, in particular when liquid phase is considered. The lack of comprehensive validations for both healthy and degenerated FE poroelastic models could lead to a great uncertainty during the choice of material parameters for models. Indeed, several parametric studies have allowed drawing important guidelines about the choice of suitable linear and non-linear elastic material parameters by exploring the sensitivity of the response of FE models under different loading conditions. For instance, Rao and Dumas (86) examined the compressive behavior of a lumbo-sacral segment model, varying the non-linear material properties of each structural component. Their results pointed out that both the Young's modulus and the Poisson's ratio of the AF ground substance largely affect the IVD biomechanical response. Fagan et al. (87) examined the geometric and material non-linearities of the IVD under three physiological loadings, stating that both non-linearities, especially the material one are important to accurately predict the disc response to mechanical loads. Especially, the AF ground substance stiffness was relevant to the global disc response under all loading conditions whereas AF fibers' stiffness was relevant under torsional and flexional loads, rather than under compressive ones. However, these parametric studies have been conducted varying one parameter at a time so that the interactions among parameters have not been investigated. Although viscoelastic disc behavior was represented, both studies did not consider any explicit fluid parameter. Ng *et al.* (88) used a statistical factorial approach to determine the effect of linear elastic material properties variation on a cervical segment response. Unfortunately, the linear elastic assumption for disc sub-tissues mechanical properties did not provide any further outcome for fluid coupling.

The most evident variations of fluid and solid parameters in the human IVDs are due to degeneration, since both the solid phase of the AF and the NP ground matrices become stiffer and both local and global permeability change in all disc sub-structures (41, 45, 78). In such cases, the sensitivity of the FE model to fluid and solid parameter variations would ensure the reliability of the poromechanical representations of both healthy and degenerated IVDs. Therefore, the aim of the present work was to study the poromechanical response of a L3-L4 intervertebral disc FE model under compression, flexion and axial rotation, by varying the Young's modulus and the permeability of the main disc sub-tissues. To this purpose, a statistical factorial approach using a design of experiment (DOE) (89) was used. It was hypothesized that the permeability and stiffness values of some particular IVD sub-tissues are critical to the overall disc response whereas other parameters and sub-tissues do not influence significantly the IVD behavior.

3.2 Materials and methods

In the context of poromechanics, we considered IVD tissues as fluid-saturated porous media which models a solid fibrous matrix where fluid moves relative to the deformable solid material. The solid matter was considered as intrinsically *incompressible*. The fluid was treated as almost incompressible with a constant bulk modulus equivalent to that of water, i.e. 2200 MPa. The theoretical poromechanical framework detailed in 2.4.2.2 was used.

3.2.1 IVD base model

3.2.1.1 Model geometry

A L3-L4 intervertebral disc FE model was extracted from a previously kinematically validated model of a spinal L3-L5 segment (90, 91). The isolated disc model included two layers of elements parts of the cranial and caudal vertebral bodies attached to the disc, and included the anterior and posterior longitudinal ligaments (ALL and PLL). AF fibers reinforcement was similar to that of the original model in terms of collagen fibers material properties and orientation. Geometry and hypoelastic material properties of both fibers and ligaments are detailed in (90, 91). Material properties of all model

sub-structures, i.e. cortical shell, trabecular bone, bony endplate, AF ground matrix, NP and CEP, were changed to linear poroelastic material.

In Fig. 3.1, the sectioned model is visible, with all tissues modeled. Poroelastic solid-phase material properties are summarized in Table 3.1. Three physiological loading scenarios were simulated: (i) a disc compression of 1000 N in the crano-caudal direction, (ii) an anterior flexion and (iii) a clockwise axial rotation. The moment magnitude chosen for flexion and rotation was 7.5 Nm, according to other FE and experimental studies (90, 92). For the three load cases, the maximum load was applied linearly in 60 s, from an unloaded state. This loading ramp was chosen to study the physiologic *short-term* behavior of the disc. Common boundary conditions were used for the three load cases: (i) a zero pore pressure at the extreme cranial and caudal faces of the model in order to simulate the condition of free fluid flux through the porous vertebrae, (ii) an initial pressure of 0.2 MPa for the nucleus in the unloaded state (see results for the initial pressure value chosen), and (iii) a zero displacement of the most caudal nodes while loads were applied at the most cranial nodes. In order to assess the sensitivity of the material properties on the *long-term* viscoelastic behavior of the disc, four models with different combinations in material properties were loaded with a compressive 1000 N force during 16h. After this, the force was removed for 8 h, simulating a daily cycle. Disc height changes were compared with diurnal stature changes hypothesizing that lumbar spine is responsible for one third of the total stature loss and that all lumbar discs deform equally (93). The *in vivo* circadian experiment values from (94) were used as a reference to validate the order of magnitude of disc height changes predicted by the model and to determine how the low and high levels of parameter values (i.e. the "extreme" variations of parameter values within the range studied) affect such response.

3.2.1.2 Choice of factors and levels for statistical analysis

To investigate how the experimental variability of poroelastic material properties affects the mechanical behavior of IVD models under different load conditions, a preliminary review was performed to choose the most relevant parameters and their temporal (with aging and degeneration) and inter-study variability. First, both AF and NP stiffness were considered in terms of Young's moduli. The AF Young's moduli reported in the literature varied from 2.56 to 12.29 MPa, these extreme values corresponding to healthy and highly degenerated AF, respectively. In the case of NP, the Young's modulus

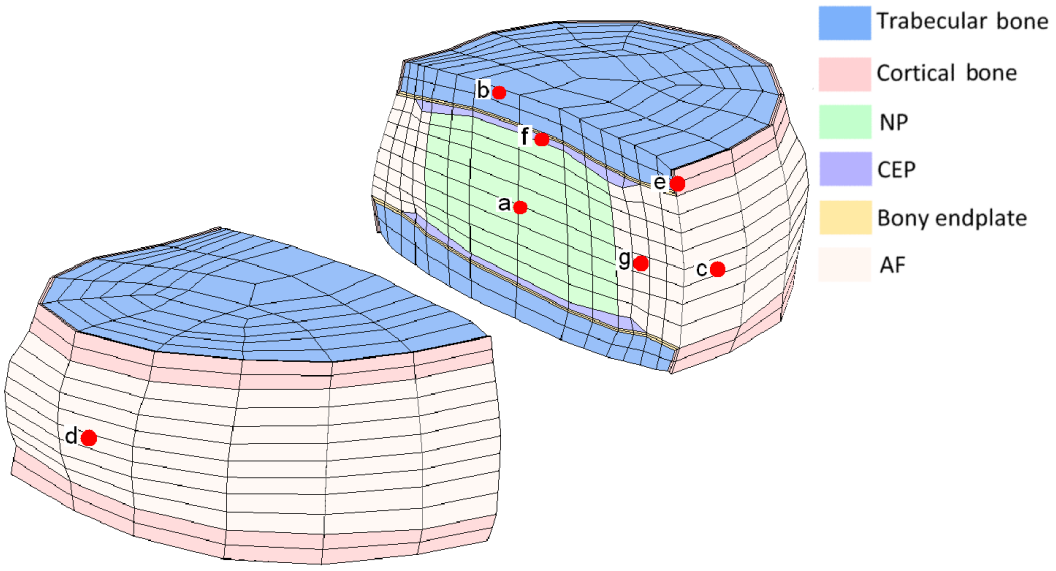

Figure 3.1: Mid-sagittal cut of the finite element model of a L3-L4 intervertebral disc with distinct element properties for the nucleus, annulus ground substance, annulus fibres, cartilage endplate, bony vertebral endplate, trabecular bone and cortical cortex. The red dots indicate where the results were calculated.

varied from 1 (healthy) to 1.66 MPa (degenerated) (45, 78). Second, permeability was considered because it is a key factor in poroelastic FE analysis, quantifying the ability of the interstitial fluid to flow within the tissues. Experimental results have shown a large variation of this parameter. Reynaud and Quinn (95) indicated that articular cartilage permeability values typically range two orders of magnitude. Nauman et al. (96) measured the intertrabecular permeability and found values ranging three orders of magnitude. Gu et al. (42) and Johannessen and Elliott (41) correlated the anisotropic AF permeability with disc degeneration. In the present study, four hydraulic permeabilities were chosen as statistical factors: the AF, the CEP, the NP and the trabecular bone permeability. This choice allowed us studying the significance of fluid-solid interactions in the whole disc, since the main regions that experience fluid exchanges (external AF and vertebrae, (29)) were included. An interval of values (levels) was assigned to each factor, based on the most used values in poroelastic IVD simulations. Table 3.2 summarizes the six parameters chosen and the ranges of variation studied.

Table 3.1: Material properties of the FE model used in this study. *Bone orthotropic linear elastic properties and bony endplate isotropic properties taken from (90). All other values taken from (13, 78). For the "varied factors" refer to Table 3.2.

Material	Elastic modulus (MPa)	Poisson's ratio	Shear modulus (MPa)	Initial porosity	Initial permeability (mm^4/N s)
Trabecular bone*	140	0.45	48	0.8	Varied factor
	140	0.176	77	0.8	Varied factor
	250	0.315	77	0.8	Varied factor
Cortical bone*	8000	0.4	2857	0.048	5
	8000	0.23	3200	0.048	5
	12000	0.35	3200	0.048	5
Bony endplate	1000	0.3	-	0.048	200000
Nucleus pulposus	Varied factor	0.17	-	0.71	Varied factor
Cartilage endplate	5	0.17	-	0.8	Varied factor
Annulus fibrosus matrix	Varied factor	0.35	-	0.57	Varied factor

3.2.2 Design of experiment statistics - screening experiment

In order to perform a statistical factorial analysis, different FE IVD models with the same geometry but different material properties were created. A full factorial analysis with two levels (values) for each of the six factors (material parameters) studied would require $2^6 = 64$ runs for each loading condition. In such a full analysis, only 6 of the 63 statistical degrees of freedom correspond to the *main* effects (89), i.e. the influence of single material parameters. For that reason and in order to limit the computational cost, a 1/4 fractional design was used. Fractional designs are expressed as l^{k-p}, where l is the number of levels of each factor investigated, k is the number of factors investigated, and p describes the size of the fraction of the full factorial used. p is also the number of generators, assignments as to which effects or interactions are confounded,

Table 3.2: Summary of combination of parameters (factors) and low and high values (levels) for the statistical factorial analysis, consisting in $2^{6-2} = 16$ runs, showing also blocks used for the strain-dependent permeability and initial pressure studies. All material properties are taken from (13, 16, 41, 42, 78, 95, 96).

Run	Blocks	TB permeability $mm^4/N\ s$	CEP permeability $mm^4/N\ s$	NP permeability $mm^4/N\ s$	AF matrix permeability $mm^4/N\ s$	NP Young's modulus MPa	AF matrix Young's modulus MPa
1	1	26800	0.0001	0.00075	0.00075	1	2.56
2	1	26800	0.0014	0.00075	0.00075	1.66	12.29
3	1	200000	0.0001	0.0014	0.00075	1	12.29
4	1	200000	0.0014	0.0014	0.00075	1.66	2.56
5	1	200000	0.0001	0.00075	0.00187	1.66	12.29
6	1	200000	0.0014	0.00075	0.00187	1	2.56
7	1	26800	0.0001	0.0014	0.00187	1.66	2.56
8	1	26800	0.0014	0.0014	0.00187	1	12.29
9	2	200000	0.0001	0.00075	0.00075	1.66	2.56
10	2	200000	0.0014	0.00075	0.00075	1	12.29
11	2	26800	0.0001	0.0014	0.00075	1.66	12.29
12	2	26800	0.0014	0.0014	0.00075	1	2.56
13	2	26800	0.0001	0.00075	0.00187	1	12.29
14	2	26800	0.0014	0.00075	0.00187	1.66	2.56
15	2	200000	0.0001	0.0014	0.00187	1	2.56
16	2	200000	0.0014	0.0014	0.00187	1.66	12.29

i.e., cannot be estimated independently of each other. A design with p generators is a $1/(lp)$ fraction of the full factorial design (89). In our case, a fractional design with $2^{6-2} = 16$ runs for each loading condition was chosen. The combination of parameters was automatically generated by the statistical software Minitab (97) corresponding to a IV resolution factorial design as indicated in Table 3.2. In a design of such resolution, main effects are unconfounded by two-factor interactions while two-factor interaction effects may be confounded with other two-factor interactions(89). Thus, the chosen resolution for this first screening experiment allowed us screening out only the main effects.

3.2.3 Effect of strain-dependent permeability and initial NP pressure

A study of the effect of strain-dependent permeability would require the modification of the definition of four (the permeabilities) of the six factors studied. It could not be considered as a factor itself but the effect of strain dependence of all four permeabili-

ties on the poromechanical responses was studied using blocks in DOE. In a factorial design of resolution IV the "blocks" feature does not affect the statistical analysis outcomes since three-way factor interactions are not considered (89). With two blocks in the design matrix (see Table 3.2), for each loading condition studied, 8 runs were performed using a constant permeability and 8 runs using a strain-dependent isotropic permeability implemented through an exponential constitutive law (16, 64, 65):

$$\mathbf{k} = k_0 \left[\frac{e\,(1+e_0)}{e_0\,(1+e)}\right]^2 \exp\left[M\left(\frac{1+e}{1+e_0}-1\right)\right]\mathbf{I}, \tag{3.1}$$

which links the permeability tensor $\mathbf{k}$ with the initial void ratio e_0 and the initial permeability k_0. Void ratio e is related with porosity ϕ via the following relation:

$$e = \frac{\phi}{1-\phi}. \tag{3.2}$$

Initial void ratio and initial porosities are reported in Table 3.1 whereas initial permeabilities are shown in Table 3.2. The block approach was also used to determine the sensitivity of the IVD response under compression to variations of the initial nuclear pressure: 0.2 MPa was applied in one block and 0.4 MPa was applied in another block (two blocks of 8 runs, see Table 3.2), which simulate different preloaded states of the disc.

3.2.4 Interdependence of factors

To assess whether an important factor is independent from the others and, to evaluate how interdependences (for example between stiffness and permeability) affects the model predictions, a full factorial analysis was performed, considering the four most significant factors resulting from the screening study in subsection 3.2.2. The four factors were: AF stiffness, AF permeability, NP stiffness and CEP permeability. The significance of factor interactions was evaluated as well as the significance of each single parameter was checked again to confirm the robustness of the preliminary study. Such analysis required $2^4 = 16$ runs and only compression was considered. Following the results of this analysis, changes in the linearity of the displacements, of the pore pressures and of the fluid velocities under CEP permeability variations were tracked using a 4-level analysis (4 runs).

3.2.5 Finite element and statistical analyses of results

Simulations were performed with MSC Marc 2007r1 (MSC Software) under large displacement and total Lagrange formulations, using a fully coupled fluid-solid FE approach. Results were analyzed at maximum loading in terms of displacements, pore pressures and fluid velocities in different locations within the model. Under compression and flexion, displacements were calculated: crano-caudally in (a) the NP center, and (b) in the cranial vertebral body, antero-posteriorly (c) medio-laterally (d) in the outer AF (red dots in Fig, 3.1). In torsion, the circumferential displacement of the antero-lateral part of the cranial superior shell (e) was calculated. Pore pressure and fluid velocities were computed in six different zones of the FE model: (a) NP center, (b) superior vertebral body, (f) superior endplate, and (c, d and g) three locations in the AF, corresponding to the external and internal AF (Fig. 3.1). Each local result under each loading condition was analyzed statistically (97) using an analysis of variance (ANOVA). The standardized effect T_I was calculated for each factor I through the following equation:

$$T_I = \frac{COEFF_I}{COEFF_{SE}} \tag{3.3}$$

where $COEFF_I$ is the estimate of the coefficients of a population regression, which corresponds to the change in the mean response due to a unit increase of one of the factors when all others remain constant. $COEFF_{SE}$ refers to the standard error of the coefficient in the regression model.

3.3 Results

Global viscoelastic disc behavior was observed in all the analyses. Fig. 3.2 shows the effect of each parameter variation and the range of predicted behaviors in comparison to experimental measurements (94): AF stiffness variations controlled the absolute value of vertical displacements reached and CEP permeability effect became evident in the 8-hours recovery phase. Velocity and pressure results were in the same range to those found experimentally and in other computational studies. Fluid velocities ranged from 1 to 5 μm/s as in the computational study of Ferguson *et al* (13) and pore pressures up to 1 MPa, as indicated in experimental (71) and computational (98) studies. Fig. 3.3 shows section plots of the considered results for the three loading conditions studied,

and for one of the models with a particular set of parameters. Fluid velocities were always lower than 1 μm/s under torsion, and under flexion and compression major velocities were computed in the cranial and caudal bony endplate regions of the model.

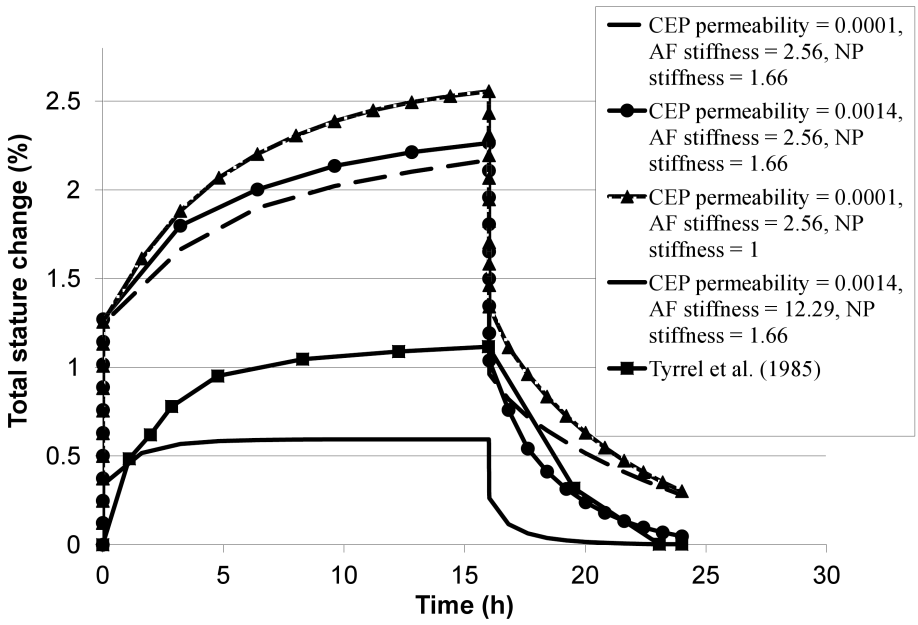

Figure 3.2: Comparison between total stature change extrapolated through FE predictions (see assumptions for extrapolations in Section 3.2.1.1) with different combination of CEP permeability, AF and NP stiffness and experimental results from literature (94).

3.3.1 ANOVA for displacement, pressures and velocities in three loading conditions

A summary of the importance of each factor is reported in Table 3.3, 3.4 and 3.5 as Standardized Effect (89) for each result at several points.

A computational experiment (with no experimental error) did not give the possibility to test a statistical hypothesis (and fix a statistical level of confidence): yet, this calculation provided a quantification of the importance of each factor. Standardized effects greater than 3.355 (i.e. the value of the (1-α/2) quantile of a t-distribution with degrees of freedom equal to the degrees of freedom for the error term) are indicated in bold in Table 3.3, 3.4 and 3.5. They correspond to a significant level with $p < 0.01$ in

Table 3.3: Results of ANOVA statistics showing the standardized effect of each factor on local displacements for each loading condition: the importance of factors is represented by the absolute value, while the negative sign indicates whether an increment of the factor produces a decrease in the response. The most important factors are in bold.

	Factors	Displacements			
		Vertical	AP bulging	ML bulging	Circumferential
Compression	AF stiffness	**10.8**	**-101.9**	**122.9**	-
	NP stiffness	**4.1**	**-5.0**	**4.9**	-
	AF permeability	-0.4	0.2	-0.5	-
	NP permeability	0.0	0.0	0.0	-
	CEP permeability	**-8.2**	0.7	-0.7	-
	TB permeability	0.0	0.0	0.1	-
Flexion	AF stiffness	**17.2**	**-37.9**	**50.5**	-
	NP stiffness	0.4	-0.2	2.6	-
	AF permeability	0.3	-1.6	1.0	-
	NP permeability	-2.0	1.6	-1.1	-
	CEP permeability	-2.4	-1.7	0.9	-
	TB permeability	-0.2	0.0	0.1	-
Torsion	AF stiffness	-	-	-	**-36.0**
	NP stiffness	-	-	-	-0.8
	AF permeability	-	-	-	-1.6
	NP permeability	-	-	-	1.7
	CEP permeability	-	-	-	-1.3
	TB permeability	-	-	-	0.0

Table 3.4: Results of ANOVA statistics showing the standardized effect of each factor on local pressures for each loading condition: the importance of factors is represented by the absolute value, while the negative sign indicates whether an increment of the factor produces a decrease in the response. The most important factors are in bold.

	Factors	Pore pressures				
		annular external	annular internal	nuclear	cartilage	trabecular bone
Compression	AF stiffness	**-4.9**	**6.1**	**-101.7**	**-16.3**	0.2
	NP stiffness	0.0	**-5.2**	**-6.2**	**-4.8**	-0.2
	AF permeability	**3.5**	-1.4	1.6	0.3	0.0
	NP permeability	0.0	0.0	-0.2	0.2	0.1
	CEP permeability	0.6	0.3	**-9.5**	**-16.9**	**3.7**
	TB permeability	0.0	0.1	-0.1	0.1	**-4.9**
Flexion	AF stiffness	**4.7**	**22.0**	**-26.4**	**-14.5**	**-3.4**
	NP stiffness	0.5	-2.2	3.4	1.8	-0.8
	AF permeability	0.6	**-4.7**	-1.3	-0.6	-0.5
	NP permeability	-1.0	1.4	1.5	0.7	0.5
	CEP permeability	1.4	-2.1	-2.2	**-4.3**	0.5
	TB permeability	0.0	0.0	0.0	-0.1	-2.4
Torsion	AF stiffness	-2.7	**-38.8**	**-36.0**	**-19.8**	-2.3
	NP stiffness	-1.2	-0.9	-2.3	-2.1	-0.3
	AF permeability	**6.3**	-3.0	-1.7	-0.8	-0.2
	NP permeability	-2.4	1.8	1.8	0.9	0.3
	CEP permeability	4.5	-1.6	**-5.3**	**-11.0**	2.9
	TB permeability	0.1	0.0	0.0	-0.1	**-6.2**

Table 3.5: Results of ANOVA statistics showing the standardized effect of each factor on local fluid velocities for each loading condition: the importance of factors is represented by the absolute value, while the negative sign indicates whether an increment of the factor produces a decrease in the response. The most important factors are in bold.

	Factors	Fluid velocity				
		annular external	annular internal	nuclear	cartilage	trabecular bone
Compression	AF stiffness	-0.7	**6.8**	**-8.2**	-2.2	-0.8
	NP stiffness	-2.8	**-5.5**	3.2	-2.0	-1.2
	AF permeability	**35.0**	**26.0**	0.1	0.1	-0.2
	NP permeability	0.0	-0.1	**6.7**	0.3	0.5
	CEP permeability	-0.1	-0.8	0.1	**51.5**	**41.7**
	TB permeability	0.5	0.9	-0.1	0.1	-2.4
Flexion	AF stiffness	-0.1	**-5.0**	**-6.6**	-3.3	**-11.5**
	NP stiffness	-1.1	-0.9	**4.1**	0.3	-1.4
	AF permeability	**7.2**	2.8	-0.1	-0.3	-1.2
	NP permeability	-0.4	0.7	**7.4**	0.4	0.9
	CEP permeability	0.6	-0.6	-0.4	**5.9**	2.5
	TB permeability	0.3	-0.3	0.0	0.4	1.5
Torsion	AF stiffness	**-4.8**	**-5.6**	**-6.8**	-3.2	**-8.6**
	NP stiffness	0.5	-0.2	3.8	-0.6	-0.8
	AF permeability	**9.3**	**11.9**	-0.2	-0.2	-0.4
	NP permeability	1.0	0.2	**10.0**	0.3	0.6
	CEP permeability	-1.1	-1.3	-0.9	**11.3**	**10.9**
	TB permeability	-0.2	0.1	0.1	0.3	0.5

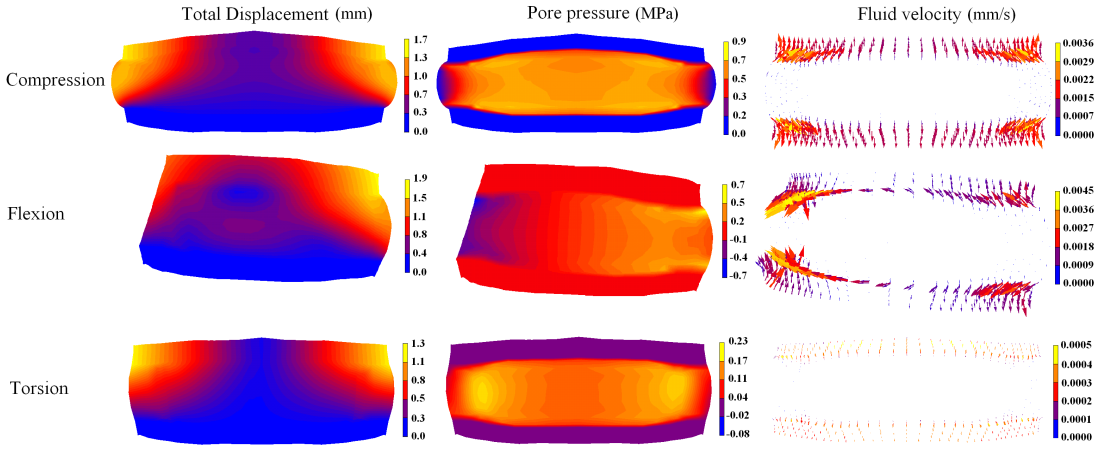

Figure 3.3: Result plots within different section planes of one of the 16 models, with the following parameter combination: TB permeability = 26800 $mm^4/N\ s$, CEP permeability = 0.0014 $mm^4/N\ s$, NP permeability = 0.00075 $mm^4/N\ s$, AF permeability = 0.00187 $mm^4/N\ s$, NP Youngs modulus = 1.66 MPa, AF Youngs modulus = 2.56 MPa. For compression and torsion mid-frontal sections are showed, whereas for flexion the cutting plane is mid-sagittal.

our computational experiment. Disc bulging was more sensitive to AF and NP Young's moduli, as shown in Fig. 3.4. In the case of flexion, bulging was sensitive only to the AF stiffness. The IVD vertical displacements under compression were sensitive to AF and NP stiffness, as well as to CEP permeability. Under torsion, the circumferential displacements of the cranial cortical shell were also sensitive to AF stiffness variations (Table 3.3). NP pore pressures calculated under compression were sensitive to AF and NP stiffness, and to CEP permeability. Both AF stiffness and CEP permeability were also significant parameters in torsion, whereas in flexion CEP permeability was significant only at the boundary NP-CEP (point "f" in Fig. 3.1). For AF pore pressures, the most significant factors under the three loading scenarios were AF stiffness and AF permeability. In torsion, CEP permeability was also significant (Fig. 3.4 and Fig. 3.5). In general, fluid velocities were sensitive to the permeability of the sub-tissue where calculations were done. In the cranial part, where the velocities ranged up to 5 μm/s, the only significant factor was CEP permeability.

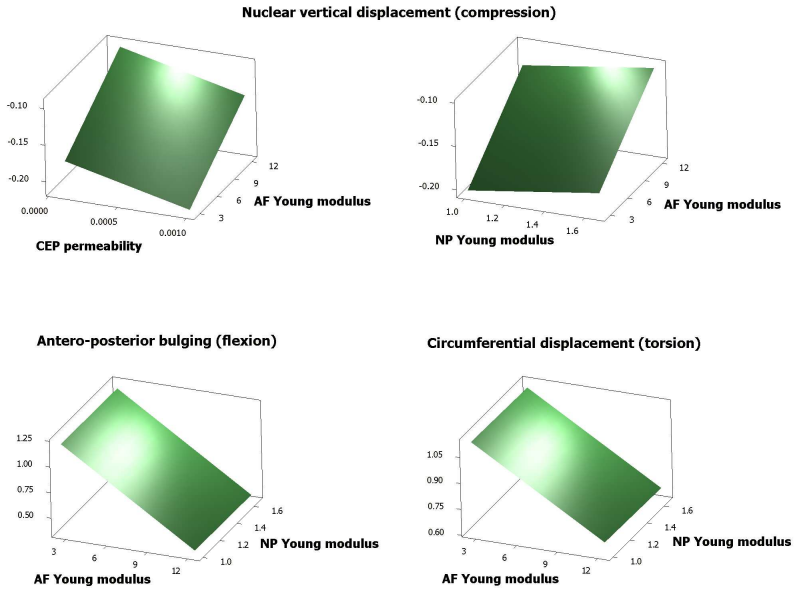

Figure 3.4: Surface plots of the displacement calculated. Upper plots show the effect of NP stiffness, AF stiffness (in MPa) and CEP permeability (in $mm^4/N\ s$) on the nuclear crano-caudal displacement (in mm). Lower plots show the effects of AF and NP stiffness for displacements under flexion and torsion.

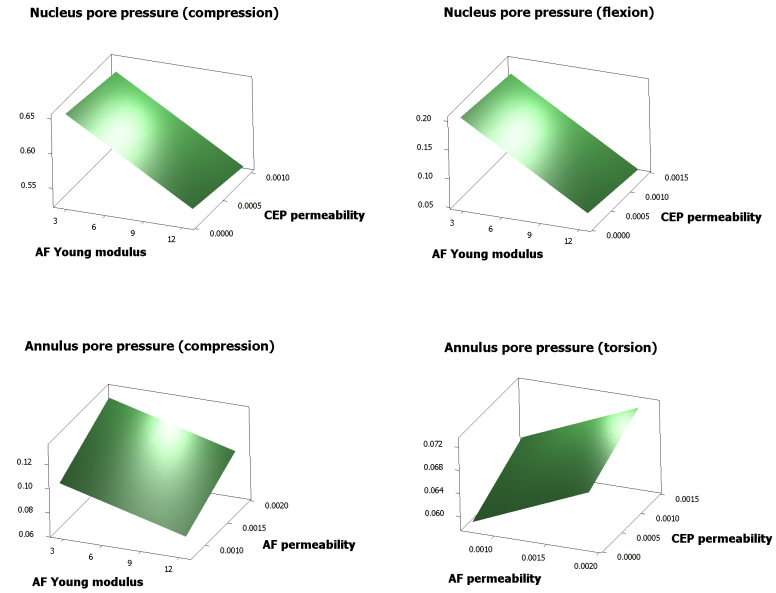

Figure 3.5: Surface plots of the pore pressures calculated. Upper plots show NP pore pressures (in MPa) whereas bottom plots show AF pore pressures. Young's moduli are in MPa, whereas permeabilities are in $mm^4/N\ s$.

3.3.2 Initial pressure and strain-dependent permeability effect

There was no statistically significant difference between blocks with different initial NP pressures: The sensitivity of the response in compression varying the six poroelastic material parameters was similar for the two values of nucleus pressure. Thus, a value of 0.2 MPa was chosen for all remaining analyses, which is reasonable compared to experimental findings (99) and simulations (17) in the literature.

The effect of strain-dependent permeability was significant in the short-term ($p < 0.01$) only for fluid velocities in the outer AF, for the three loading conditions studied. Nevertheless, in the long-term, strain-dependent permeability has been reported to have a non negligible influence (16). We confirmed this through the prediction of changes in vertical (crano-caudal) IVD displacement at the end of 10 hour of creep (1000 N compressive load) (Fig. 3.6). When strain-dependence for the permeability was simulated in all subtissues, it caused a global stiffening effect: a 25% reduction of the vertical IVD motion with respect to the vertical motion with no strain-dependence in any IVD subtissue was observed.

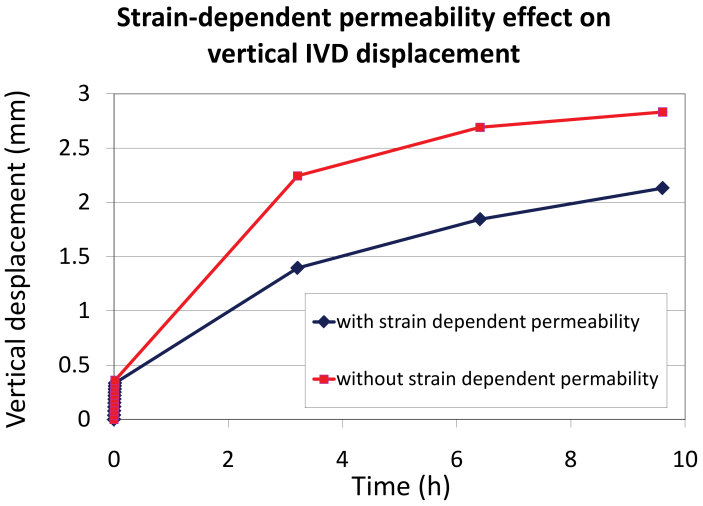

Figure 3.6: Stiffening effect of the strain-dependent permeability in the long-term creep compressive behavior: the curve in blue refers to vertical IVD displacement when strain-dependent permeability is simulated in all subtissues, while in red the case without strain-dependence is reported.

3.3.3 Interdependence of factors

No interactions among factors occurred in any case, except for the AF pore pressure calculations, where AF stiffness interacted with AF permeability (Fig. 3.7). The multi-level statistical study considering only the CEP permeability as a factor showed very little non-linearity of responses (Fig. 3.8).

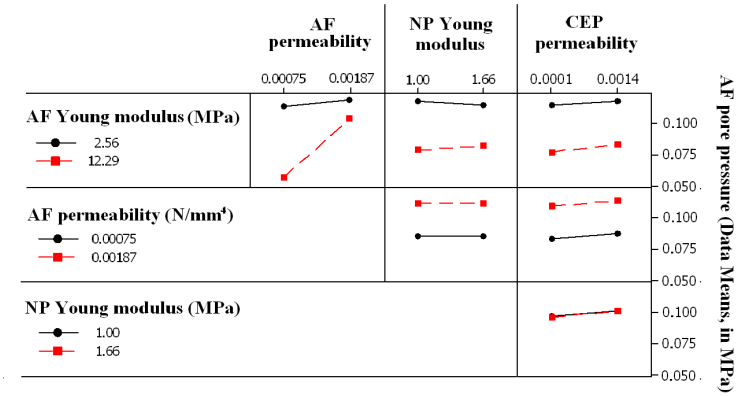

Figure 3.7: Interaction plots for pore pressure calculations in the external lateral annulus fibrosus. Parallel lines mean no interactions.

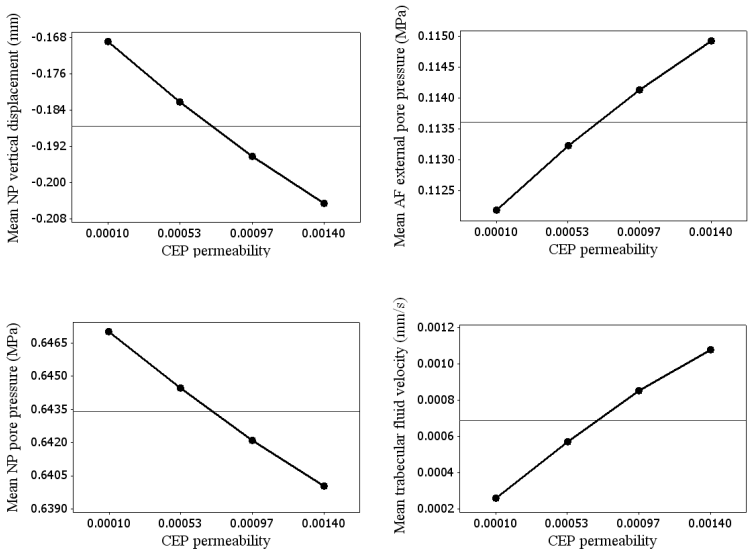

Figure 3.8: Non-linearity of the responses by varying one single factor (CEP permeability). Four responses were analyzed: nuclear and external annular pressures, vertical displacement of the nucleus and fluid velocities in the vertebral extremities.

3.4 Discussion

The aim of the present work was to use a statistical factorial approach to study the short-time poromechanical response of an intervertebral disc FE model under simple loading modes varying stiffness and permeability of the principal disc sub-tissues. Six poroelastic parameters were selected and low and high levels were identified for the values from the literature. A combination of parameter levels was implemented in a FE model of the lumbar disc and three different loading conditions were studied, compression, flexion and rotation. All loads were linearly applied up to a maximum value. Results in terms of displacements, pore pressures, and fluid velocities were statistically analyzed. AF stiffness was the factor that most significantly affected the displacements throughout the IVD, under the three loading conditions studies. Under compression, the NP stiffness and the CEP permeability played also a key role. Results of pore pressures and fluid velocities suggested a strong significance of both CEP and AF strain-dependent permeabilities. The importance of the AF stiffness is in agreement with other sensitivity studies in the literature. Ng et al. (88) found that changes in the linear elastic properties of the AF ground substance had the strongest influence on the force-displacement response of a cervical segment under three physiological loadings. Rao and Dumas (86) pointed out that the influence of the AF ground substance properties can be investigated only by modeling the annulus as a composite. They found a relevant effect of AF Young's modulus on both the vertical displacements and the bulging of the disc, and a lesser effect on the NP pressure. Sensitivity of the results in compression to the NP stiffness suggests that NP stiffening due to degeneration alters the normal behavior of the lumbar discs in terms of nucleus pressure and range of vertical motion. These results are particularly relevant to model validation, showing for example that a validation of the AF bulging - an important clinical parameter - could be achieved by varying only AF Young's modulus, without explaining other important physical phenomena. Another important finding of the present work is that CEP permeability is a determining factor for the following: (1) vertical IVD displacement during compression, (2) nucleus pressure under compression and torsion, (3) annulus pressure under torsion, and (4) fluid velocities through the vertebral bodies. In agreement with the computational findings from (100), a decreasing permeability associated with high grades of degeneration hinders disc rehydratation as confirmed by the predicted curves

of disc height recovery at the end of 24 h. Tissue permeabilities are showed to be important in fluid flow processes. This is a logic consequence of Darcy's law, used to model the fluid flow behavior, and in which the fluid velocity is proportional to the hydraulic permeability.

The first part of this study used a fractional instead of a full factorial design to screen the most significant factors. The two-ways interaction study showed that overall significance was confirmed for each single factor, even in case of significant interactions (that occurred between AF stiffness and AF permeability for example). The levels chosen for each factor were not standardized. It could be possible to run the same analysis varying low levels and high levels to a fixed percentage from a typical initial value. This would avoid that some factors, such as the NP stiffness, vary over a reduced range, whereas other factors presented variations of one order of magnitude or even more. However, levels were chosen to study the sensitivity of the IVD response under realistic variations of parameters, naturally observed in both degeneration processes and experimental measurements. Thus, the particular range of variation of a given parameter is not expected to change our results, since results are given as standardized/normalized effects. To support this fact, it can be argued for example that TB permeability was not an important factor, though ranging two orders of magnitude.

In summary, the significance of each factor was assessed using an engineering statistical approach. AF stiffness was the factor that mostly affected the displacements predicted under various loading conditions. In compression, NP stiffness and CEP permeability were also relevant. As a consequence, model assumptions for such parameters, especially AF stiffness, should be strongly verified through calibration of realistic material models. Moreover, this is the first study exploring the importance of permeability in the IVD mechanical response using a factorial analysis. Pressure and fluid velocity calculations indicated a strong significance of CEP and AF strain-dependent permeabilities for the disc under physiological loading conditions. Physically, variations of these parameter are observed due to tissue degeneration or calcification. These variations influence fluid motion inside the disc and its viscoelastic short- and long-term compressive behavior. Therefore, our sensitivity study points on the monitoring of such parameters to maintain a healthy disc physiology. Finally, the study also provides a numerical framework for experimental tests to determine which material measurement is most relevant given a specific application.

3. STUDY OF THE SENSITIVITY OF THE PHYSICAL PROPERTIES OF THE DISC

4

Development of a new porohyperelastic model of the disc accounting for regional AF and NP tissue properties

4.1 Description of the AF and NP improvements needed

In the previous chapter, we have seen how AF and NP stiffness largely affect the poromechanical response of the IVD, in various loading conditions and time scales. The objective of the present chapter is to describe, implement and test a series of improvements for the AF and NP constitutive material models. First, the non-linear behavior of the solid phase of both tissues has to be captured to accurately account for the ability of the IVD to undergo large and complex deformations (14, 101, 102). For this, a hyperelastic constitutive model was chosen and coupled to the poroelastic theory, a constitutive theory known in the literature as porohyperelasticity (103). Having in mind the equivalence between biphasic theory and poroelasticity, as detailed in section 2.4, the porohyperelastic FE implementation was also compared against a verified numerical implementation of the non-linear biphasic theory. A mesh convergence study using poroelastic material properties was performed together with a series of verification tests of the material models against experimental results in the literature.

4.1.1 AF collagen fibers

A challenge for FE models of the AF is to capture the intricate structure of the tissue and relate this structure to the specific AF mechanical function. The concentric fiber-reinforced lamellæ that build up the AF generate a strong anisotropy, due to specific collagen fiber orientation patterns. At the same time, the annulus presents significant regional differences in mechanical behavior. For instance, under a moderate circumferential strain of 5-6%, specimens in the anterior outer region of the AF experienced circumferential stresses about 10 times higher than those occurring in posterior inner specimens (104). Collagen fibres, embedded in a criss-cross pattern within the AF matrix are essential to properly mechanically stabilize the IVD and tune the functional biomechanics of the intersegmental joints. Interestingly, while this criss-cross pattern seems common to all human AF, particular regional variations in AF fibre criss-cross angles have been anatomically observed (105, 106, 107). Such particularity could be further related consistently with the regional-dependent functional biomechanics of the AF tissue (108). As a result of the several fibre angle distributions in the literature, different fibre patterns could be used as input for models. For example, following the description from Marchand and Ahmed (109), some studies did not model any particular changes of fibre angle throughout the AF, taking an average criss-cross angle value of +/-30 degrees with respect to the AF circumferential direction (16). According to the findings of Cassidy *et al.* (107), more transversal fibres in the outer than in the inner AF have been introduced in AF models (see (90), for instance). In 2001, Eberlein *et al.* (110) reported a model where experimentally-based fibre angle distributions were in perfect agreement with the micro-dissection results further described by Holzapfel *et al.* in 2005 (105), who reported an increasing fibre angle with respect to the AF transverse plane, in the tangential direction, from the anterior to the posterior annulus. More recently, Zhu *et al.* (106) investigated the lumbo-sacral annulus microstructure and reported both radial and tangential AF criss-cross angle changes. A circumferential and radial fibre angle variation was introduced by Schmidt *et al.* (111) in a FE calibration study that considered comparisons against in-vitro tests on motion segments. However, calibrated parameters involved stiffness of the AF fibres and of the ground substance while fibre angles values were unvaried. Also, such a bundle configuration has been qualitatively studied and was shown to lead to biomechanical

predictions different from those given by other AF collagen network definitions (108). In FE models of the AF, the collagen network is implemented by using fibre-reinforced elements (16, 90), as well as through continuum constitutive theories that can take into account fibre orientations and fibre stiffness-related parameters (101, 105). In particular, by using a continuum approach, Eberlein and coworkers (101) showed how varying the fibre stiffness-related parameters, two different mechanical behaviours for posterior and anterior AF regions could be reproduced. They implemented such AF constitutive behaviour in a FE model of the whole lumbar IVD, to study the functional disc mechanics. The regional variations in fibre angles were studied only circumferentially and the experimental stress-strain responses were calibrated by varying the fibre stiffness parameters. However in their study a full validation could not be obtained. Moreover, anatomical data on radial gradients in AF collagen network could be important for the mechanical stabilization of the lumbar segments under specific motions (108). Thus, we hypothesise that AF fibre angles could be considered as an unknown parameter that could be used for model calibrations. In the present study, we propose a novel model calibration procedure through the adjustment of fibre orientations in four discrete different AF regions. For this, a continuum anisotropic poro-hyperelastic approach was chosen and regional AF stress-strain measurements were reproduced by locally calibrating fibre orientation and stiffness. Calibration results in terms of fibre angles were finally implemented in a complete FE IVD model for which the predicted behaviour was compared to experimental data.

4.1.2 NP swelling pressure

The osmotic pressure largely governs the compressive behavior of the NP, due to a high concentration of fixed charges. The loss of osmotic pressure has clinically relevant consequences, such as a negative effect on the activity of disc cells (33) or on disc herniation (112). Biphasic experiments in IVD subtissues are increasingly studying as fundamental result the swelling pressure of the tested tissue, i.e. the external pressure at which the tissue neither lose nor gain water (45, 75, 77). As commented in section 2.4.3, to incorporate osmotic phenomena, triphasic and quadriphasic theories have been implemented by modeling the diffusion of ions trough the interstitial fluid and the interaction with the fixed charges. However, these models require simplified geometries and custom-made finite element solvers (56, 82), which limit their integration to full

joint articulations models. To partially simulate the swelling phenomenon through the built-in model definition fields available in commercial FE packages, some studies have simply introduced a fixed pore pressure in the range of 0.1-0.25 MPa at the external boundaries of the disc (13, 16). Another simple approach prescribed the osmotic pressure as a fixed contribution to the spherical part of the stress tensor (113), which can be implemented in FE packages via a user subroutine.

As initially hypothesized by Lanir (68), the osmosis can be incorporated in biphasic formulations by relating it to the proteoglycan fixed charge density, which depends on tissue volumetric deformations (17, 56, 67). Such an approach has been verified, yielding results comparable to those obtained by considering ionic entities as independent degrees of freedom (67). The incorporation of osmotic effects through rather simplified models and within commercially available FE programs would offer an opportunity to obtain fast and reliable solutions for complex FE simulations in spine biomechanics. Under this line, four different swelling algorithms to simulate osmotic pressure in IVD subtissues were recently explored by Galbusera and coworkers (114): (i) the fixed pore pressure at the boundaries of the model, (ii) the prescribed fixed osmotic pressure gradient throughout the disc or (iii) only in the nucleus pulposus, and (iv) the proteoglycan fixed charge density-dependent swelling model (68). They demonstrated that results predicted with the fixed boundary pore pressure and the fixed osmotic pressure in the whole disc models were nearly identical, with the only difference being that the boundary pore pressure model could not simulate differential osmotic pressures in disc regions. The swelling model offered the best potential to provide more accurate results, provided reliable values for the required coefficients and material properties are available. However, the other approaches were a good compromise between the ease of implementation and the reliability of results, especially when considering higher loads or when the focus is on global results such as spinal kinematics. In the present thesis, among all the techniques, the fixed osmotic pressure gradient in the NP was used. Therefore, a spherical (volumetric) component of the stress tensor was modified to account for the swelling mechanism. The approach, although demonstrated as a reliable option in the above-mentioned work (114), was verified in its FE implementation against confined compression experiments available in the literature.

4.2 Methods

4.2.1 AF and NP Solid-phase hyperelasticity: verification

The porohyperelasticity was implemented through the FE commercial software ABAQUS (Simulia, Providence, RI, USA) and compared to the FE implementation of the non-linear biphasic theory (54), which follows the theoretical framework detailed in 2.4, in this case with a non-linear hyperelastic constitutive law for the stress-strain relationship of the solid skeleton. In particular, a creep confined compression of a soft tissue was simulated as in the work of Almeida and coworkers (115), with no effect of collagen fibers nor swelling pressure. The original FE model of Almeida and Spilker and the type of creep experiment simulated are briefly shown in Fig. 4.1 together with the ABAQUS FE model used in our verification. It is important to underline that the work of Almeida and Spilker was chosen since it is itself a verified numerical procedure[1].

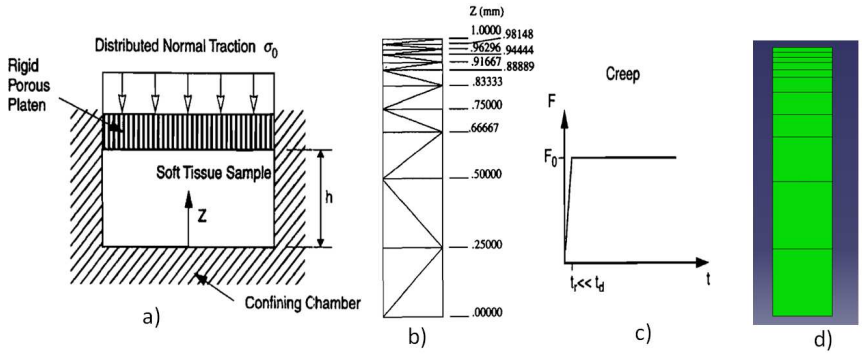

Figure 4.1: Verification procedure: a) the type of confined compression creep experiment simulated, b) FE discretization used in the original work of Almeida and Spilker (115), c) force application in the creep experiment and d) ABAQUS FE model used in the present verification.

In the work of Almeida and Spilker, the effective stress followed a non-linear constitutive law (originally proposed by Holmes and Mow (62)) that would have required a custom-made implementation in ABAQUS. In our model such a constitutive law was substituted with a compressible hyperelastic Neo-Hookean model defined through a

[1] a process that normally includes comparisons with linear solutions in the case of infinitesimal deformation, independent finite difference solutions, results from different finite element formulations and from distinct descriptions of the same problem (plane-strain, axisymmetric and 3- D models) (115)

strain energy density W from which the stress is derived[1]:

$$\boldsymbol{\sigma}_{eff} = \frac{1}{J}\frac{\partial W}{\partial \mathbf{F}}\mathbf{F}^T \tag{4.1}$$

with $J = \det \mathbf{F}$ the volumetric strain and $\mathbf{F}$ the deformation gradient tensor. The strain energy density chosen is of the Neo-Hookean type, i.e.:

$$W = \frac{G}{2}(I_1 - 3) + \frac{K}{2}(J-1)^2 \tag{4.2}$$

In the above equation, G and K are respectively the shear and bulk modulus and I_1 is the first strain invariant. For permeability, a strain-dependent function was used, similar to that of the reference work of Almeida and Spilker (54), and originally introduced by Holmes and Mow (64)

$$\mathbf{k} = \left\{ k_0 \left[\frac{(1-\phi_0)\,\phi}{\phi_0\,(1-\phi)} \right]^L \exp\left[\frac{M\left(J^2-1\right)}{2} \right] \right\} \mathbf{I} \tag{4.3}$$

In their example, Almeida and Spilker used the biphasic parameter *zero-strain compressive modulus* (or aggregate modulus at equilibrium) H_{A0} which can be converted to shear and bulk modulus in our ABAQUS implementation, following the relationships (41, 75):

$$G = \frac{H_{A0}\,(1-2\nu)}{2\,(1-\nu)} \tag{4.4}$$

$$K = \frac{H_{A0}\,(1+\nu)}{3\,(1-\nu)} \tag{4.5}$$

where ν is the Poisson's ratio.

Such parameters, in the original work of Almeida and Spilker were set to $H_{A0} = 0.31$ MPa and $\nu = 0.1$. The confined compression boundary stress on the top of the model was $\sigma_0 = 0.8 H_{A0}$ while in lateral and bottom walls a condition of zero fluid flux and displacement was imposed. The same loading rate (Fig. 4.1) was used and results were compared in terms of pore pressure over time generated at different levels.

[1] for ease of presentation, henceforward $\boldsymbol{\sigma}^s_{eff}$ has been substituted with $\boldsymbol{\sigma}_{eff}$. It should be referred to the "drained" solid skeleton. The same applies to the gradient of deformation $\mathbf{F}$

4.2.2 AF collagen fibers

To define the mechanical behavior of the AF solid phase, an anisotropic hyperelastic continuum approach was chosen. The total strain energy density function W_{AF} presents an extra term W_F in which the strain-like quantity $\bar{E}_\alpha$ is active only in two opposite orientations (101, 116), reproducing the fiber criss-cross pattern:

$$W_{AF} = W_M + W_F = \frac{G}{2}(I_1 - 3) + \frac{K}{2}(J-1)^2 + \frac{K_1}{K_2}\sum_{\alpha=1}^{2}\left\{\exp\left[K_2\left\langle\bar{E}_\alpha\right\rangle^2\right] - 1\right\} \quad (4.6)$$

In 4.6, K_1 and K_2 are fiber stiffness-related parameters. W_M represents the strain energy density of the fiber-embedding porous matrix for which a compressible Neo-Hookean model was used as in eq. 4.2. For each family of mono-oriented fibers (perfectly aligned) α, $\bar{E}_\alpha$ is defined as $\bar{E}_\alpha = \bar{I}_{4\alpha} - 1$, where $\bar{I}_{4\alpha}$ is a pseudo-invariant equal to the square of the stretch in the direction of fibers[1]. Strain-dependence for permeability was implemented following the empirical law 3.1. Again, the total stress tensor $\boldsymbol{\sigma}$ caused by external loadings was the superimposition of the porous solid stress and the fluid pore pressure, p, (see 2.11), and the porous solid stress was derived from the strain energy density function, $W = W_{AF}$ according to eq. 4.1. The fluid pore pressure was given by Darcy's law 2.14. G and K were calculated from a semi-experimental estimation of H_{A0} (77) by using the equations 4.4 and 4.5 and assuming a Poisson's ratio $\nu = 0.2$ (41).

K_1 and K_2 for the anterior and posterior AF regions were chosen from the literature by hypothesizing only circumferential stiffness changes (101). In the present study, a further radial subdivision was assumed for the calibration of fiber angles (Fig. 4.2).

Table 4.1 summarizes all the values chosen.

An experimental set-up (104) on AF tissue samples was reproduced through a FE analysis and stress-strain experimental curves were calibrated by varying only the fiber angles in the four regions considered: AI, AO, PI and PO.

4.2.3 NP swelling pressure

Within the poromechanics framework, the NP can be seen as a biphasic continuum made of a compressible porous solid fully saturated with an incompressible fluid, being

[1] as reported in (116), $\bar{I}_{4\alpha} = \mathbf{a}_{0\alpha} \otimes \mathbf{a}_{0\alpha} : \bar{\mathbf{C}}$, with $\mathbf{a}_{0\alpha}$ being the referential unit vector characterizing the fiber orientation and $\bar{\mathbf{C}}$ being the deviatoric part of the right Cauchy-Green tensor, with $\bar{\mathbf{F}} = \frac{1}{J}\mathbf{F}$ and thus $\bar{\mathbf{C}} = \bar{\mathbf{F}}^T\bar{\mathbf{F}}$

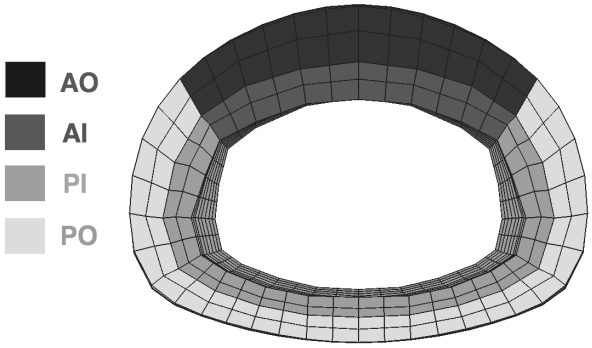

Figure 4.2: Regional subdivision of the annulus fibrosus. First letter refers to circumferential (A=anterior, P=posterior) whereas second refers to the radial one (O=outer, I=inner).

Table 4.1: Material properties for the Neo-Hookean strain energy function, strain dependent permeability (eq. 3.1), and fiber-related material properties.

	G (MPa)	K (MPa)	k_0 (m^4/N s)	e_0	M	K_1	K_2
Anterior (outer and inner)	0.28	0.37	0.2×10^{-15}	2.33	1.18	2	190
Posterior (outer and inner)	0.28	0.37	0.2×10^{-15}	2.33	1.18	5	10

the total stress in the tissue expressed according to eq. 2.11. By explicitly introducing the osmotic pressure gradient into this equation following (67, 68),the total stress is given by:

$$\boldsymbol{\sigma} = \boldsymbol{\sigma}_{eff} - (\mu_f + \Delta\Pi)\,\mathbf{I}. \tag{4.7}$$

In the above equation, the pressure is expressed as $p = \mu_f + \Delta\Pi$ where μ_f is the water chemical potential and $\Delta\Pi$ is the osmotic pressure gradient:

$$\Delta\Pi = \Pi - \Pi_{ext} \tag{4.8}$$

with Π and Π_{ext} being the internal and external osmotic pressures respectively. Introducing a new tensor $\boldsymbol{\sigma}\hat{_{eff}}$ as

$$\boldsymbol{\sigma}\hat{_{eff}} = \boldsymbol{\sigma}_{eff} - \Delta\Pi\mathbf{I}$$

Eq. 4.7 becomes:

$$\boldsymbol{\sigma} = \boldsymbol{\sigma}\hat{_{eff}} - \mu_f\mathbf{I}, \tag{4.9}$$

which has the same form as eq. 2.11 and can directly be implemented in a FE code within the standard poroelastic formulation by using a subroutine for the calculation of

$\hat{\boldsymbol{\sigma}_{eff}}$. On the one hand, μ_f is now the FE pressure solution of the poroelastic problem. Such term is dependent thus on tissue strain and on the change in water fraction. On the other hand, the osmotic effect is thus added to the solid stress matrix; such an approach has been implemented and verified by (67, 68). As pointed out in the introduction 4.1.2, the present approach has been tested and compared with the more complete approach of (67) and it has been demonstrated to provide similar results.

In the present study, a confined compression set-up (41) on NP tissue samples was reproduced with a FE model to assess the reliability of the approach presented above to model the NP swelling pressure. Degenerated and non-degenerated set of material properties were considered with biphasic parameters (zero-strain compressive modulus, constant permeabilities[1] and swelling pressure) as found in the simulated experiment. The peak stresses under confined compression were calculated and compared to the experimental ones.

4.2.4 FE IVD mesh verification

4.2.4.1 Hexahedral vs. Tetrahedral discretizations

The spatial discretization of the IVD in hexahedral elements, originally defined in the work of Noailly *et al.* (90, 91) was tested for convergence, given that a new poroelastic constitutive mechanics was adopted in the present work. The possibility of using tetrahedral elements was also explored. For both mesh types (hexa and tetra), different degrees of refinement were tested (Fig. 4.3). Individual tissue geometries remained constant for all mesh studies (subdivision on the right in Fig. 4.3). Quadratic elements were used in both tetrahedral and hexahedral meshes and convergence was tested by applying a linearly increasing compressive load of 0.5 MPa in 1 s. For these hexa-tetra mesh comparisons, linear elastic properties were used in all subtissues (Table 4.2), and no collagen fibers in the AF were considered. Results in terms of vertical displacement, bulging (i.e. transversal displacement at the external AF surface) and strain energy patterns throughout the disc were used to assess mesh convergence.

[1] strain dependence was not considered in the cited experiment

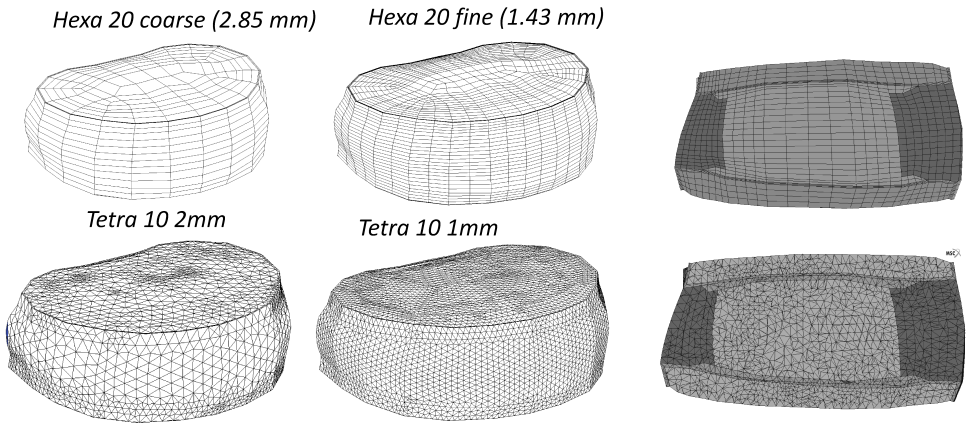

Figure 4.3: Hexahedral (top) and tetrahedral discretization used. The average element length is indicated. On the right side, the internal tissue subdivision was maintained for both hexa and tetra meshes.

Table 4.2: Material properties used for the comparisons between tetra and hexa meshes. For simplicity, orthotropy for bone was referred to the model axes (ordered in table as x/y/z), being the z axis aligned with the superior-inferior direction. All properties were taken from literature (10, 90, 111, 117).

	Young's modulus (MPa)	**Poisson's ratio**
AF	4.2	0.45
NP	3	0.49
CEP	23.8	0.4
Cortical	8000/8000/12000	0.4/0.23/0.35
Trabecular	140/140/250	0.45/0.176/0.315
Endplate Bone	12000	0.3

4.2.4.2 Iterative mesh convergence using poroelastic properties

Since finally an hexahedral discretization was chosen (see Results 4.3.2) the poroelastic properties were inserted in the hexa model and the spatial mesh resolution was iteratively increased. An optimal number of elements and average element length was determined by comparisons of: total strain energy computed in each subtissue after loading, maximum (local) fluid velocities and pore pressures. For these comparisons, no collagen fibers were considered in the AF and linear poroelastic properties for all subtissues were taken from (13) except for the AF (in (13) fibers were explicitly considered) where an average Young's modulus of 4.2 MPa was taken (117).

4.2.5 IVD model verification (with no NP swelling)

A previously developed L4-L5 intervertebral disc geometrical model was used (15, 90), with a FE discretization satisfying the above-described convergence test. A 500 N compressive creep experiment on cadaveric L4-L5 discs (92, 118) was simulated to evaluate both the global IVD mechanical response and the fiber strain values obtained with the calibrated fiber angles. The load was applied initially in approximately 10 seconds, as estimated from the in-vitro tests. The undeformed local fiber orientations were defined within the plane of the local element orientation system in which one reference axis was aligned with the circumferential direction of the AF geometry and the other one followed the lamellar crano-caudal curvature (Fig. 4.2). A large strain formulation updated automatically the fiber directions at each load increment, according to the current deformation. The nucleus pulposus (NP) was considered as a poro-hyperelastic isotropic material characterized by a Neo Hookean strain energy function, without swelling characteristic, given that in the experiment disc were tested in air (92, 118) and no osmotic effects are thus expected. Cartilage and bony endplates were treated as linear poroelastic materials (Table 4.3). Permeability for CEP was strain-dependent following eq. 4.3. The geometrical model and the finite element discretization are shown in Fig. 4.4. Calculations were done with the commercial software ABAQUS.

Table 4.3: Material properties chosen for the NP, and cartilage and bony endplates. For the endplates, G and K were calculated from reported Young's modulus and Poisson's ratio. For AF properties, refer to Table 4.1.

	G (MPa)	K (MPa)	k_0 (m^4/N s)	e_0	References	Notes
NP	0.1125	0.15	9×10^{-16}	4.88	(13, 77)	Poro-hyperelastic, strain-dependent permeability (eq. 3.1)
CEP	7.14	33.3	2.52×10^{-15}	4	(13, 84, 115)	Poroelastic, strain-dependent permeability (eq. 4.3, M =4.6, L =0.08)
BEP	3846	8333	2.68×10^{-8}	0.05	(13)	Poroelastic, constant permeability k_0

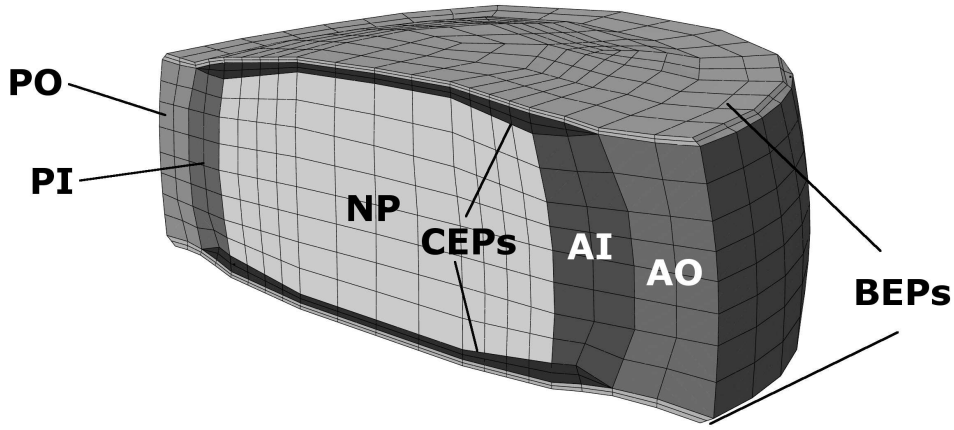

Figure 4.4: Sagittal section of the FE IVD model used for comparison with experimental data. All subtissues considered are visible.

4.3 Results

4.3.1 ABAQUS porohyperelasticity verification

The results obtained with the FE implementation of the poro-hyperelastic theory in ABAQUS and compared with those from the non-linear biphasic theory are shown in Fig. 4.5, in terms of pore pressure (normalized with the aggregate modulus) over time. Time was normalized with the diffusion time t_d of the creep experiment, which is defined to be large compared to the time of loading t_r for the creep experiment (see Fig. 4.1). Relative differences between the two implementations are lower than 5%, which is acceptable if we consider that the solid-phase strain energy function used by Almeida and Spilker was different from our non-linear Neo-Hookean one.

4.3.2 Mesh discretization

4.3.2.1 Hexahedral vs. Tetrahedral discretization

For tetra meshes, asymmetric paths of displacement results were found encompassing the external AF surface (Fig. 4.6). Such asymmetry produced displacements that could be up to 50% different from those calculated in the hexa meshes. Asymmetric results were also found in terms of strain energy density in the tetra meshes (Fig. 4.7). A

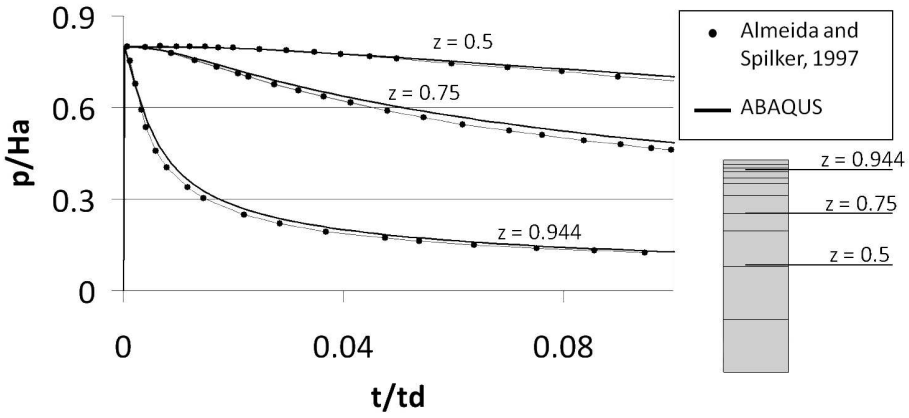

Figure 4.5: Comparison between the FE outcomes in terms of pore pressure for the ABAQUS porohyperelastic model and the non-linear biphasic model of Almeida and Spilker (115).

structured hexa mesh was thus considered as more appropiated for our "symmetric" IVD FE model and was selected for the following calculations.

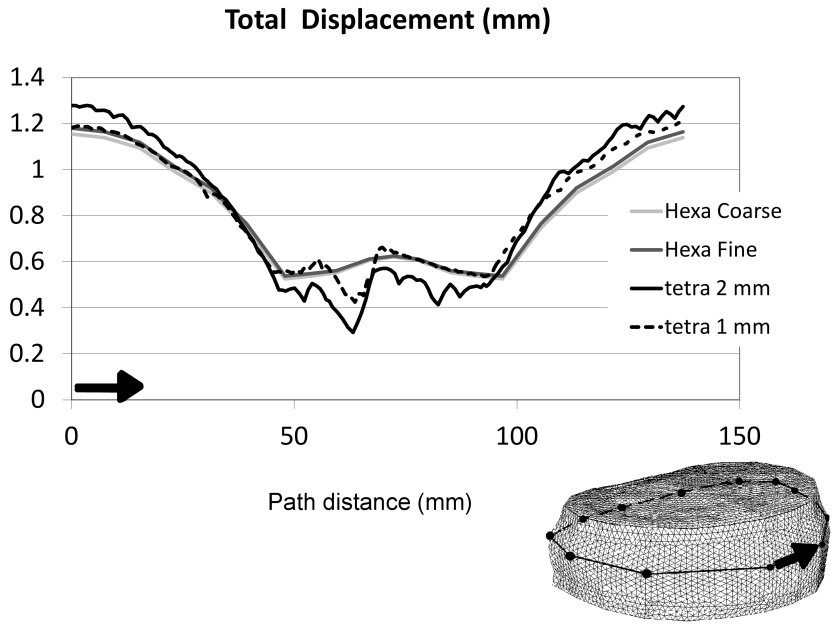

Figure 4.6: Comparison of path displacement plots (the path is showed in the inset) for the different mesh typologies and refinements. Black arrows indicate the path studied in terms of location, progression and point of origin.

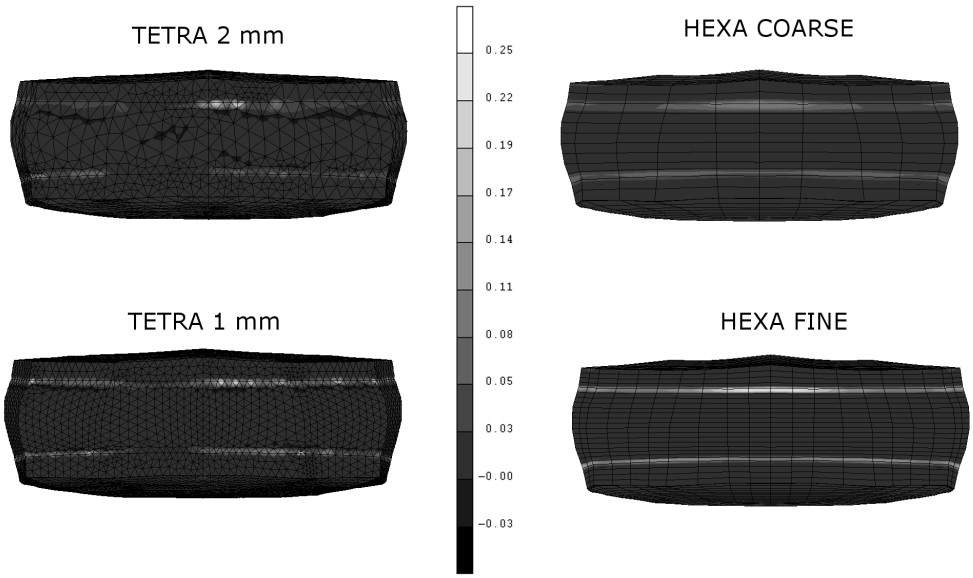

Figure 4.7: Comparisons of strain energy densities (in MPa) plots in a posterior view of the IVD, for the different mesh tested.

4.3.2.2 Iterative mesh convergence using poroelastic properties

When comparing hexahedral meshes (Hexa 20 coarse and fine, see Fig. 4.3) the strain energy density varied less than 10% for all subtissues except the CEP, where relative differences reached about 31% (Table 4.4). Also, while the maximum pore pressure varied less than 2% comparing coarse and fine IVD models, the maximum fluid velocity reached a relative difference of about 52%. Such differences in strain energy density and fluid velocities were lowered to less than 5% by refining only the mesh for the CEP in the crano-caudal direction (CEP refined in Fig. 4.8 and Table 4.4). The distribution of the velocity field and the location of the maximum value in the CEPs (Fig. 4.9) was also similar when comparing the CEP refined only in the crano-caudal direction to the CEP refined in all directions (as was in the "Hexa fine" whole IVD model).

4.3.3 Calibration of the AF mechanical behavior based on fiber angles

Curve calibrations (Fig. 4.10) resulted in the following optimal angles, calculated with respect to the circumferential axis: 28° for PO, 23° for AO, 43° for PI and 31° for

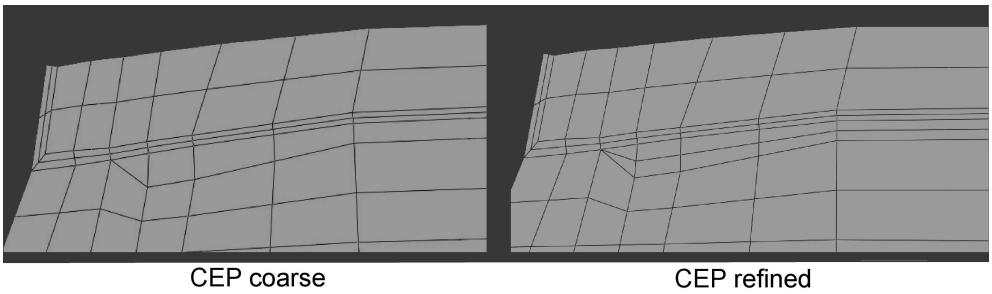

Figure 4.8: CEP refinement in the crano-caudal direction showed in an enlargement of a sagittal section.

Table 4.4: Strain energy density in Joule for each subtissue in the FE models with hexa elements used for the mesh convergence study.

	NP	AF	CEP coarse	CEP refined	BEP	Cortical bone	Trabecular bone	Whole model
Hexa coarse	35.08	106.27	5.22	7.50	9.25	2.84	4.34	165.33
Hexa fine	35.53	108.18	7.59		8.99	2.67	4.45	167.40
Relative difference	1.28%	1.76%	31.18%	1.12%	-2.86%	-6.29%	2.47%	1.23%

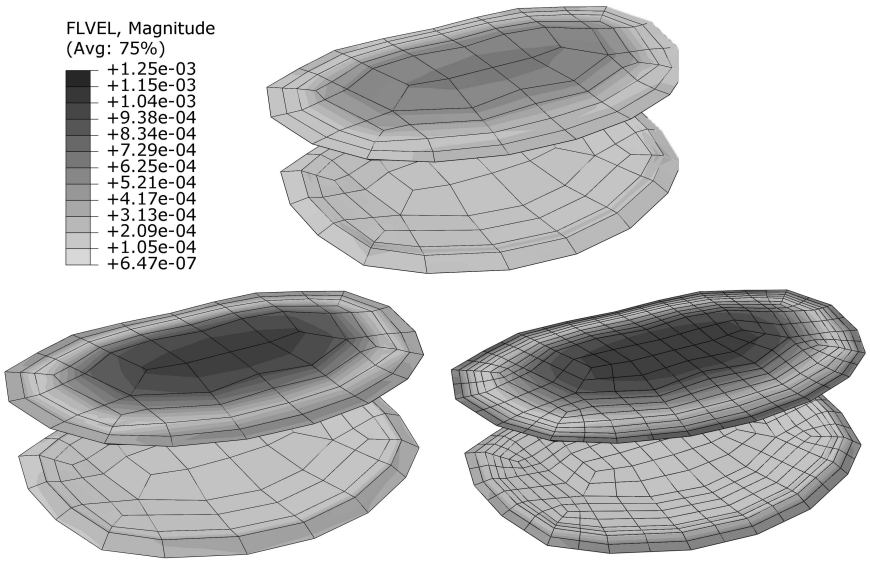

Figure 4.9: Distribution of fluid velocity field in the FE models with progressive CEP refinement. Velocities are in mm/s.

AI. Fig. 4.11 reports the average angle values compared to anatomical measurements where only radial (107) and circumferential (105) variations were reported, respectively. Fibers 31% more transversal in the outer region with respect to the inner one were predicted, against 37% found in Cassidy *et al.* (107) (Fig. 4.11a). Also, fibers 24% more transversal in the anterior region with respect to the posterior one were computed against 50% found in Holzapfel *et al.* (105) (Fig. 4.11b). Averaged absolute fibre angles were within the experimental range found in (105), while an increasing underestimation of absolute fibre angles from outer to inner was observed when comparing to (107).

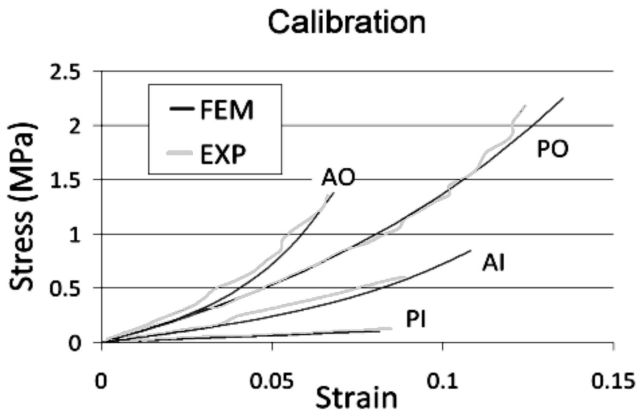

Figure 4.10: Calibration of stress-strain curves with experimental data from literature (104).

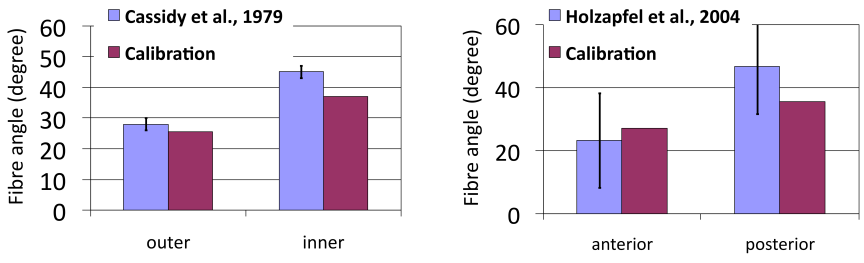

(a) (b)

Figure 4.11: Averaged data for the regional variations in fibre angles resulting from calibration, comparison with two patterns: (a) radial (107) and (b) circumferential (105).

4.3.4 NP swelling model verification

Simulation results in terms of peak compressive stresses showed a good agreement with the experimental data from (41). The computed peak stresses were within the experimental range while being 12% and 13% lower than the reported experimental values for degenerated and non degenerated specimens, respectively (Fig. 4.12).

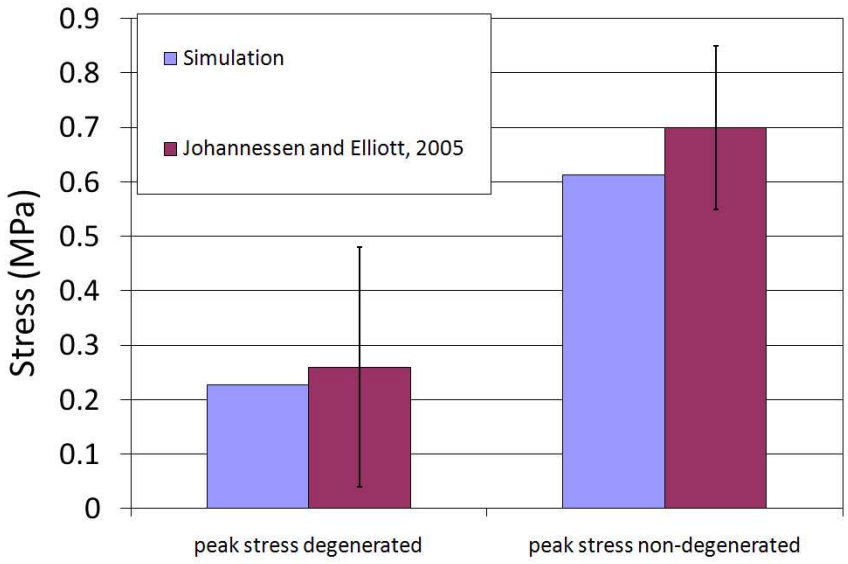

Figure 4.12: Peak compressive stresses comparison with confined experiments in literature (41).

4.3.5 Results in terms of global IVD poroelastic response

Fig. 4.13 shows the disc height changes (a) and NP intradiscal pressure (b) predictions compared to literature experimental data (92) measured during a creep period of 15 minutes under a compressive force of 500 N. At the end of such a period, the disc height change was overestimated by 5.1% and the NP intradiscal pressure was underestimated by 15.4%, compared to the average experimental values. Nevertheless, both computed height change and intradiscal pressure were within the experimental ranges reported. With the same absolute value of compressive force, maximum surface strains computed in the collagen fibre direction were 6% in the postero-lateral region of the AF, against 6.7% reported in literature for intervertebral disc with all posterior bony structures and

ligaments removed (118).

Fig. 4.14 shows the comparison of bulging results predicted with our whole-disc model against results obtained experimentally by Heuer *et al.* (92). The model predicted a bulging of 1-1.3 mm in the anterior region after load application, which increased about 20% after 15 min creep. In the posterior region, initial bulging was 1.5-1.6 mm, increasing about 10 % after 16 min. In the experiment, initial anterior bugling was 1-1.25 mm while posterior one was 0.25-0.5 mm. The increase in the anterior region after 15 min was negligible, while in the posterior was about 24%.

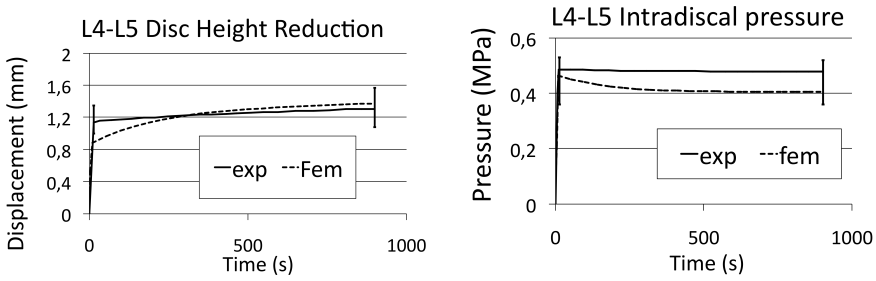

(a) (b)

Figure 4.13: FE model results with AF regional properties derived from the regional fiber angle differences in terms of (a) disc height reduction and (b) NP intradiscal pressure, and comparison with experimental values from literature (92).

4.4 Discussion

A porohyperelastic constitutive model for the AF and the NP has been implemented. The FE solution of the constitutive equation has been compared to verified biphasic FE numerical procedures. The commercial software ABAQUS was demonstrated to provide a reliable FE solution of the constitutive laws chosen. Also, a mesh convergence study was performed to further ensure the reliability of the model predictions. The porohyperelastic laws have been further specialized for the NP and AF subtissues. In the NP, given the high proteoglycan concentration, the swelling behavior has been included as a constant volumetric stress. In the AF, given the high concentration of collagen and the high level of fiber organization, a mathematical modification of the porohyperelastic continuum has been included to reproduce the strengthening effect

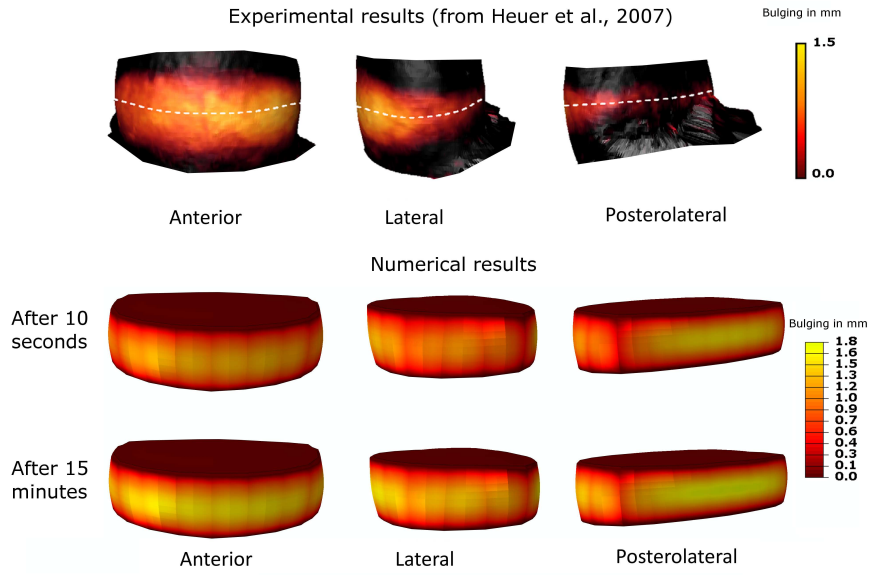

Figure 4.14: Comparison of predicted bulging displacements against experimental results (92).

of fibers. Both AF and NP constitutive laws have been verified against independent experimental results.

The mesh convergence study showed that in regions where the fluid velocities are higher as in the CEP (see Chapter 3 or (13)), the mesh should be enough refined in the direction of fluid flow. The refinement performed in the present study in the cranocaudal direction was verified in compression, but could need further explorations for other load cases. However, since the present work is meant to use the porohyperelastic model for compressive loading cases, no additional refinements were explored at this time.

Regarding the AF fibers, results demonstrated that it is possible to follow the AF regional mechanics by regional calibration of fiber orientations, while maintaining the embedding matrix properties constant throughout the AF. The results in terms of fiber angles were in general in agreement with the collagen fiber regional patterns found in the literature (105, 107). Results also showed that radial and tangential variations in fiber angle based on experiments at the tissue level produce a satisfactory response when implemented in a whole FE disc model. Moreover, in a complete lumbar spine functional unit, the tangential fiber pattern seems intuitively adapted to resist sagittal flexion, but axial fibers in the posterior AF are also thought to be adapted to the mechanical action of the facet joints under axial rotation (108). Radial orientation gradients could be explained considering a better mechanical response when intersegmental shear deformations are involved in axial rotation (transversal shear), for example. Under sagittal extension, it has also been suggested that the mechanical reinforcement of the thick anterior AF of the lower lumbar spine could be improved with fiber radial orientation gradient because of significant axial shear deformations (108). It is worth to highlight that the values found for the fiber angles could depend on the embedding matrix material properties. Differences in AF regional mechanics could also be due to regional variation of AF matrix properties as well as swelling pre-testing conditions that affect the absolute values of the matrix parameters (77). So far, our calibration considered that all the mechanical heterogeneity through the AF is attributed to the fibers rather than to the matrix. In the future, mixed calibrations fiber-matrix should be explored. Also, bundle stiffness has been used as parameter for calibration (111) of local AF mechanics, since the presence of composition-based radial variation for bundle stiffness exists in AF (119). In our model, bundle stiffness-related parameters were

taken from (101) and their variation should be fully explored in the future. Nevertheless, the present study clearly shows that fiber angle calibration is a valid tool since it allowed reproducing the non-linear stiffness of matrix plus fibers and gave realistic fiber orientation patterns that could be related with those anatomically observed. Such outcome supports former numerical explorations that suggested using particular AF fiber angle distributions to realistically improve lumbar spine model calibrations that are based on material stiffness adjustments (108).

In the present model, four fiber angle discrete regions were considered, whereas smooth gradients (i.e. a linear pattern for fiber variation) have been measured in both radial and tangential directions (105, 106, 107). Future work should include a less abrupt fiber angle changes from one region to another, by including those gradients for fiber angles throughout the AF. Our fiber configuration, when implemented in a whole-disc FE model, provided creep displacements and NP pressures that were between the experimental range (Fig. 4.13). Our model also predicted a bulging at the end of 10 seconds that increased slightly at the end of 15 minutes creep, in agreement with the experiment and the bulging displacements are comparable with the experiment, in the front and side view (Fig. 4.14). However, looking at the rear view, our model predicts high bulging, which is not confirmed experimentally. We believe that this depends on the shape of the tested motion segments and its relative position with respect to the load direction. This in turn depends on both the particular geometry and degeneration grade of the tested discs. These factors could be very different in our simulated disc. Moreover, additional in-vitro tests with different loading scenarios - especially rotational loads that stress fibers in a more significant way - were not considered for whole-disc model verification. However, well-documented time dependent data are necessary to validate a poroelastic model and are unfortunately not available for such intersegmental scenarios, to our knowledge. Since this aspect could potentially challenge our overall calibration procedure, more comparisons with the aim of a more comprehensive model validation are required in the future.

Finally, novel combined experimental-analytical techniques, such as Diffusion Magnetic Resonance Imaging (Diffusion MRI) are able to provide a spatial mapping of the distribution of fiber orientation (120). With such a technique, it could be possible to obtain *in vivo*-based fiber angles that can be used then as input of the AF anisotropic

porohyperelastic model verified in the present chapter, to include the effects of subject-specific, regional AF mechanics.

Regarding the swelling behavior of the NP, the introduction of a spherical (volumetric) component was used in the constitutive law of the solid NP phase to model the volumetric stiffening due to osmotic effects. In the present work, stress calculations were in accordance to the stress measured in independent stress relaxation tests (41). It can be thus considered that the introduction of the NP swelling as a fixed osmotic pore pressure reproduces well the macroscopic behavior of NP tissue samples. Recently, Galbusera *et al.* (114) compared distinct models to simulate osmotic effects in a lumbar disc under both free swelling and daily physiological loads: (i) a complete electrochemical biphasic swelling model with strain-dependent osmotic pressure (based on strain-dependent fixed charge density), (ii) a fixed boundary pore pressure model, and (iii) a fixed osmotic pressure model (in both the AF and NP or only in the NP). The comparisons showed that prescribing the osmotic pressure as a pore pressure at the boundaries or as a fixed osmotic pressure gradient (as in the present thesis) yielded similar results. Indeed, while the more complete electrochemical biphasic swelling model (67) can lead to more accurate results, extensive sets of measurements and mathematical fit of experimental data are required for the estimation of material parameters, e.g. osmotic coefficients, fixed charge densities, etc., which may introduce additional errors and uncertainties. Furthermore, as already mentioned in section 4.1.2, in (114), Galbusera and colleagues further demonstrated that approaches such as fixed boundary pore pressure or fixed osmotic pressure (in the AF and NP) or only in the NP (as the present thesis) can be conveniently used when large physiological loads, daily activities or assessment of implants are simulated, or in when the kinematics of the spine is the intended result. These approaches were thus pointed out as a good compromise between the ease of implementation and the reliability of results at a macroscopic scale.

The complete IVD FE model was tested under compression and compared to independent experiments. It has to be noted that the NP swelling pressure was not activated in such comparison. This is because the IVDs in the reference experiment were tested in air (92), thus osmotic effects were considered to be negligible in our study. Also, the prediction of disc height reduction at the beginning of the creep load (see Fig. 4.13a) tended to slightly differ from measured values. However, experiments were driven with

cadaveric specimens where blood clotting may have blocked the main fluid pathway at the vertebral endplate, affecting the transient behavior of the specimen.

In conclusion, a porohyperlastic FE implementation was shown to be appropriate to describe the biphasic nature of IVD main subtissues. Globally, the NP and AF porohyperelastic modeling together with regional fiber angles variations is able to reproduce the regional AF and NP tissue mechanics and lead to a satisfactory global mechanical behavior when implemented in a complete IVD FE model. Furthermore, calibration of AF fiber criss-cross angle distributions should be considered as an effective tool to reproduce the biomechanical behavior of both the AF and a lumbar spine segment in a realistic way, which can be further improved in the future by using imaging-based techniques for the determination of fiber distributions.

4. DEVELOPMENT OF A NEW POROHYPERELASTIC MODEL OF THE DISC ACCOUNTING FOR REGIONAL AF AND NP TISSUE PROPERTIES

5

Micromechanical study of the vertebral bone poroelasticity

5.1 Motivation

In the previous chapters, the importance of fluid exchanges between the intervertebral discs and vertebrae for the IVD mechanical response has emerged. CEP permeability influenced both the short-term vertical motion and the long-term vertical recovery, therefore demonstrating its fundamental role in global IVD mechanics (15, 29). Additionally to the fluid exchanges, the load sharing between discs and vertebrae has also been addressed in the past as fundamental for the study of the human spine: for instance, in case of IVDs degeneration, the alteration of local stress shielding involving (i) redistribution of bone mass, (ii) reduction of trabecular architecture anteriorly and (iii) increasing in bone risk of fracture have been pointed out (121). Also, other pathologies such as *developmental spondylolisthesis* - the anterior or posterior displacement of a vertebra in the lumbar region - are directly related with bone loading. A better understanding of the micromechanical load transfer is necessary in order to understand the different stages of the disease and how damage in the discs affects adjacent vertebrae. For realistic simulations of the human spine, it thus appears as relevant to increase our knowledge on *local* IVD-vertebrae load sharing, involving both solid and fluid phases. The present chapter is dedicated to a poro-micromechanical focus on vertebral bone. Three main studies were carried out during a stay at the Institute for Mechanics of Materials and Structures of the Vienna University of Technology (TU Wien), Vienna,

Austria:

- an experimental characterization of the human vertebral bone anisotropic elasticity
- a micromechanical-based interpretation of such experiments with the aim of fully characterize the poroelasticity of vertebral bone
- an additional study involving computational fluid dynamics (CFD) simulations to understand the role of bone microstructure at the bony endplates when looking at the fluid exchanges between discs and vertebrae.

5.2 Introduction

5.2.1 A multiscale view of bone material

Bone is a complex multiscale composite material. It is mainly formed by assembly - at different observation scales - of water, organic phases (collagen and cells and other organic matter) and inorganic mineral phase (crystals of hydroxyapatite). In the following description, we refer to the literature review of Fristch *et al.* (122) based on the widely accepted hierarchical multiscale schematization of Katz *et al.* (123) (see Fig. 5.1). At a scale of few nanometers, collagen molecules assemble with intramolecular water and form a matrix called wet collagen. The resulting wet collagen coexists and interpenetrates - at a superior-order scale of hundred of nanometers - with crystal agglomerations of hydroxyapatite, forming a new material assembly called mineralized collagen fiber. At the same scale, a mineral foam, or extrafibrillar space exists, made up of a mixture of hydroxyapatite crystals and intercristalline space. Mineralized collagen fibers and extrafibrillar space are the main constituents of a superior-order scale (few micrometers) material, which is commonly named as the extracellular bone material, or ultrastructure. The ultrastructure has two different types of porosity, i. e. the lacuno-canalicular and the trabecular one, and, depending on the porosity type, it forms what we commonly distinguish as cortical and trabecular bone, at the scale of milli- to centi-meters (bone organ level).

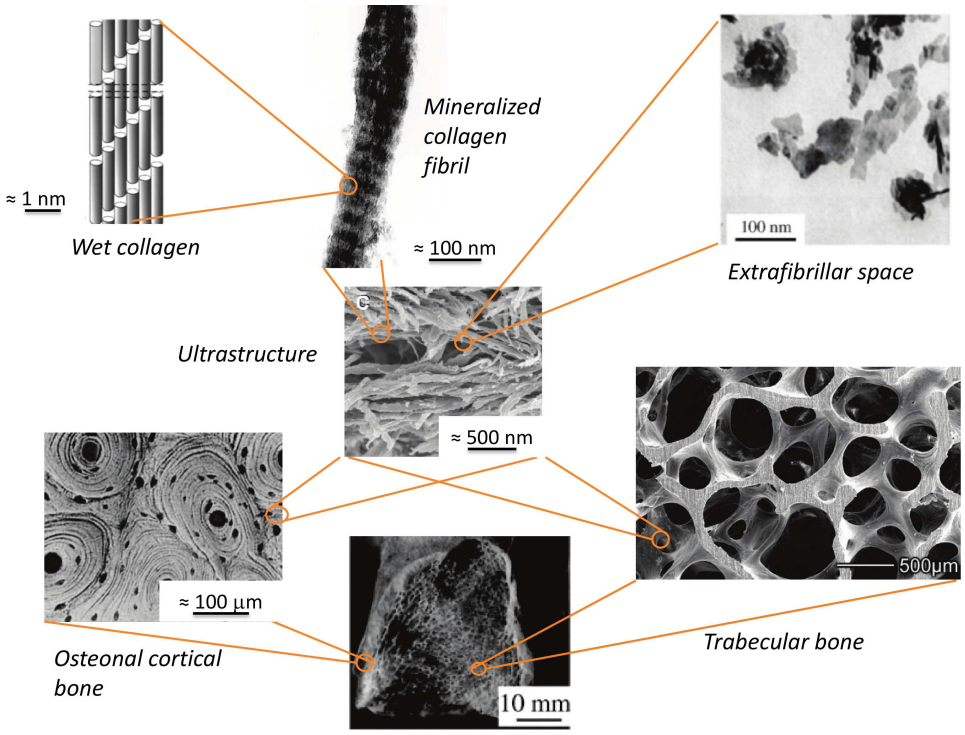

Figure 5.1: Hierarchical organization of bone. Images from (124, 125, 126).

5.2.2 Application of multiscale poro-micromechanics and ultrasonic experiments for the evaluation of elasticity of human vertebral bone

Biomechanical simulations of the intervertebral disc and adjacent vertebrae are generally accepted as beneficial tools for a better understanding of the degeneration and failure mechanisms (15, 127). Such models require a realistic reconstruction of the geometry, a consistent definition of external loads, and a reliable formulation of the material laws. For the latter, realistic elastic properties for the bone tissue are indispensable in addition to the disc properties. As could be pointed out from the hierarchical bone organization and elaborated in the work of Fritsch *et al.* (122), it seems that "universal" patterns of structural organization exist in bone, related to the material behavior (128): *"hydroxyapatite, collagen, and water are tissue-independent phases, which define, through their mechanical interaction, the elasticity of all bones, whether cortical or trabecular"*. The dosage of such "elementary" phases is thus important, at each scale, to understand the mechanical interactions of phases. Accordingly, a multiscale continuum

micromechanical model has been strictly validated against independent experimental tests, at both the extracellular and extravascular observation scales (122) and for different types of bones. However, human vertebral bone was never verified. Interestingly, in adult organs, the chemical and mechanical tissue properties are, when averaged over volumes of millimeter size, constant in space and time (129, 130, 131, 132, 133, 134). This was explicitly shown also for vertebral bone (135). Moreover, Vuong and Hellmich (136) recently performed a data analysis from bone drying, demineralization, and deorganification tests, collected over a time span of more than 80 years, to extract the chemical concentrations of hydroxyapatite, of water, and of organic material (mainly collagen) in the extracellular bone matrix. They found a unique bilinear relationship between organic concentration and mineral concentration (see Fig. 5.2), across different species, organs, and age groups, from early childhood to old age. This imply unique relationships between the tissue mass density and the mineral/collagen/water concentrations which, in combination with micromechanical models, deliver 'universal' mass density-elasticity relationships in extracellular bone matrix valid across different species, organs, and ages. Based on such arguments, the authors speculated on quantitative reflections of the interplay of osteoblasts, osteoclasts, osteocytes, and their precursors, which control, the chemical genesis and continuous transformation of the extracellular bone matrix. Therefore, on the one hand, it is instructive to compare elasticity results to this database comprising a multitude of different extracellular bone tissues from different organs and species (but no vertebral bones, so far), and check whether the bone tissues from human vertebral bone, would also fit within this very general framework. On the other hand, bone tissue is anisotropic (at least transversely isotropic) so that (at least) five independent elastic values need to be known for complete tissue characterization and such a complete elastic characterization of human vertebral bone cannot be found in the literature. Closing this gap is the goal of the present study. Therefore, the present study combines experimental elasticity determination with ultrasonic tests (137) together with bone micromechanics and poro-micromechanics, as described in 5.3. After checking whether ultrasonic elastic waves in two different direction fit within an "universal" elasticity-density relationship found for different bones in the animal kingdom (136), the desired elastic properties are given in 5.4, together with a poro-micromechanical derivation of important quantities in poromechanical analyses

and set in relation to other experimental and theoretical achievements on vertebral bone, in 5.5.

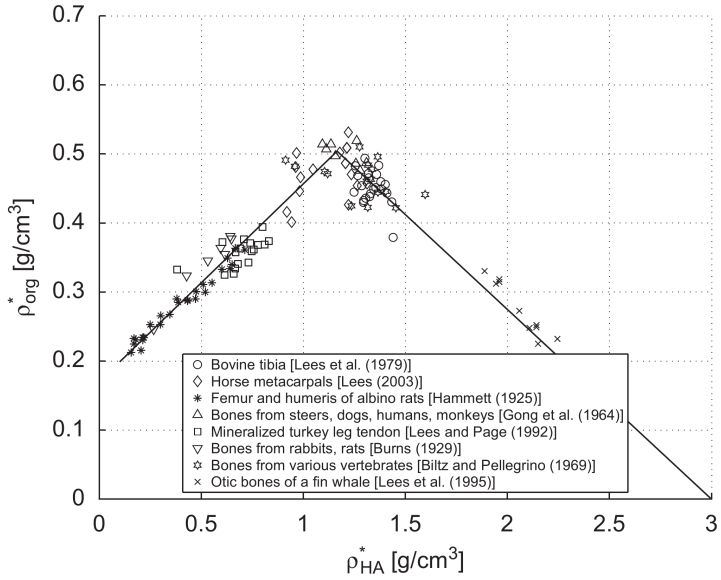

Figure 5.2: Relation between apparent mass densities of hydroxyapatite and organic matter in extracellular bone matrix, across different species, organs, and ages. Taken from (136).

5.2.3 A micro-macro evaluation of the vertebral bony endplate permeability based on computational fluid dynamics

Resistance to fluid flow is a key property of the interface between intervertebral disc and vertebrae, strongly influencing spinal segment biomechanics and transport of nutrients. A parameter that describes such a resistance is the permeability, which is of central importance in poroelastic modeling of the IVD-vertebra interface. Due to extremely reduced thickness of the subchondral bone at this interface, experimental techniques were not able to explicitly evaluate the permeability of the bony endplate portion[1] at the macroscopic level. As such, permeability values extracted from permeation experiments as well as the dependence from the flow direction observed (29, 30) were likely more representative of the adjacent cartilaginous layer that consolidates more and is

[1]The reader is referred to Chapter 2 for descriptions on the bone-cartilage interface (BEP and CEP) between disc and vertebrae (see for instance Fig. 2.4

less permeable than bone. However with aging, degeneration and/or endplate calcification, the cartilage endplate becomes thinner and hardly distinguishable from bony endplate, potentially increasing the importance of the subchondral bone permeability. A direct evaluation for subchondral bone permeability and porosity would clarify the abovementioned issues and also provide input poroelastic parameters for modeling degeneration/calcification at the endplates (138). For this, micro-computer tomography (μCT) offers a bone structural mapping from which it is possible to simulate the permeation of fluid and thus evaluate the resistance to fluid flow. Thus, by using μCT-based finite element models, the aim of this study was to calculate both permeability and porosity of the bony endplate through computational fluid dynamics (CFD) analyses.

5.3 Methods

5.3.1 Ultrasonic experiments

Cubic samples from three human lumbar vertebrae of several patients (age of death from 65 to 80 years old) were obtained from the Ludwig Boltzmann Institute for Clinical and Experimental Traumatology (Vienna, Austria). Samples were stored frozen at -20°C. No further information (gender, known diseases) were provided. Slices from the mid-height portion were cut from each vertebral body using a bandsaw under continuous water irrigation (300Cp, Exakt Gmbh, Germany). For each slice, from six to eight cubes were cut (Fig. 5.3) using a wheel saw (Isomet, Buehler, USA). All the specimens had a face containing the external vertebral cortex. Two exactly parallel opposite surfaces orthogonal to the cortex layer were cut, whereby attention was paid not to damage the cortex. The dimension of the samples (5-6 mm edge length) was chosen (i) to ensure a 'bulk' wave propagation mode[1], where the ultrasonic velocities measured for the material (i.e. bone) are directly related to the elastic constants (i.e. coefficients of the stiffness tensor, see later in the text) at the solid bone matrix level, and (ii) to avoid large measurement errors due to reduced thickness of the samples. The cubes were washed with flushing water, in order to remove the bone marrow from the large pores prior to ultrasonic measurements. The cubes were cut in two perpendicular

[1]Bulk waves are compressional, laterally constrained waves, that are considered to propagate in a quasi-infinite medium (139)

orientations: (i) axial (cranial-caudal) and (ii) circumferential (following the elliptical cross-section perpendicular to the axial direction), see Fig. 5.3.

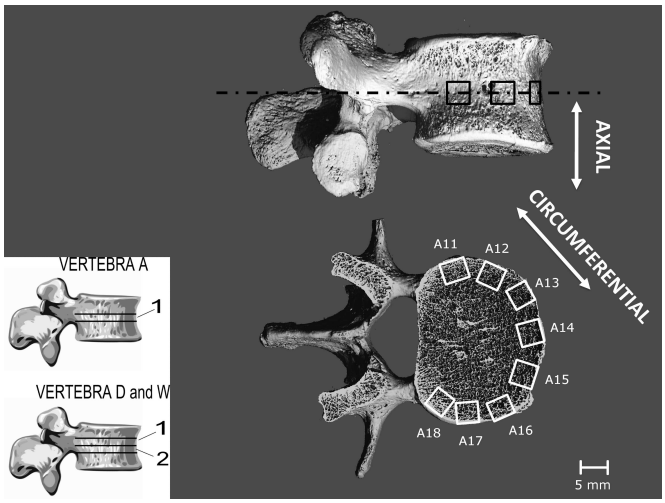

Figure 5.3: Schematic position and reference orientation chosen for cubic samples cut from one of the mid-height vertebra (vertebra A), shown in a micro-CT image.For vertebra D and W two slices were obtained from the mid-height (see inset), and cubes ere cut in the same fashion as it was done for vertebra A.

Ultrasonic testing was performed according to the through-transmission technique: two ultrasonic transducers were put in contact with the opposite faces of the tested cubic bone specimen, and honey was used as a medium for mechanically coupling the transducers to the specimen (140). An electrical signal produced by means of a pulser-receiver unit (PR 5077, Panametrics Inc., Waltham, MA, USA) was sent to the piezoelectric elements of the ultrasonic transducers, which transformed the electrical signal into a mechanical signal. This mechanical signal propagated as ultrasonic wave through the specimen and was received by the oppositely located transducer. The received signals were amplified and analyzed using an oscilloscope (WaveRunner 62Xi, Lecroy Corporation, Chestnut Ridge, NY, USA). The cubes were tested along the axial and circumferential directions showed in Fig. 5.3. The time of flight t_f needed by the acoustic signal to cross the sample was related to the travel distances l_{ax} and l_{circ}, in order to give access to the phase velocities v_{ax} and v_{circ} of the ultrasonic wave in the axial and in the circumferential direction, respectively:

$$v_{ax} = \frac{l_{ax}}{t_f}, \quad v_{circ} = \frac{l_{circ}}{t_f} \tag{5.1}$$

Since the travel distance is related to the first detected signal, the measured velocities refer to the cortical layer, being denser than trabecular bone. According to the theory of plane waves (139), the axial velocity v_{ax} is related to the axial normal elasticity component C_{3333}, and the circumferential velocity v_{circ} is related to the circumferential normal elasticity component C_{1111} through:

$$C_{3333} = \rho^{ec} v_{ax}^2, \quad C_{1111} = \rho^{ec} v_{circ}^2, \tag{5.2}$$

where ρ^{ec} is the density of the material being tested, in this study the extracellular bone matrix.

Based on continuum mechanics (141), Eq. (5.2) only holds for a material whose representative volume element (RVE) with characteristic length l is considerably smaller than the wavelength λ of the ultrasonic wave sent through the specimen, i.e. $l \ll \lambda$ (122). This requirement is necessary so that differential calculus can be used in the plane wave theory. On the other hand, the introduction of elasticity theory only makes sense if $l \gg d$, d being the characteristic length of the inhomogeneities within the RVE. Fig. 5.4 shows how dimensional characterization of a RVE from a mechanical point of view depends on the frequency and wavelength of the ultrasonic signal.

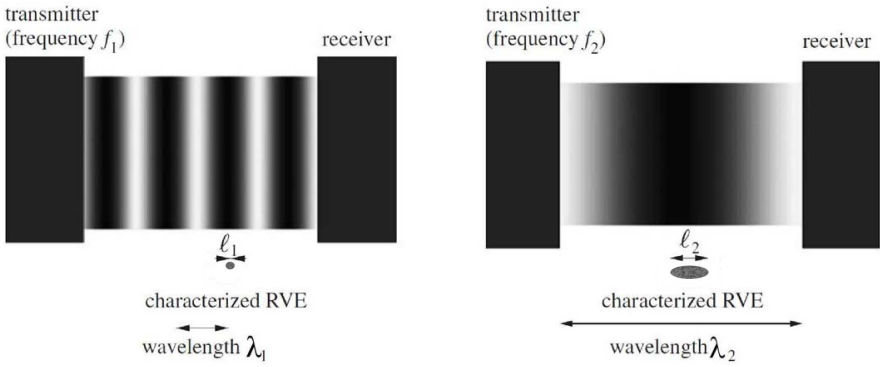

Figure 5.4: Dependency of the (mechanically) characterized RVE from the frequency ($f_1 > f_2$), and therefore from the wavelength, of the ultrasonic testing procedure. Adapted from (122).

In the case of vertebral cortex ultrastructure, d relates to the characteristic length of the mineralized collagen fibril, ranging from 100 to 500 nanometers (125). Accordingly, an RVE of ultrastructure is characterized by a characteristic length l in the order of 5 to 10 micrometers (condition $l \gg d$). Consequently, a wavelength in the order of hundreds

of micrometers is needed for characterizing the bone ultrastructure (condition $l \ll \lambda$). Such a wave length was produced through a 10 MHz pulse, since

$$\lambda = \frac{v}{f} \approx \frac{3 \text{ km/s}}{10 \text{ MHz}} = 300 \ \mu\text{m} \tag{5.3}$$

with the f pulse frequency, and with v being of the order of magnitude of the ultrasonic wave velocity in compact bone (as presented later in Table 5.2).

5.3.2 Continuum micromechanical evaluation

5.3.2.1 Multistep homogenization of bone material

In the line of a multiscale view of the bone material, a "multistep homogenization" procedure is presented here (see Fig. 5.5), which is that used in the reference works (122, 136). Such a procedure is based on continuum[1] micromechanics concepts (122, 141, 142), where a material can be seen as a homogenized continuum made up of a matrix and different types of inclusions. A homogenization procedure based on matrix-inclusion problems (143) can be applied, if the dimensional requirements of the problem do not invalidate the use of classical differential calculus and allow for a proper continuum description. In particular, inclusions must be small enough with respect to the RVE of the homogenized material (matrix plus inclusion). Such a homogenized material can now be scaled up, for instance being considered as an inclusion itself. The multistep homogenization can thus continue, and cover several scales, allowing an evaluation of a given material property - in this case, elasticity - depending on its (multiscale) inhomogeneities, on their dosage within the matrix (i.e. the volume fractions) and their characteristic shape, as schematized in Fig. 5.5.

5.3.2.2 Fundamentals of continuum micromechanics

In continuum micromechanics, it is possible to estimate the elastic properties $\mathbb{C}$ (fourth-order elasticity tensor) of a material (*macro*homogeneous but *micro*heterogeneous medium), defined on a RVE, from the phase properties (volume fractions f_r and elastic stiffness $\mathbb{C}_r$ as well as from the morphological information (141). Knowing that the phase stiffness $\mathbb{C}_r$ relates the (average) strain in phase r, $\boldsymbol{\epsilon}_r$, to the stress $\boldsymbol{\sigma}_r$ in phase r through

[1] see also subsection 2.4.1 for conceptual continuum models

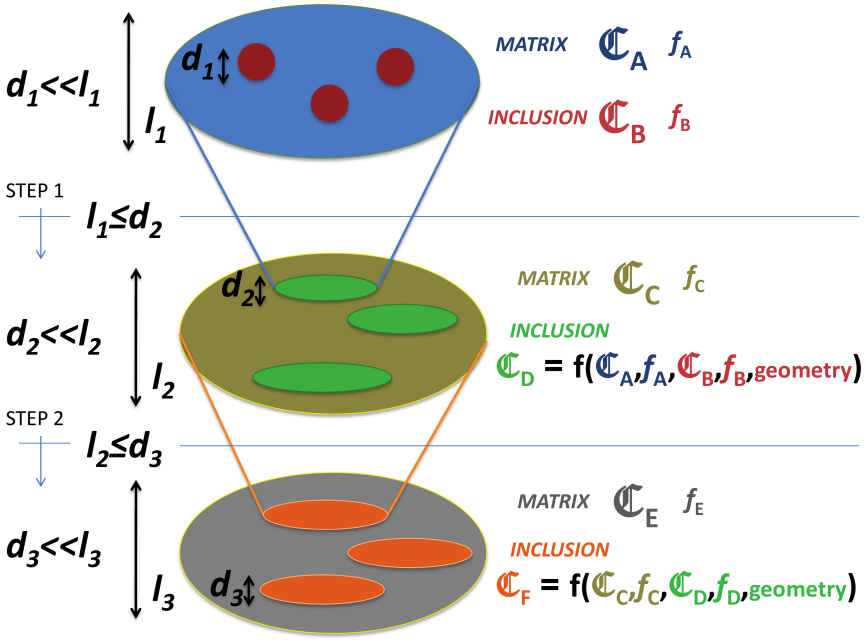

Figure 5.5: Multistep and multiscale homogenization procedure.

the well-known relations $\boldsymbol{\sigma}_r = \mathbb{C}_r : \boldsymbol{\epsilon}_r$ and $\boldsymbol{\epsilon}_r = \mathbb{C}_r^{-1} : \boldsymbol{\sigma}_r$, it is possible to average over the RVE and obtain the "overall" homogenized stress and strain (141, 144):

$$\boldsymbol{\sigma}_{homog} = \frac{1}{V_{RVE}} \int_{\partial V_{RVE}} \boldsymbol{\sigma} \cdot \mathbf{n} \otimes \mathbf{x} \, dA = \frac{1}{V_{RVE}} \int_{\partial V_{RVE}} \boldsymbol{\sigma} \, dV = \sum_r f_r \boldsymbol{\sigma}_r \tag{5.4}$$

$$\boldsymbol{\epsilon}_{homog} = \frac{1}{V_{RVE}} \int_{\partial V_{RVE}} \boldsymbol{\epsilon} \, dV = \sum_r f_r \boldsymbol{\epsilon}_r, \tag{5.5}$$

where V_{RVE} is the volume of a RVE, with surface ∂V_{RVE}. All positions on and within the RVE are located by vector $\mathbf{x}$, and $\mathbf{n}$ is the outward normal onto surface element dA of ∂V_{RVE}. The homogenized stiffness tensor $\mathbb{C}$ will thus relate homogenized stress to homogenized strain through the classical elasticity law $\boldsymbol{\sigma}_{homog} = \mathbb{C} : \boldsymbol{\epsilon}_{homog}$. Also, we define as concentration tensors the fourth-order tensors that relate $\boldsymbol{\epsilon}_r$ to $\boldsymbol{\epsilon}_{homog}$:

$$\boldsymbol{\epsilon}_r = \mathbb{A}_r : \boldsymbol{\epsilon}_{homog} \tag{5.6}$$

so that the homogenized stiffness tensor for a given material - according to Eqs. 5.4, 5.5 and 5.6 - can be expressed as a function of the concentration tensors $\mathbb{A}_r$, volume fractions f_r and phase stiffness $\mathbb{C}_r$ of phases r:

$$\mathbb{C} = \sum_r f_r \mathbb{C}_r : \mathbb{A}_r \tag{5.7}$$

5.3.2.3 Combining micromechanical evaluation and ultrasonic experiments for the determination of the anisotropic vertebral bone elasticity at the extracellular scale

The two experimentally measured velocity values (subsection 5.3.1) for specimens from the mid-height vertebra [Eq. (5.2)] can be studied by using the "universal" elasticity-density relationships reported in (136) and reproduced in Figs. 5.6 and 5.7. Such relationships allow for determination of extracellular density, provided the experimental values for velocities obey to such universal laws, at the same time. The universal relationships were found by means of a multiscale homogenization theory applied to bone (122), as depicted in 5.1. Summarizing what previously stated, analytical homogenization of bone ultrastructure comprises four steps (122): the first homogenization step refers to an observation scale of several nanometers, where crosslinked collagen molecules form a contiguous matrix, which is 'perforated' by intermolecular, water-filled spaces (wet collagen). At the fibrillar observation scale, wet collagen and mineral crystal agglomerations penetrate each other, building up the mineralized fibril. At the ultrastructural scale, mineralized fibrils are embedded as inclusions into the extrafibrillar mineral foam, forming together the extracellular bone matrix or ultrastructure (the analytical expressions of this four-step homogenization procedure are not reported here, and the reader is referred to the work of Fritsch *et al.*, (122). Instead, an additional homogenization step up to the millimeter scale was performed in the present thesis and explained later in 5.3.2.4). The input parameters for such micromechanical model are: (i) tissue-independent ('universal') phase properties of the elementary constituents of bone (hydroxyapatite, collagen, water), see Table 5.1; (ii) the mass density of the vertebra; (iii) the volume of a single collagen molecule $v_{col} = 335.6$ nm^3 (145), the average (rigid) collagen crosslink length valid for all mineralized tissues b=1.47 nm (146), the axial macroperiod of staggered assemblies of type I collagen $D \approx 64$ nm (147).

By using this model, elasticity-density and ultrasonic velocity-density relationships have been found (136) and are reported in Figures 5.6 and 5.7, respectively. The mean wave speed results (both axial and circumferential) are compared to such relationships to verify that vertebral cortex follows the hypothesized universality.

Table 5.1: 'Universal' (tissue and location-independent) isotropic (or transversely isotropic) phase stiffness values.

phase	bulk modulus k [GPa]	shear modulus μ [GPa]	experimental source
hydroxyapatite	$k_{HA} = 82.6$	$\mu_{HA} = 44.9$	(148)
water containing non-collageneous organics or osteocytes	$k_{H_2O} = 2.3$	$\mu_{H_2O} = 0$	
	c_{ijkl} [GPa]	c_{ijkl} [GPa]	
collagen	$c_{col,3333} = 17.9$ $c_{col,1111} = 11.7$	$c_{col,1133} = 7.1$ $c_{col,1122} = 5.1$ $c_{col,1313} = 3.3$	(149)

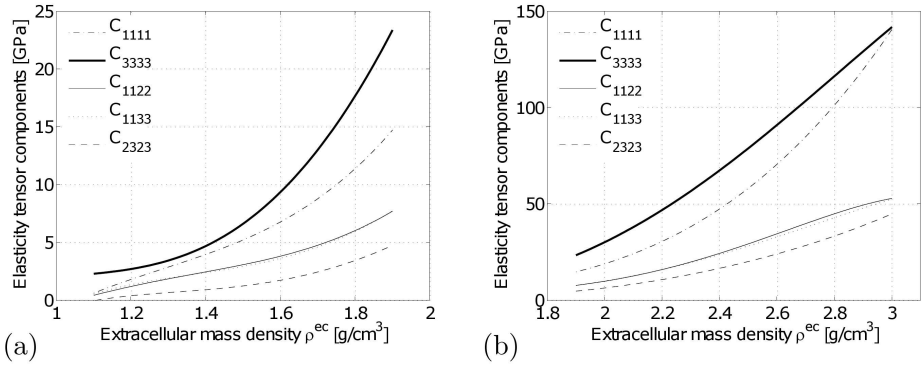

Figure 5.6: Elasticity tensor components of extracellular bone matrix, as functions of the mass density of the latter, based on the results of (136) (3-axial direction; 1,2-transverse direction): (a) Low mass density. (b) High mass density.

5.3.2.4 One homogenization step: from ultrastructure to cortical and trabecular bone, for the determination of poroelastic quantities

In the present work, we have considered vertebral bone as a multi-phase and multi-scale material, based on the hierarchical representation given in Fig. 5.1, up to the extracellular scale. Scaling up to the millimeter scale we could still see both trabecular and cortical bone as a material formed by two phases (150): extracellular bone and pores. Pores, in this simplification, would represent the intertrabecular porosity in case

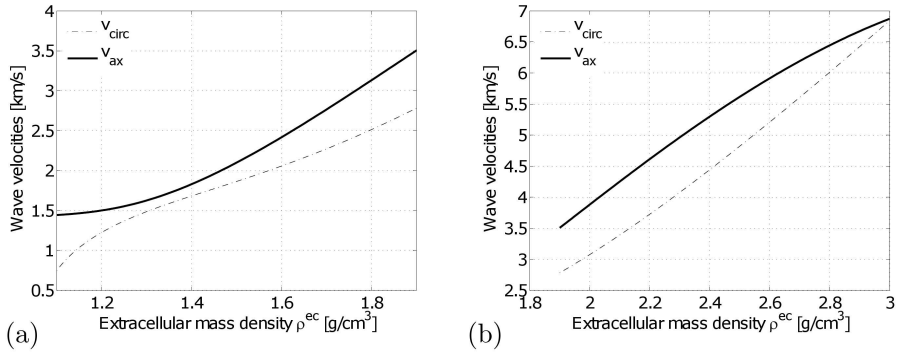

Figure 5.7: Circumferential and axial ultrasonic wave velocities within extracellular bone matrix, as functions of the mass density of the latter, based on the results of (136) (3-axial direction; 1,2-transverse direction): (a) Low mass density. (b) High mass density.

of trabecular bone or the extravascular porosity, in case of cortical bone. If we let us adopt such a scheme, we can use an additional homogenization step, which corresponds to the last hierarchical step depicted in Fig. 5.1.

As such, we can consider the extracellular bone matrix being characterized by its stiffness tensor, $\mathbb{C}_{BM}$ and its water-saturated pores by $\mathbb{C}_{H_2O}$, so that eq. 5.7 can be written as:

$$\mathbb{C} = (1-\phi)\mathbb{C}_{BM} : \mathbb{A}_{BM} + \phi\mathbb{C}_{H_2O} : \mathbb{A}_{H_2O}, \tag{5.8}$$

where the porosity ϕ has been considered as fluid volume fraction. For the estimates of the concentration tensor, following Hellmich *et al.* (150), we can refer to the framework of Eshelby problem-based continuum micromechanics (141, 143), referred to as Mori-Tanaka schemes (151) by considering the extracellular bone matrix with interacting cylindrical inclusions, corresponding to the pore space:

$$\begin{aligned}\mathbb{C} = \left\{\phi\mathbb{C}_{H_2O} : \left[\mathbb{I} + \mathbb{P}_{cyl}\left(\mathbb{C}_{H_2O} - \mathbb{C}_{BM}\right)\right]^{-1} + (1-\phi)\,\mathbb{C}_{BM}\right\} : \\ : \left\{\phi\left[\mathbb{I} + \mathbb{P}_{cyl}\left(\mathbb{C}_{H_2O} - \mathbb{C}_{BM}\right)\right]^{-1} + (1-\phi)\,\mathbb{I}\right\}^{-1}.\end{aligned} \tag{5.9}$$

In the above equation, $\mathbb{I}$ is the fourth-order unity tensor and $\mathbb{P}_{cyl}$ is the fourth-order Hill tensor, accounting for the cylindrical pore shape in a matrix of stiffness $\mathbb{C}_{BM}$:

$$\mathbb{P}_{cyl} = \frac{1}{2\pi}\int_0^{2\pi} \mathbf{\Gamma}\left(\Phi, \Theta = \frac{\pi}{2}\right) d\Phi, \tag{5.10}$$

with

$$\mathbf{\Gamma} = \boldsymbol{\xi} \otimes^s \mathbb{K}^{-1} \otimes^s \boldsymbol{\xi},$$

$\mathbb{K}$ the acoustic tensor

$$\mathbb{K} = \boldsymbol{\xi} \cdot \mathbb{C}_{BM} \cdot \boldsymbol{\xi},$$

$\boldsymbol{\xi}$ the unit lenght vector indicating the surface of a unit sphere

$$\boldsymbol{\xi} = \sin\Theta\cos\Phi\mathbf{e}_1 + \sin\Theta\cos\Phi\mathbf{e}_2 + \cos\Theta\mathbf{e}_3$$

and with Euler angles Θ and Φ relating $\boldsymbol{\xi}$ to an orthonormal basis $\mathbf{e}_1$, $\mathbf{e}_2$ and $\mathbf{e}_3$, situated at the origin of the sphere.

By comparing Eqs. 5.8 and 5.9, the concentration tensors can be identified as such:

$$\mathbb{A}_{H_2O} = \left\{[\mathbb{I} + \mathbb{P}_{cyl}(\mathbb{C}_{H_2O} - \mathbb{C}_{BM})]^{-1}\right\} : \\ : \left\{\phi\,[\mathbb{I} + \mathbb{I}(\mathbb{C}_{H_2O} - \mathbb{C}_{BM})]^{-1} + (1-\phi)\mathbb{I}\right\}^{-1} \tag{5.11}$$

$$\mathbb{A}_{BM} = \left\{\phi\,[\mathbb{I} + \mathbb{P}_{cyl}(\mathbb{C}_{H_2O} - \mathbb{C}_{BM})]^{-1} + (1-\phi)\mathbb{I}\right\}^{-1} \tag{5.12}$$

5.3.2.5 Estimation of important poroelastic quantities from the micromechanical approach

A porous media (like bone material) can be seen as a heterogeneous material composed of two phases (liquid and solid). It is possible thus to homogenize over a RVE and apply an analytical poro-micromechanical approach to find the classical state equations of Biot poroelasticity (53), as showed by several authors (144, 152, 153). Here, by following the micromechanical framework of Hellmich and Ulm (144), we will show how to estimate poroelastic coefficients originally introduced by Biot (53), and generalize the poroelastic constitutive laws[1]. Indeed, Biot showed that poroelastic materials can be described in a variety of cases, including *drained* and *undrained* conditions, i.e. if the fluid phase can freely drain out of the pores or if it cannot flow in or out of the pores, respectively.

[1]The poroelastic theoretical framework already presented in Section 2.4 was restricted to the case of incompressibility of solid phase and for quasi-static processes.

Drained condition and Biot tensor: Drained conditions happen when pore pressure is controlled from outside the RVE. From a micromechanical point of view, a special case of drained condition occurs when the material solid skeleton does not contain any fluid (empty pores) and thus pore pressure is null, $p = 0$:

$$\mathbb{C}^{empty} = (1 - \phi)\mathbb{C}_{BM} : \mathbb{A}_{BM}. \tag{5.13}$$

Eq. 5.13 is obtained from eq. 5.7 by assuming a null stiffness for empty pores. If now we consider saturated poroelastic materials, micromechanically it is possible to account for the pressurization of the pores by introducing pore pressures as eigenstresses:

$$\boldsymbol{\sigma}_{H_2O} = -p\mathbf{I},$$

that can be homogenized by using the same technique as in Eq. 5.4

$$\boldsymbol{\sigma}_{homog,H_2O} = -\phi_0 p\mathbf{I} : \mathbb{A}_{H_2O},$$

and leading to [1]

$$\boldsymbol{\sigma}_{homog} + \mathbf{b}p = \mathbb{C}^{empty} : \boldsymbol{\epsilon}_{homog}, \tag{5.14}$$

with

$$\mathbf{b} = \phi\mathbf{I} : \mathbb{A}_{pores} \tag{5.15}$$

Eq. 5.14 is the classical state equation of Biot poroelasticity after identification of the empty stiffness tensor with the drained stiffness tensor $\mathbb{C}^{empty} = \mathbb{C}^{drained}$ and $\mathbf{b}$ as the tensor of Biot coefficients. To estimate the quantity $\mathbb{A}_{pores}$ we can substitute in the estimate of $\mathbb{A}_{H_2O}$ (eq. 5.11) a tensor with all the coefficient equal to zero, i.e. the relation $\mathbb{C}_{pores} = \mathbb{O}$ instead of $\mathbb{C}_{H_2O}$. This is equivalent to consider that air fills up the pores instead of water, and allow the analytical estimation of $\mathbf{b}$.

We should note that $\boldsymbol{\sigma}_{homog} + \mathbf{b}p$ can be identified as the effective stress, this new definition being more general than that given in Section 2.4, eq. 2.11. Physically, the tensor $\mathbf{b}$ of Biot coefficients $0 < b_{ij} < 1$ describes the macroscopic stress experienced from pore pressure p when macroscopic strain is absent, i.e. $\boldsymbol{\epsilon}_{homog} = \mathbf{0}$. As Biot coefficients for a given fluid pressure increase, the macroscopic compressive strain resulting from an applied macroscopic compressive stress decreases, which gives a measure of the

[1] this result come from the validity of Levin's theorems, as showed in (141, 144)

hydraulic stiffening of the material (144). In the special case of incompressible solid phase, $\mathbf{b} = \mathbf{I}$.

The change in porosity as material deforms can be expressed as:

$$\phi - \phi_0 = \phi_0 \mathbf{I} : \boldsymbol{\epsilon}_{pores}. \tag{5.16}$$

Such change can be seen as superposition of two load cases, the first one with only strain and null pressure, $\boldsymbol{\epsilon}'_{homog} = \boldsymbol{\epsilon}'_{homog}$ and $p' = 0$ and the second one with only pressure considered, $\boldsymbol{\epsilon}''_{homog} = \mathbf{0}$ and $p'' = p$. Similarly, by combining eqs. 5.6, 5.14, 5.16, 5.4 and 5.5 the change in porosity can be referred to such superposition as (144):

$$\begin{aligned} (\phi - \phi_0)' &= \phi_0 \mathbf{I} : \mathbb{A}_{pores} : \boldsymbol{\epsilon}_{homog} = \mathbf{b} : \boldsymbol{\epsilon}_{homog} \\ (\phi - \phi_0)'' &= \phi_0 \mathbf{I} : \boldsymbol{\epsilon}''_{pores} = \mathbf{I} : \mathbb{C}_{BM}^{-1} : (\mathbf{b} - \phi_0 \mathbf{I})\, p. \end{aligned} \tag{5.17}$$

Summation of eqs. 5.17 delivers the total change in porosity:

$$(\phi - \phi_0) = \mathbf{b} : \boldsymbol{\epsilon}_{homog} + \frac{p}{N}, \tag{5.18}$$

where

$$\frac{1}{N} = \mathbf{I} : \mathbb{C}_{BM}^{-1} : (\mathbf{b} - \phi_0 \mathbf{I}) \tag{5.19}$$

is the inverse of the *skeleton Biot modulus* N (154).

Estimation of undrained stiffness tensor and Skempton coefficient: the undrained condition can be mathematically defined as a constant overall fluid mass content m in the RVE so that $dm = 0$. A constitutive law for the fluid can be introduced, by considering its bulk modulus k_f, its current fluid mass density ρ_f and such mass density at a state with zero pressure $\rho_{f,0}$ (154) so that:

$$\frac{\rho_f}{\rho_{f,0}} = 1 + \frac{p}{k_f} \rightarrow \frac{d\rho_f}{\rho f, 0} = \frac{dp}{k_f}. \tag{5.20}$$

If this equation is inserted on eq. 5.18 and considering that $dm = d\rho_f \phi + d\phi \rho_f = 0$, the pressure under undrained conditions becomes

$$p = \left(\frac{\phi_0}{k_f} + \frac{1}{N} \right)^{-1} \mathbf{b} : \boldsymbol{\epsilon}_{homog}. \tag{5.21}$$

By introducing the latter expression into the poroelastic first state equation 5.14, we obtain:

$$\boldsymbol{\sigma}_{homog} = \mathbb{C}^{drained} : \boldsymbol{\epsilon}_{homog} + \mathbf{b} \otimes \left(\frac{\phi_0}{k_f} + \frac{1}{N} \right)^{-1} \mathbf{b} : \boldsymbol{\epsilon}_{homog} = \mathbb{C}^{undrained} : \boldsymbol{\epsilon}_{homog}. \quad (5.22)$$

This allows for the identification of the undrained stiffness tensor as

$$\mathbb{C}^{undrained} = \mathbb{C}^{drained} + M \mathbf{b} \otimes \mathbf{b}, \quad (5.23)$$

where

$$M = \left(\frac{\phi}{k_f} + \frac{1}{N} \right)^{-1}. \quad (5.24)$$

Another relevant poroelastic quantity, the *overall Biot modulus* or *Biot modulus of the porous continuum* M was derived considering only a micromechanical reasoning (144, 154). Finally, by using eq. 5.21 and combining with 5.22 we can obtain:

$$\begin{aligned} \boldsymbol{\sigma}_{homog} = -\mathbb{C}^{undrained} : \mathbf{b}^{-1} \frac{p}{M} \rightarrow \\ p = -M \mathbf{b} : \mathbb{C}^{undrained,-1} : \boldsymbol{\sigma}_{homog} = -\mathbf{B}_s : \boldsymbol{\sigma}_{homog}, \end{aligned} \quad (5.25)$$

where

$$\mathbf{B}_s = M \mathbf{b} : \mathbb{C}^{undrained,-1}. \quad (5.26)$$

In case of isotropy, $\mathbf{B}_s = B_s \mathbf{I}$. B_s is called *Skempton coefficient*, and describes the increase of pore pressure due to the macroscopic stress under undrained conditions (144, 154).

It should be highlighted that all the tensorial quantities introduced so far (the tensor of Biot coefficients $\mathbf{b}$, eq. 5.15, drained and undrained stiffness tensors, eqs. 5.13 and 5.23, skeleton Biot modulus N and overall Biot modulus M, eqs. 5.19 and 5.24 as well as the tensor of Skempton coefficients $\mathbf{B}_s$ in eq. 5.26) can be easily evaluated in a matrix-based software: forth-order tensors can be conveniently expressed as a 6×6 matrices through the Kelvin notation(150)(1 is the longitudinal direction, 2 the radial direction and 3 the axial one):

$$\hat{\mathbf{C}} = \begin{pmatrix} C_{1111} & C_{1122} & C_{1133} & \sqrt{2}C_{1123} & \sqrt{2}C_{1113} & \sqrt{2}C_{1112} \\ C_{2211} & C_{2222} & C_{2233} & \sqrt{2}C_{2223} & \sqrt{2}C_{2213} & \sqrt{2}C_{2212} \\ C_{3311} & C_{3322} & C_{3333} & \sqrt{2}C_{3323} & \sqrt{2}C_{3313} & \sqrt{2}C_{3312} \\ \sqrt{2}C_{2311} & \sqrt{2}C_{2322} & \sqrt{2}C_{2333} & 2C_{2323} & 2C_{2313} & 2C_{2312} \\ \sqrt{2}C_{1311} & \sqrt{2}C_{1322} & \sqrt{2}C_{1333} & 2C_{1323} & 2C_{1313} & 2C_{1312} \\ \sqrt{2}C_{1211} & \sqrt{2}C_{1222} & \sqrt{2}C_{1233} & 2C_{1223} & 2C_{1213} & 2C_{1212} \end{pmatrix}. \quad (5.27)$$

In the same way, second-order tensors (for instance, $\mathbf{b}$) can be expressed as six-components vectors

$$\hat{\mathbf{b}} = \left(\begin{array}{cccccc} b_{11} & b_{22} & b_{33} & \sqrt{2}b_{32} & \sqrt{2}b_{31} & \sqrt{2}b_{12} \end{array} \right).$$

Also, all the poroelastic quantities introduced so far can be evaluated - as a function of porosity ϕ - by knowing the basic elastic stiffness quantities of the two phases, which means knowing $\mathbb{C}_{BM}$ and $\mathbb{C}_{H_2O}$, or $\mathbb{C}_{pores}$ ($= 0$ in case of air-filled pore space). In particular, $\mathbb{C}_{BM}$ will be provided in (5.4.1), by means of the combined experimental-numerical methodology presented in 5.3.2.3.

5.3.3 Micro to macro evaluation of effective bony endplate permeability

CT scans (μCT40, Scanco Medical AG, Basserdorf, Switzerland) of three human lumbar vertebrae were used. The voxel resolution was 12 μm. 3D parallelepiped ($2.5 \times 2.5 \times 3$ mm^3) models were generated for CFD analyses using mixed hexahedral and tetrahedral finite volumes generated with ScanIP (Simpleware Ltd.). The mesh resolution was checked for convergence to provide reliable pressure and velocity accuracy. The models considered squared cross sections (2.5×2.5 mm^2) of the bony endplate, and the third dimension was aligned with the crano-caudal direction which was the fluid flux direction (Fig. 5.8). Trabecular bone was virtually removed taking care to leave as much of the endplate part as possible. The thickness of the porous zone was variable from sample to sample, depending on the particular endplate morphology observed during the image segmentation. Endplate permeation was then simulated with a physiological mass flux boundary inlet of 10^{-5} kg/s (29) applied at a distance of approximately 1.5 mm from the endplate. The pressure at the outlet cross section was zero (Fig. 5.9). A column of fluid of approximately 1.5 mm was considered in all samples in order to stabilize the pressure at the inlet to the porous bony region.

Flow-in (from vertebra to disc) analyses were performed on: (i) 11 parallelepipeds from the cranial part and 11 from the caudal part for one of the vertebra (vertebra #1), (ii) 6 parallelepipeds from the cranial part and 6 from the caudal part for vertebra #2 and (iii) 5 parallelepipeds from the cranial part and 6 from the caudal part for vertebra #3. Flow-out (from disc to vertebra) analyses were also performed

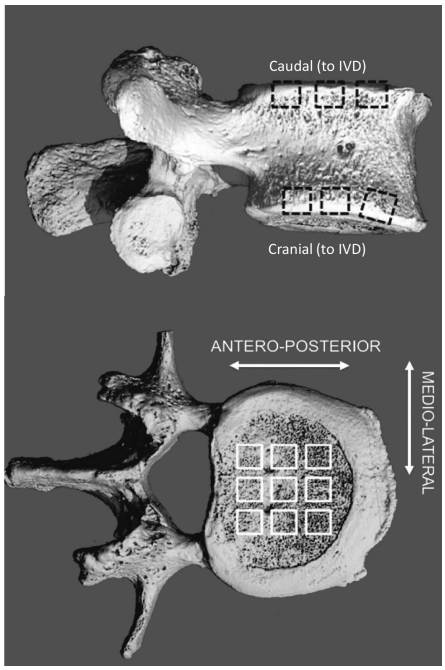

Figure 5.8: Schematic representation of the cutting procedure, to obtain the bony samples from the human vertebral endplate for successive μCT scanning.

on four parallelepipeds from the cranial part and four from the caudal part of vertebra #1. CFD steady-state analyses were performed using FLUENT (ANSYS) under implicit formulation. Density ρ and viscosity μ_f of the simulated fluid corresponded to water at 20°C i.e. $\rho = 998$ kg/m^3 and $\mu_f = 0.00103$ kg/ms. The macroscopic intrinsic permeability was evaluated through the Darcy relation 2.14 where the Darcy flux (discharge per unit area) $\mathbf{q}$ was

$$\mathbf{q} = \frac{Q_{in}}{\rho A}\mathbf{i}_3, \tag{5.28}$$

with A being the cross-sectional area, perpendicular to the (crano-caudal) direction ($\mathbf{i}_3$ is the unit vector) of the mass flux at the inlet, Q_{in}. The spatial gradient of pressure $\boldsymbol{\nabla} p$ was macroscopically evaluated as the difference between the CFD-calculated fluid pressure at the inlet of the porous material, P_{in}, and the (imposed) zero pressure at the outlet P_{out}, divided by the crano-caudal distance between these two levels (see also Fig. 5.9 b):

$$\boldsymbol{\nabla} p = \frac{(P_{in} - P_{out})}{L}\mathbf{i}_3 \approx \frac{P_{in}}{L}\mathbf{i}_3. \tag{5.29}$$

The porosity was calculated as the volume of segmented fluid-filled pores divided

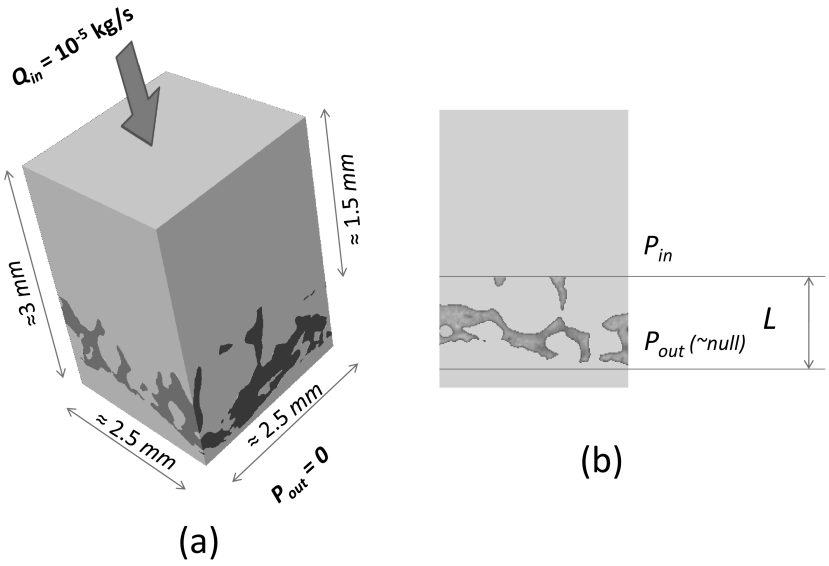

Figure 5.9: a) Dimensions and boundary conditions for the CFD experiment in the flow-in configuration. b) Example of macroscopic inlet and outlet sections for the pressure gradient evaluation. The column of fluid above the endplate region was inverted - displaced below the endplate - in the flow-out configuration.

by the total volume. Results were statistically analyzed with Minitab (97) to screen out the effect of location (cranial vs. caudal) and flow direction (flow-in vs. flow-out). Additionally, following the hydraulic-radius theories (155), a Kozeny-Carman type model was used to describe the permeability results as a function of the porosity:

$$\mathbf{k} = k\mathbf{I} = \frac{c\phi^{\alpha}}{S_v^2}\mathbf{I}, \tag{5.30}$$

where α and c were fitting parameters and S_v the specific surface, defined as the total surface of the solid matrix divided by the total volume. Such model was chosen since it predicts $k = 0$ for $\phi = 0$ and $k \to \infty$ as $\phi \to 1$, which are both characteristics needed for any valid porosity-permeability predictor (155).

5.4 Results

5.4.1 Ultrasonic experiments and micromechanical evaluation

In Table 5.2, the results in terms of axial and circumferential ultrasonic velocities are reported. The mean experimental velocity in transverse direction, $v_{circ} = 2.79$ km/s, can be related to an extracellular mass density of $\rho_{ec} = 1.90$ g/cm^3, by using the results of Vuong *et al.*, (136) in Fig. 5.7. The use of this mass density in the micromechanics formulation of (136), see Fig. 5.6, together with Eq. 5.2, leads to an axial velocity prediction of $v_{ax} = 3.52$ km/s. This value agrees very well with our (mean) experimental result of $v_{ax} = 3.45$ km/s (1.9% relative error). Hence, we have remarkable evidence that the vertebral bone tissue does follow the general relationships of Fig. 5.6, and this leads to the (average) stiffness tensor for human vertebral bone tissue. Conclusively, for $\rho_{ec} = 1.90$ g/cm^3, the complete tissue elasticity tensor, evaluated with the micromechanical approach from (122), reads as:

$$\mathbb{C}^{est}_{ultra} = \begin{pmatrix} C_{1111} & C_{1122} & C_{1133} & 0 & 0 & 0 \\ C_{1122} & C_{2222} & C_{2233} & 0 & 0 & 0 \\ C_{1133} & C_{2233} & C_{3333} & 0 & 0 & 0 \\ 0 & 0 & 0 & 2C_{2323} & 0 & 0 \\ 0 & 0 & 0 & 0 & 2C_{1313} & 0 \\ 0 & 0 & 0 & 0 & 0 & 2C_{1212} \end{pmatrix}$$

$$= \begin{pmatrix} 12.7 & 6.2 & 6.4 & 0 & 0 & 0 \\ 6.2 & 12.7 & 6.4 & 0 & 0 & 0 \\ 6.4 & 6.4 & 20.2 & 0 & 0 & 0 \\ 0 & 0 & 0 & 7.9 & 0 & 0 \\ 0 & 0 & 0 & 0 & 7.9 & 0 \\ 0 & 0 & 0 & 0 & 0 & 6.5 \end{pmatrix} \quad \text{[in GPa]} \tag{5.31}$$

5.4.2 Micro-poromechanical results

To use the approach described in 5.3.2.5 we have identified the ultrastructural stiffness tensor as the one found above with the ultrasound tests combined with micromechanical evaluation, i.e. $\mathbb{C}_{BM} = \mathbb{C}^{est}_{ultra}$ provided in Eq. 5.31. In Figure 5.10 the three non-zero components of the Biot tensor are shown. Due to the transversely isotropic form of $\mathbb{C}_{BM}$, radial and circumferential Biot coefficient were identical, i.e. $b_{11} = b_{22}$ and were renamed as "transverse" Biot coefficient. Both axial and transverse coefficients increased with porosity, although in a slightly different manner: this perceivable effect

Table 5.2: Ultrasonic wave velocities of specimens from the mid-height vertebrae at an ultrasound frequency of 10 MHz, in axial and circumferential direction (s.d.=standard deviation). The first letter of the sample ID refers to the denomination of the vertebral body, the second to the slice from the mid-height portion, see inset in Fig. 5.3, and the third is a radial counter

Sample name	v_{ax} [km/s]	v_{circ} [km/s]
A11	3.65	3.64
A12	3.47	2.01
A13	3.68	3.38
A14	3.47	3.18
A15	3.24	2.26
A16	3.32	1.83
A17	3.41	2.09
A18	3.44	-
D11	3.22	2.88
D12	3.54	-
D13	3.76	-
D14	3.43	2.95
D21	3.29	3.03
D22	3.57	-
D23	3.40	2.95
D24	3.56	-
W11	3.41	2.96
W12	3.41	2.92
W21	3.39	3.00
W23	3.45	-
W24	3.34	2.83
W25	3.48	-
mean	3.45	2.79
s.d.	0.136	0.516

of tissue anisotropy on tensor **b** indicates that for a given pressure, the marrow plays a slightly more dominant role for transverse loads with respect to the axial ones (compare transverse Biot coefficient with axial in Figure 5.10).

Figure 5.11 shows the three non-zero components of the tensor of Skempton coefficients. Similar to the Biot coefficients, circumferential and radial coefficients are identical due to transverse isotropy, therefore are plotted as one "transverse" Skempton coefficient (Fig. 5.11). With respect to Biot coefficients, the effect of porosity for

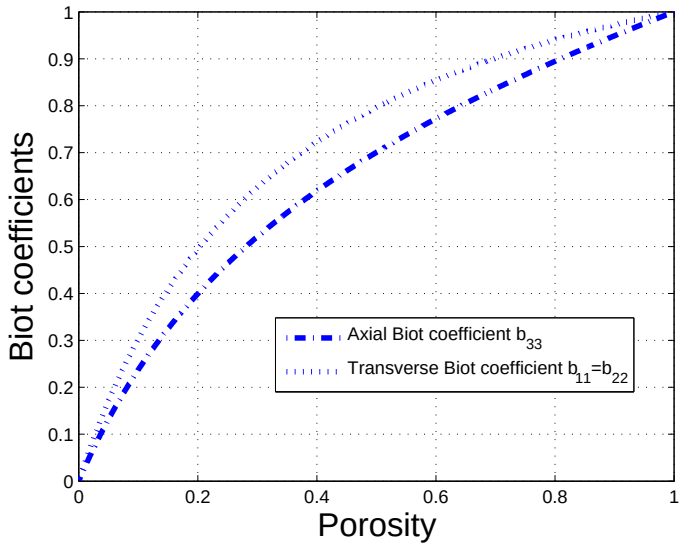

Figure 5.10: Non-zero components of the second-oder tensor of Biot coefficients as a function of porosity, obtained after micro-poromechanical evaluation. Radial and circumferential (transverse) $b_{11} = b_{22}$, and axial Biot coefficients are shown b_{33}.

Skempton coefficients is less pronounced, while the one of anisotropy is more marked. Having in mind the physical meaning of such coefficients under undrained conditions 5.3.2.5, we can estimate that transverse macroscopic stress leads to a pore pressure up to 10-times larger than the axial stress. Non-zero stiffness values and derivate elastic and shear moduli are shown in Fig. 5.12 for the drained case, whereas for the undrained one in Fig. 5.13. It can be noted that for null porosity, stiffness coefficients corresponding to the undrained case are not zero, a consequence of the presence of a constant mass content of fluid inside the RVE.

5.4.3 Macroscopic bony endplate permeability

CFD-based evaluation from μCT scans allowed us to calculate a macroscopic effective bony endplate permeability for the three vertebra scanned and for each region (cranial or caudal) of each vertebra. Results, in terms of intrinsic permeability and porosity, are summarized in Table 5.3. Spatial distribution of permeability in such regions can be visualized in color code in Fig. 5.14. There were no statistically significant differences in permeability (N=8, paired t-test $p < 0.05$) evaluated from flow-in or flow-out analyses. Also, no significant differences were found between samples from the caudal

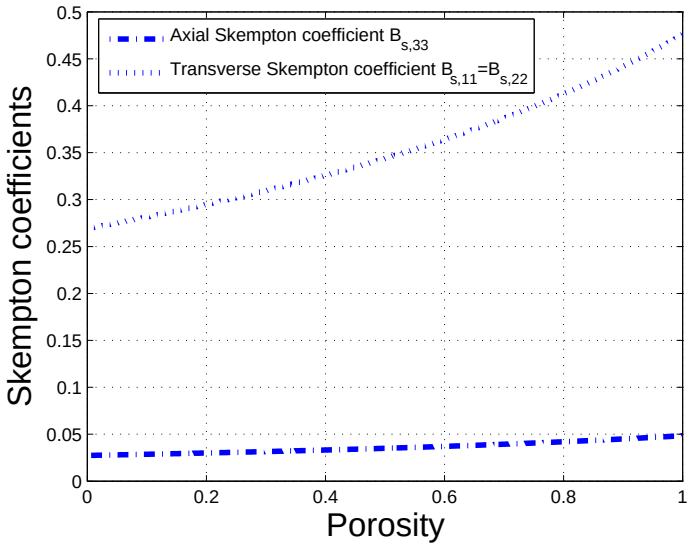

Figure 5.11: Non-zero components of the second-oder tensor of Skempton coefficients as a function of porosity, obtained after micro-poromechanical evaluation. Radial and circumferential (transverse) $B_{s,11} = B_{s,22}$, and axial Skempton coefficients are shown $B_{s,33}$.

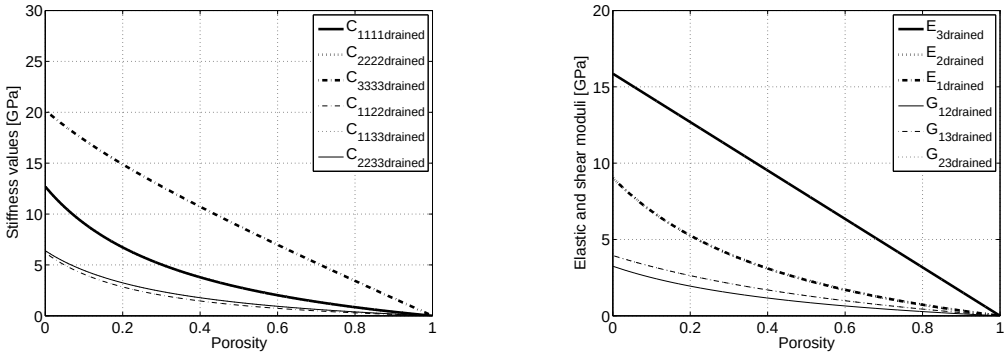

(a) (b)

Figure 5.12: Non-zero components of the forth-oder drained stiffness tensor as a function of porosity expressed in a) stiffness coefficients and b) elastic and shear moduli.

and cranial region (unpaired t-test, $p < 0.05$). Porosities and permeabilities of samples from vertebra #3 were statistically different from those from vertebra #1 and #2.

Results can also be visualized as porosity-permeability relationships, as usual in soil mechanics. Following Nauman and coworkers (96) we can perform a logarithmic

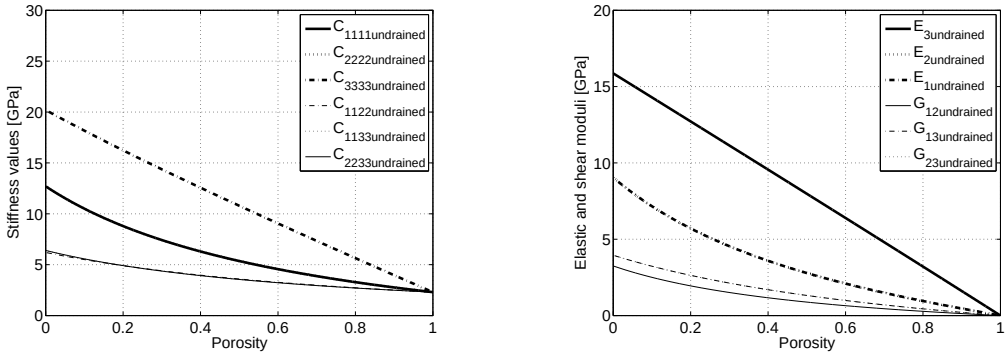

(a) (b)

Figure 5.13: Non-zero components of the forth-oder undrained stiffness tensor as a function of porosity expressed in a) stiffness coefficients and b) elastic and shear moduli.

Table 5.3: Average values and standard deviations for the effective macroscopic permeability and porosity, evaluated from CFD analyses and μCT images.

	Vertebra #1 (11 caudal, 11 cranial)	Vertebra #2 (6 caudal, 6 cranial)	Vertebra #3 (6 caudal, 5 cranial)
Permeability [$\times 10^{-10}$m^2]	8.7 ± 7.1	11.5 ± 12.2	0.9 ± 2.2
Porosity [%]	64.0 ± 7.1	63.6 ± 7.6	39.4 ± 14.1

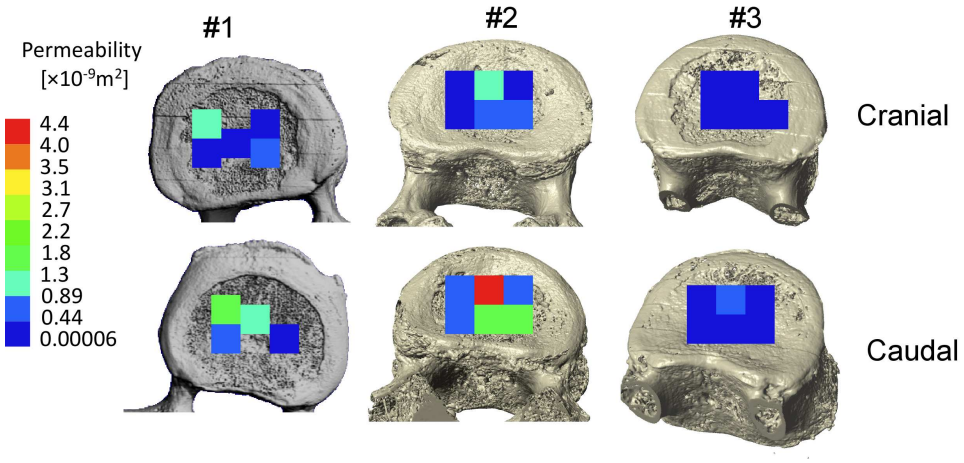

Figure 5.14: Intrinsic permeability values found for each region in each of the three vertebrae studies, visualized in color code.

regression analysis by plotting the logarithm of the intrinsic permeability as a function

of the solid volume fraction. This is depicted in Fig. 5.15 a. The resulting equation is

$$\log_{10}(k) = -7.27 \times (1 - \phi) - 6.60,$$

which can be used to compare with other experimental observations (see discussion 5.5). Also, to provide a valid permeability/porosity predictor (see 5.3.3), results were fitted by using a Kozeny-Carman model (Fig. 5.15 b). A good correlation was obtained and the fitted parameters were $\alpha = 6.81$ and $c = 0.74$.

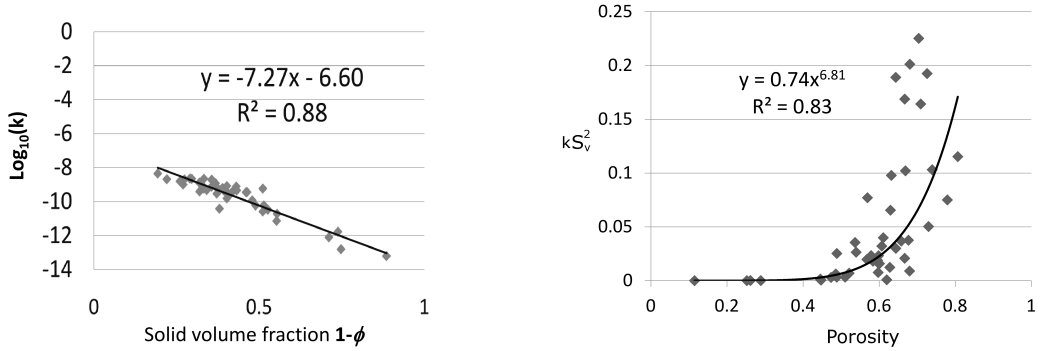

(a) (b)

Figure 5.15: a) Logarithm of the intrinsic permeability as a function of solid volume fraction. All samples from the three vertebrae in this study were considered. b) Results of porosity and permeability fitted whit a Kozeny-Carman model (Eq. 5.30).

5.5 Discussion

In the present chapter, several methodologies have been applied to the vertebral bone, in an attempt to improve our understanding of (i) vertebral bone anisotropic elasticity, (ii) bone poromechanical behavior and (iii) fluid exchanges at the bone-IVD interface. A multiscale modeling approach, based on continuum analytical micromechanics and micro-poromechanics has been applied for the first time to the vertebral bone. Ultrasound measurements at a frequency elucidating vertebral bone tissue properties were combined to the modeling approach with well-validated microelasticity laws. Additionally, 3D micro models were generated from μCT images, and fluid dynamics was simulated to calculate the effective permeability of the vertebral bony endplates. The

combination of all the presented methodologies allowed to determine (i) the full elasticity tensor of human lumbar vertebral bone, (ii) the drained and undrained elasticity tensors, and (iii) the Biot and Skempton coefficients. Such quantities helped to elucidate the role of fluid phase in vertebral bone. Macroscopic porosity and permeability values of the bone at the interface with the cartilage endplate as well as the relationship between them were also provided in the present study.

It is important to notice that the tested bone samples, on average, fulfill previously identified universal density-composition-elasticity rules valid across a variety of species and organs (122, 136). It is also remarkable that the scattering of measured values is relatively pronounced. This is probably due to the fact that we measured elastic properties of material volumes of roughly 5-10 micrometers size, and it is known that such properties fluctuate at the level of ten to hundreds of micrometers due to relatively pronounced fluctuation in composition (e.g. mineral content) at that scale (129, 156, 157).

Notably, changes in mineral content affect the transverse stiffness much more than the axial stiffness, since the mineral is mainly situated out of the mostly longitudinal collagen fibrils (156, 158). In this extrafibrillar space, hydroxyapatite builds up a mineral foam or porous polycrystal, which is "reinforced", predominantly in the longitudinal direction, by collagen fibrils (reducing the effect of mineral content on changes in longitudinal stiffness). However, the transverse stiffness is mainly governed by the mineral foam characteristics, i.e. its mineral concentration (122). Namely, the investigated cortices are only several hundred micrometers thick so that the waves "see" the aforementioned fluctuations much more pronouncedly than in millimeter-sized bone sample consisting of cortical bone only. Also, the aforementioned fluctuations are much more expressed in the transverse direction than in the longitudinal direction, and this is beautifully reflected by the standard deviations of our wave velocity measurements, being much larger in circumferential than in the axial direction (see Table 5.2).

Conclusively, a picture emerges where over-millimeter-scale-averaged tissue elasticity is precisely tuned according to 'universal' microstructural patterns found in all vertebrates (122, 136) (and clearly, also in their vertebrae, as evidenced herein), while considerable fluctuations of compositional and mechanical properties are recorded at the lower levels of extracellular bone tissue. These fluctuations cause considerable (mi-

cro)stress fluctuations within the extracellular bone matrix (159), and they are thought to be beneficial for ductility and toughness enhancement (160).

The micro-poromechanical study provided with values of poroelastic coefficients that were introduced originally by Biot in soil mechanics (53) but often are simply assumed in poroelastic modeling of biological tissues. To understand their meaning, we can also refer to an ideal isotropic case: the Biot coefficient - one coefficient instead of three as in our second-order tensor $\mathbf{b}$ - can be expressed (161) as (155) $\alpha = 1 - K/K_s$, where K and K_s are respectively the drained bulk modulus and the intrinsic solid-phase bulk modulus. In such an ideal case, the effective stress principle of 2.11 was defined in classical poromechanics as $\boldsymbol{\sigma} = \boldsymbol{\sigma}^s_{eff} - \alpha p\mathbf{I}$. It is clear thus that, considering a Biot coefficient equal to one means to consider a intrinsic solid bulk modulus much higher than the drained one, i.e. $K_s >> K$, therefore, the condition of incompressibility. With our evaluation, we have shown that, for bone, this assumption does not held, especially for low-porosity cases. It is also possible to show that (for an ideal poroelastic isotropic media), in case of undrained condition, the pore pressure is (155) $p = B(\sigma_{11}+\sigma_{22}+\sigma_{33})/3$, where B is the Skempton coefficient. Thus, the physical meaning of this coefficient is a measure of the relative compressibilites of the fluid and solid phases (B vanishes as Biot coefficient goes to one). We have shown, in line with (144) that in the transversal direction, the increase of pore pressure due to macroscopic stress under undrained conditions can be relevant, as Skempton coefficient is ten times higher than the very low values found in the longitudinal direction. We can compare our results with previous investigations of bone poromechanics, although the anisotropic nature of our approach makes difficult such comparisons: by using composite modeling and experimental data, Smit and coworkers (162) estimated for cortical bone with vascular and canalicular porosities of ϕ = 0.04-0.05 a Biot coefficient α = 0.12-0.15 and Skempton coefficient B = 0.34-0.37. With porosities in the same range, we found longitudinal (also crano-caudal, or axial) Biot coefficient (to be compared with α) b_{33} = 0.10-0.13 and transverse (circumferential) $b_{11} = b_{22}$ = 0.14-0.16. Skempton coefficients (to be compared with B) were $B_{s,33}$ = 0.027-0.028 and $B_{s,11} = B_{s,22}$ = 0.27-0.28. Regarding trabecular bone, Lim and coworkers (163) measured experimentally, in the crano-caudal direction of a bovine vertebral bone a Skempton coefficient of 0.851. In particular for this latter study, Skempton coefficient values differs significantly from the one(s) that we estimated, i.e. 0.42 and 0.042 in the transverse and longitudinal

directions, respectively - evaluated for a trabecular porosity of 0.82 as measured in same study (163). To explain the differences, it could be argued that such values could be very sensitive to the measurement conditions, or vary from organs to organs, or species to species. Indeed, poroelastic coefficients depend on the bone matrix stiffness tensor, $\mathbb{C}_{BM} = \mathbb{C}^{est}_{ultra}$, which in our case referred to experiments on human vertebral samples (Eq. 5.31). In the present study a further proof for the existence of "universal" mass density-elasticity relationships was provided, since the measured elasticity for human vertebral bone values agrees with such relationships, as already discussed. However, mass density can still vary from specie to specie and from organ to organ, and thus explain the above-mentioned differences in terms of Skempton coefficients.

When looking at the effective permeability of bony endplates, we did not found any direction-dependence resistance, i.e. flow-out and flow-in analyses brought to the same effective permeability values. However, in experiments performed by permeating bone-cartilage units such a direction-dependence was observed (29, 30), which correlated with the physiological phenomenon of a faster fluid recovery than exudation. Exudation in fact, happens in a period of time (during the day) which is two-times longer than recovery (during resting at night). The fact that this direction-dependence was not observed in bone strengthen the conclusion that it should be attributed only to cartilage, and thus to other phenomena (gradients in proteoglycan content, strain-dependent cartilage permeability) than bone morphology.

We can compare the porosity-permeability relationship found ($\log_{10}(k) = -7.27 \times (1-\phi) - 6.60$) with the one determined by Nauman and coworkers (96), from permeability measurements for several bones, i.e. human vertebrae, femurs and bovine tibiae. In particular, for specimens from the central region of human vertebral bodies, they found a relationship $\log_{10}(k) = -7.3 \times (1 - \phi) - 12$ for the crano-caudal direction, that had a slope similar to ours, and thus permeability variations as a function of the porosity similar to ours. Moreover, Nauman and coworkers performed a more comprehensive comparison of their results with several measurements (several species and anatomical locations) in the literature (164, 165, 166). We can put our results in this context and see how they compare with other permeability measurements: In Fig. 5.16, we can observe that our results are in line with a general relationship between intrinsic permeability and bone volume fraction. Moreover, intrinsic permeability and porosities

values that we have obtained are strongly subject-dependent. Factors as degree of osteoporosis and/or bone sclerosis can greatly affect such absolute values as reflected by the variability of our results and by the differences between vertebrae. The large scatter of permeability values was discussed also in (155), where a Kozeny-Carman model was found to fit data from human, bovine and porcine cancellous bone, with $\alpha = 4.668$ and $c = 2.592 \times 10^{-2}$. Although the coefficient of determination was $R^2 = 0.847$ for such fit, for a given value of porosity, permeabilities could span three order of magnitudes. Nevertheless, such fitted coefficient can be compared with the ones reported in Fig. 5.15 b and the differences can be related to different techniques, species and organs as well as to the limited number of samples in the present study, compared to the above-mentioned data (and relative models) from literature (96, 155). Finally, it is pointed out that (i) the variability of permeability values is potentially explained by relating it with structural parameters, confirming what recently found also by Widmer *et al* (138), and (ii) porosity-permeability relationship, rather than absolute values could provide a tool to perform parametric studies, for instance in combination with CT-based models, where CT attenuation can be highly correlated with porosity, and therefore, with permeability.

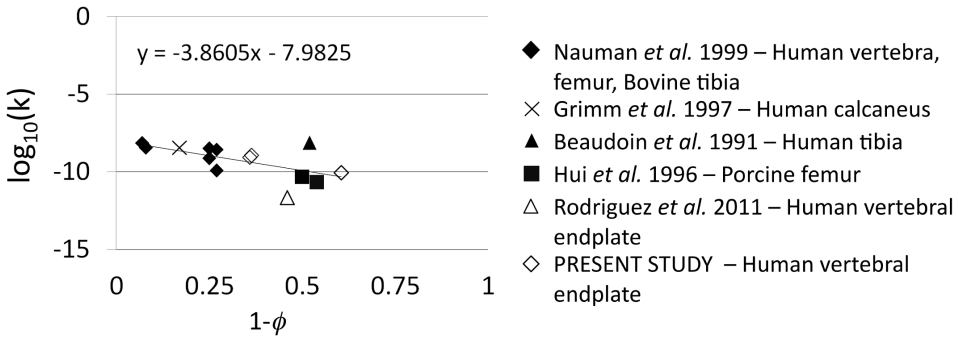

Figure 5.16: Comparison of our study with intrinsic permeability measurements in the literature.

In conclusion, in this Chapter multiscale concepts were employed to characterize vertebral bone. These concepts were based on continuum micromechanics and mico-poromechanics, as well as on computational fluid dynamics of microscopic structures. Valuable outputs for improving our understanding of the load sharing between disc

and vertebrae were obtained: (i) vertebral stiffness tensor at the extracellular scale, (ii) for the drained and undrained cases, several important poroelastic coefficients, and (iii) porosity and effective permeability of the subchondral vertebral bone. From a practical point of view, we expect that such quantities become a valuable input for vertebral Finite Element simulations (90) when extending them to CT-based (and thus, subject-specific) inhomogeneous and anisotropic properties, as it was already achieved for elasticity of mandibles (150) and femurs (167).

5. MICROMECHANICAL STUDY OF THE VERTEBRAL BONE POROELASTICITY

6

Development of a procedure for a coupled poromechanics-transport computational model

6.1 Introduction

In the previous chapters, various aspects of the IVD and vertebrae biphasic mechanics have been presented. One of the advantages of biphasic models is related to the possibility to link them with the transport of species/solutes/metabolites. Cell metabolism in the avascular IVD can be affected by fluid exchanges with the external environment. The understanding of such exchanges can provide new insights in the prognosis of disc degeneration and disc regeneration. In Chapter 4 we verified that a porohyperlastic FE implementation was appropriate to describe the biphasic nature of IVD main subtissues. In the present Chapter, a verification of a FE model of the transport of metabolites within the disc will be performed. The verification will further include the algorithm to couple the transport FE model with the porohyperelastic FE model. The algorithm will be applied to the IVD with the aim of studying metabolites distribution in the healthy disc together with the effect of IVD deformations. The main degenerative changes that occur in the disc will be simulated and a metabolites-driven cell death will be simulated to answer to clinically relevant questions to the disc regenerative medicine.

6.1.1 Features needed for a transport model of relevant solutes within the IVD

Anaerobic glycolysis (see also 2.2.5) has been recognized as the main source of energy for disc cells. Experimental work led to empirical equations modeling the interactions between the main two nutrients, i.e. oxygen and glucose and a waste product, lactate, relevant to IVD cell metabolism (168). For small neutral solutes such as oxygen, lactate and glucose, diffusion has been underlined as the main transport mechanism (169, 170). The effect of static compression on diffusion of Gadoteridol (a small solute) in the IVD has also been recently studied in vivo, suggesting a general load-dependent process when a given small solute diffuse within the IVD (171). Due to the difficulty of measuring in vivo the solute distributions within the IVD (172), finite element (FE) modeling of transport processes is often used to complement experiments and bring further insights in disc nutrition and degeneration issues. Such computational studies have shown the importance of biochemical couplings to model the disc glycolytic metabolism (173), and that of endplate obstruction to nutrients and waste products due to calcification and sclerosis (174). Fluid velocity (i.e. advective transport) was suggested to have a negligible role in enhancing small solute transport (13). Nevertheless, by coupling metabolic reactions together with a multiphasic mechanical model, different effects on solute concentrations (oxygen and lactate) were found induced by static and dynamic compressions (175), suggesting a potential role of fluid advection enhancement. Using a similar theoretical framework, Magnier and coworkers (176) studied the disc solute transport and the effect of the mechanics of free swelling. The simulated transport process depended on porosity, cell density and endplate diffusion area, but was independent of disc stiffness. Nevertheless, under sustained loads and significant tissue deformation, solute transport is expected to depend on disc stiffness. Most of the abovementioned numerical studies did not consider any local strain-dependent diffusivity (13, 18, 177) and advective effect was not clearly studied (19, 174, 177). Moreover, the few models that included both load-dependent advection and diffusion were coupled to bi-dimensional simplified geometries (175, 176), though considering 3D geometries may substantially change the transport predictions (177). Recently, a model fully coupled the diffusive, convective, and metabolic 3D transport equations with large mechanical strains (178). Static strain conditions were considered as well as the effect of endplate calcification. Glucose was found to decrease with endplate porosity reduction. Also disc deformation

caused a general decrease in glucose, which was accentuated when endplate porosity was reduced. However, transient/dynamical loads and metabolite concentrations were not presented, and other potentially relevant DDCs were not studied. In the present work, a model including biphasic mechanics, advection-diffusion-reaction (ADR), and 3D geometry is proposed to better understand IVD nutrient transport in healthy and pathological situations, i.e. the metabolic solute transport interactions with multiple DDCs - loss of fluid proteglycan content, solid matrix stiffening, cell death, geometrical changes, etc. In the first parts of the methods section (6.3.1, 6.3.2 and 6.3.3) we will (i) verify the implementation of our transport model that includes advection and strain-dependent diffusion, (ii) implement metabolic reaction for oxygen and lactate based on *in vitro* results on NP cells and (iii) verify the consistency of the algorithm to couple mechanics and transport.

6.1.2 Application of the coupled model to study IVD degeneration

Degenerative changes of IVDs (see also 2.3) occur either in a pathological manner or as a consequence of aging, and seriously compromise the tissue capability to sustain the stressful loads transmitted throughout the spine (45, 74). The IVD is the largest avascular tissue in our body and is maintained by a relatively small number of cells, which further decreases with age (179). Therefore, DDCs are strongly suspected to be linked with a failure of nutrient transport from the peripheral blood vessels to the IVD cells (9). Nutrient transport within the disc depends on the tissue composition and morphology, and is also coupled with the response to mechanical loads. While it is reported (31, 180, 181) that sustained mechanical stresses affect transport of solutes and that the nutrient pathway disturbance acts concomitantly to degenerative phenomena (9, 31), it has not been clearly investigated whether and how DDCs could affect solute transport.

We aimed at contributing to the intricate mechanics-transport connections involved in the pathophysiology of the human IVD by using the above coupled mechanics-advection-diffusion-reaction (ADR) approach in a 3D FE model. First, we hypothesized that mechano-transport couplings can affect the predictions of solute distributions in the healthy and degenerated discs. Second, we parametrically assessed which DDC (as mechanical or biological parameters) would mostly affect the oxygen and lactate transport, and in which manner.

6.1.3 Modeling glucose and cell death in the IVD

Cell death within the intervertebral disc (IVD) links with tissue degeneration and therefore needs to be fully understood. An important step, once the concentration of three solute/metabolites studied - oxygen glucose and lactate - have been implemented according to cell metabolism - is to link such concentrations with cell activity. In the literature it has been shown how the effect of acidic pH (due to lactate accumulation) can be detrimental for cell viability (182, 183, 184). Also, glucose has been underlined as the most relevant nutrient affecting cell viability: Horner and Urban (183) have found that cell concentration in a diffusion chamber decayed exponentially over time below critical glucose concentration and pH values. In this line, cell viability criteria in a metabolic transport IVD FE model have been introduced (18). In this study, the nucleus region was the most affected; cell death initiated first as CEP exchange area dropped below 40% and continued exponentially thereafter to depletion as CEP calcification was accentuated. However, disc mechanics and transient/dynamical effects were not considered. Our aim is to close this gap and determine how the deformation effect on transport would affect cell death within the IVD.

6.2 Aim

Summarizing what has been previously stated, the present study aimed at building an integrated approach that include strain-dependent diffusion and fluid advection of three relevant metabolites in a way that model also the biochemical reactions occurring *in vitro* and the porohyperelastic nature of the intervertebral disc. With this approach, the following research questions are addressed: Are mechanical phenomena capable to substantially affect the concentrations of metabolites within the disc? If a mechanical effect exists, how does it physically act and under which conditions? Which parameters are the most important in the coupled mechano-transport model? Is the mechanical effect beneficial for cell (spatial and temporal) distributions and which role could it have in disc regenerative medicine?

6.3 Methods

6.3.1 Including advective effects in diffusion-reaction transport model

Let us consider species that diffuse in a medium which in turn moves. The continuity differential equation that describes the transport of a conserved quantity is:

$$\frac{\partial c}{\partial t} + \boldsymbol{\nabla} \cdot \mathbf{q} = R, \tag{6.1}$$

where $c = \frac{\mathrm{d}q}{\mathrm{d}V}$ is the quantity q in transport per unit volume V, such as a concentration of given species, $\mathbf{q}$ is the flux (flow) per unit area and unit time of q, and R is the generation of q per unit volume per unit time. Terms that generate ($R > 0$) or remove ($R < 0$) q are referred to as a "sources" and "sinks" respectively. An advective-diffusive flux, for incompressible fluid, can be written as:

$$\mathbf{q} = -\mathbf{D}\frac{\partial c}{\partial \mathbf{x}} + \mathbf{v}c, \tag{6.2}$$

where the first quantity on the right side of Eq. 6.2 is the diffusive flux, with $\mathbf{D}$ being the second-order tensor of diffusivities and $\mathbf{x}$ the position vector, and the second quantity is the advective flux, with $\mathbf{v}$ being the velocity of the media. It should be noted that transport of species can be solved by using a thermal-transport analogy in a FE code, since the differential equations that govern heat transfer and transport are equivalent, after having converted adequately the physical constants involved (13, 185). As for the FE implementation of such transport phenomena in a porous media like the IVD, where species diffuse and are transported within the fluid phase while the saturated porous continuum deforms, an element type (or class) that contains both displacement as well as concentration degrees of freedom is needed. In our case, the ABAQUS commercial package did not allow modeling advection together with diffusion in a strain-dependent fashion. Thus, the advective-diffusive flux was modified via user subroutine by adding a stabilization term, which arises from a Taylor series expansion and has the effect of avoiding oscillations in the results (186). In time incremental terms, it is:

$$\mathbf{q}(t + \Delta t) = -\left(\mathbf{D} + \mathbf{v}^2(t)\frac{\Delta t}{2}\right)\frac{\partial c(t)}{\partial \mathbf{x}} + \mathbf{v}c(t) \tag{6.3}$$

This procedure was submitted to a verification test, in case of no sinks or sources ($R = 0$). The transport and diffusion of a concentration pulse was tested in this

verification set. A one-dimensional problem taken from Yu and Heinrich (187) was considered. The model consisted of a column of fluid 2.0 m long, meshed either with 2D (512 elements, with 0.062 m characteristic length) or 3D (16 elements, with 0.708 m characteristic length) quadratic elements. A Gaussian distribution (pulse) was applied as initial condition for the concentration c (expressed as general concentration unit u) with a unit amplitude centered at coordinate $x = 0.25$ m:

$$c(0,t) = \exp\left[-\frac{(x - v_x)^2}{4D_x}\right],$$

where the uniform velocity field with $v_x = -0.25$ m/s and the constant diffusion coefficient $D = 0.0016$ m^2/s over the bar are assumed. At time $t > 0$, the analytical solution of the governing Eq. 6.1 (with $R = 0$) is given by:

$$c(x,t) = \frac{1}{\sqrt{1+t}}\exp\left[-\frac{(x - v_x\,(t+1))^2}{4D_x\,(t+1)}\right] \tag{6.4}$$

The transient response of the concentration pulse as it advects down the length of the mesh was tracked for a period of 5.6 seconds, and compared with the analytical solution. Time increments were fixed and different time incrementation cases were studied. Also, in case of 3D elements, the solution is compared with the analytical one, and with the solution obtained with the special convective-diffusive elements designed in ABAQUS, type "DCC3D8" (that present no displacement degrees of freedom and therefore cannot be used).

The second verification test involved the comparison with a 2D problem taken from Brooks and Hughes (188). The domain was 10 × 10 m^2 meshed with 400 2D elements uniformly distributed. A function with unit value was imposed along the bottom boundary edge and the lower 3 meters of the left boundary edge, while the function at the remaining part of the boundary was specified as zero. The advective velocity had a constant value $\|\mathbf{v}_f\| = 1$ m/s over the whole space domain and was oriented with an angle of $\theta = 60$ degrees with respect to the bottom boundary edge. The two values of diffusivity in horizontal and vertical directions were identical, i. e. $D_x = D_y$ =0.6 m^2/s. The calculated concentration patterns were compared with function contours of Hughes' 2D problem at steady states with $C_r = 0.866$, where $C_r = \|\mathbf{v}_f\|\,\Delta t/\Delta_{el}$ is the Courant number - a measure of the importance of advective phenomena - and Δt and Δ_{el} the time step and the mean element length, respectively.

6.3.2 Development of a model for transport of metabolites in the IVD

For the IVD, phenomena of diffusion, advection and consumption/production of metabolites were referred to the porous continuum. A specialized, tissue-averaged form of the continuity equation 6.1 was adopted (189):

$$\frac{\partial c_{tissue}^{solute}}{\partial t} + \mathbf{v}_f \cdot \boldsymbol{\nabla} c_{tissue}^{solute} - \boldsymbol{\nabla} \cdot \left(\mathbf{D}_{tissue}^{solute} \cdot \boldsymbol{\nabla} c_{tissue}^{solute} \right) = R_{tissue}^{solute}. \tag{6.5}$$

In the above equation, *solute* refers to the particular metabolite considered - oxygen, lactate or glucose - and *tissue* to the particular RVE within the IVD subtissues - AF and NP in the present work. $\mathbf{v}_f$ is the fluid velocity relative to the solid phase. A Mackie-Meares diffusivity D_{MM} was used (190, 191), which related the volume-averaged isotropic diffusivity of each solute with the porosity of the medium and the solute diffusivity in water D_{water}^{solute}:

$$\mathbf{D}_{tissue}^{solute} = D_{MM}\mathbf{I} = \left(\frac{\phi}{2-\phi} \right)^2 D_{water}^{solute}\mathbf{I} \tag{6.6}$$

Metabolic reactions from *in vitro* experiments on NP bovine cells (168) were used for:

- pH- and oxygen-dependent oxygen cell consumption

$$R_{tissue}^{O_2} = -\frac{7.28\rho_{cell,tissue}}{S_{O_2}} \left[\frac{c_{tissue}^{O_2}\,(pH - 4.95)}{1.46 + c_{tissue}^{O_2} + 4.03\,(pH - 4.95)} \right] \tag{6.7}$$

- pH- and oxygen-dependent lactate production

$$R_{tissue}^{lactate} = \rho_{cell,tissue} \exp\left[-2.47 + 0.93pH + 0.16c_{tissue}^{O_2} - 0.0058 \left(c_{tissue}^{O_2} \right)^2 \right] \tag{6.8}$$

- glucose consumption

$$R_{tissue}^{glucose} = -\frac{1}{2} R_{tissue}^{lactate} \tag{6.9}$$

The above equations express the fact that the IVD cell metabolism was found to be mainly glycolytic, and therefore for each lactate molecule, two glucose molecule are consumed (9, 168, 183) and that oxygen consumption is of a Michaelis-Menten kinetic type (168). $R_{tissue}^{O_2}$ is in kPa/h, R_{tissue}^{lact} is in nmol/mm^{3}h, $c_{tissue}^{O_2}$ is the oxygen concentration in kPa. Since the above reactions were originally normalized with the cell density, to be

extended in other region (assuming that the cell behavior is equivalent) they had to be multiplied by the corresponding cell density. In the present implementation, the term $\rho_{cell,tissue}$ was the cell density (or concentration) for the considered tissue as porous continuum. To account for volumetric changes, it is possible to update this term by multiplying by the updated porosity in a "homogenized" cell density fashion, so that

$$\rho_{cell,tissue} = \phi \rho_{cell,f}, \tag{6.10}$$

and thus consider that cells are being part of the fluid phase f. Alternatively, and depending on the experimental data of cell density used as inputs and the corresponding measurements methods, $\rho_{cell,tissue}$ could also directly refer to the porous continuum. In such case, to account for volumetric changes, the following procedure was adopted by using the determinant of the deformation gradient of the solid skeleton J, which is equal to the volume strain $J = \frac{\mathrm{d}V}{\mathrm{d}V_0}$ (V is the updated volume and V_0 is the initial volume). In time incremental terms, it is:

$$\rho_{cell,tissue}(t + \Delta t) = \frac{n_{cell}(t + \Delta t)}{V(t + \Delta t)} = \frac{n_{cell}(t + \Delta t)}{V_0 J}. \tag{6.11}$$

Eq. 6.10 was used throughout the work presented in this Chapter, except when otherwise stated. The pH was coupled to the lactate concentration, $c^{lactate}_{tissue}$, expressed in nmol/mm^3 with the relation (176):

$$pH = 7.4 - 0.09 c^{lactate}_{tissue}, \tag{6.12}$$

which is a linearization of experimental results of pH decay with lactate accumulation. (168, 173).

6.3.3 Coupling with the FE porohyperelastic model

Our implementation involved the porohyperelastic IVD FE model presented and verified in Chapter 4 and a congruent coupling with the metabolic transport model. To link advection and volumetric changes with metabolites distributions, a sequential approach drove the poromechanical results to affect the transport solution. For volumetric changes (and therefore, porosity changes) a submodeling technique was used in ABAQUS. The porohyperelastic FE model was the "global" model, which deformed accordingly to the constitutive laws already discussed in 4.2. The "submodels" were

the transport ones, glucose, oxygen and lactate, which were driven by the deformation field experienced by the global porohyperelastic model. FE mesh geometries were the same for global and submodels. Thus, each metabolite diffused/advected/reacted while IVD geometry changed poromechanically. From the volumetric deformations porosity changes were computed (with Eq. 2.4) and diffusivities of the media at each integration point (Eq. 6.6) were updated. Relative fluid velocities $\mathbf{v}_f$ (output of the porohyperelastic IVD model) at each integration point and for each increment were transferred from the global to the submodel. The general algorithm of coupling is depicted in Fig. 6.1.

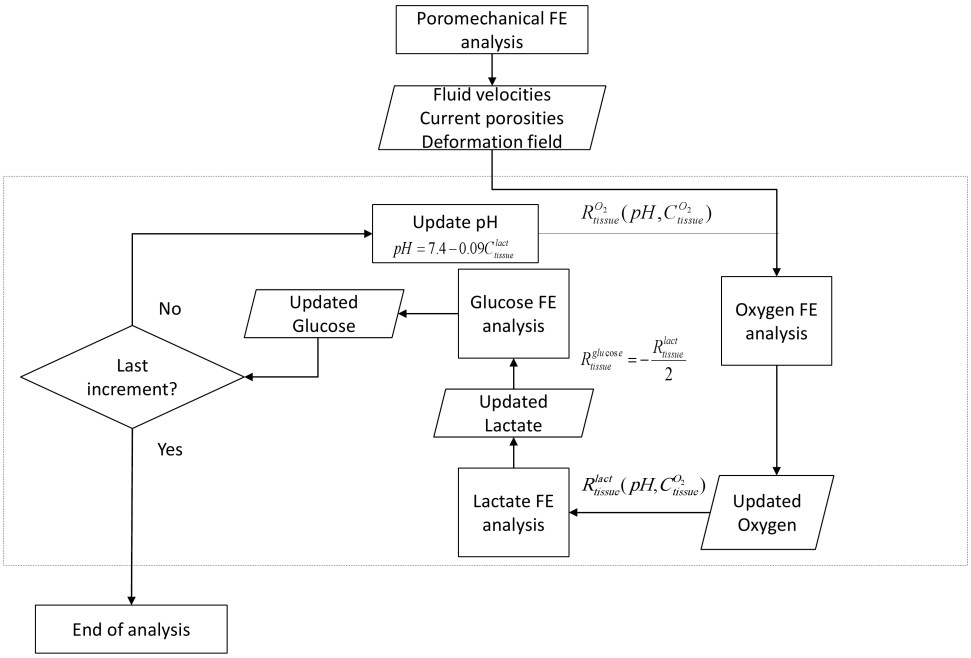

Figure 6.1: Sequential coupling scheme between poromechanical FE model and transport FE model (dashed line box). The latter considered oxygen, lactate and glucose FE analysis coupled to account for IVD metabolic reactions.

It is worth to note that the coupling procedure requires that the same time increments are chosen in all analyses, that the metabolites FE transport models do not affect the poromechanical solution, and therefore can be executed in a separate block. Since the glucose transport model was dependent only on lactate metabolic rate, we verified that at least the order or execution of the two mutual dependent metabolites - oxygen and lactate - had negligible influence on the final results, if the time increments are

chosen to be reasonably short. To prove this, we ran a series of tests changing the order of oxygen and lactate transport analyses, and we compare the resulting distributions for the two metabolites. For such tests, lactate and oxygen models were coupled with a porohyperelastic FE model already detailed in Chapter 4 with properties of Tables 4.1 and 4.3. However, additional layer modeling the adjacent vertebral bodies were included at this time. Cortical and trabecular bone properties, together with the already defined properties in Tables 4.1 and 4.3 are summarized in Table 6.1.

The model was loaded in the cranial part with a pressure of 0.5 MPa linearly increasing for 10 seconds and then maintained for 3 hours while always fixed in the caudal part (Fig. 6.2 a). For the first step of 10 seconds, a time increment of 1 second was chosen. The remaining 3 hours were divided in two steps: one of 600 seconds, with a time increment of 60 seconds, and the remaining 10200 seconds, with a time increment of 1020 seconds. The boundary conditions for the transport equation were taken from literature (18), being 5.8 kPa oxygen partial pressure and 0.9 nmol/mm^3 lactate concentration at the external AF edges and 5.1 kPa and 0.8 nmol/mm^3 at the cranial and caudal boundaries corresponding with the cartilage endplate (Fig 6.2 d).

6.3.4 Interaction between mechanics and metabolic oxygen transport in the healthy disc

Poromechanical and transport properties corresponding to a "healthy" disc were used (Table 6.1). To explore the mechano-transport responses of the models, a simple diurnal cycle consisting in 16 hours of creep under compression at 0.5 MPa and 8 hours of rest at 0.1 MPa of compressive stress was applied and repeated during two days (Fig. 6.2 b). To establish the role of mechanics in transport predictions during a diurnal cycle, the healthy disc was tested with and without the abovementioned loading. When mechanical deformation was not considered, diffusivities were constant during the simulation and calculated from the initial void ratios (and thus initial porosities via Eq. 3.2) reported in Table 6.1 by using Eq. 6.6. With mechanical loading, the roles of strain-dependent diffusivity, changes in diffusion distances and advective transport were also computed. The effect of metabolic coupling with lactate was assessed for the healthy disc by comparing with a simulation where pH was constant and equal to 7.1, where oxygen reaction depended only on oxygen availability (Eq. 6.7).

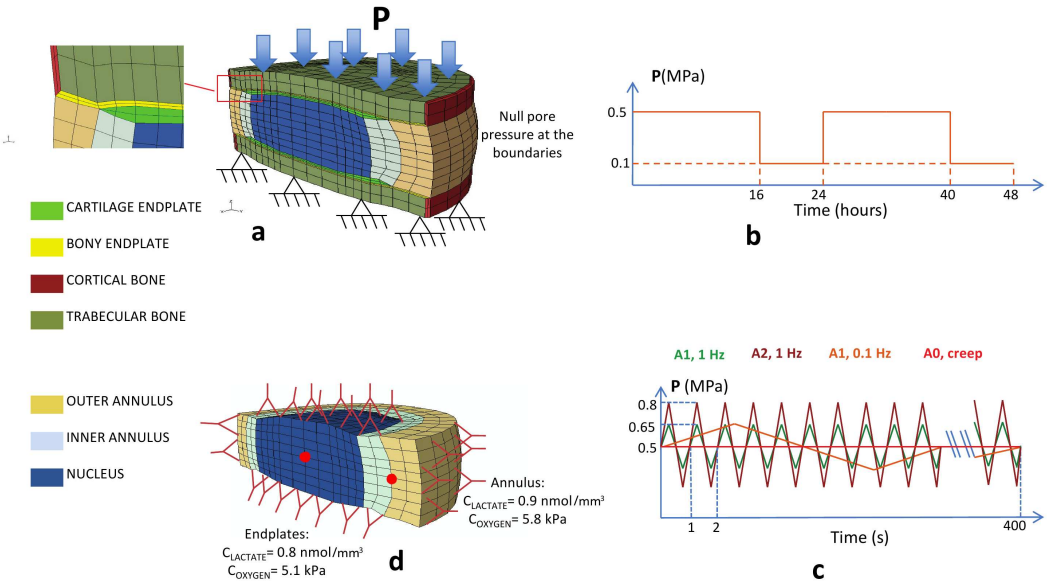

Figure 6.2: FE models, boundary conditions and loading modes used in the present study. (a) Poromechanical FE model for the IVD with all the subtissues modeled and boundary conditions applied for all the simulations; (b) load history for the diurnal cycle simulation; (c) load history for the cyclic frequency and amplitude comparison; (d) FE transport model with the applied boundary conditions. The red dots indicate the node were the results were calculated.

6.3.5 Advective effect in the IVD submitted to cyclic compressive loadings

A cyclic compression with an average load of 0.5 MPa was applied during 400 seconds. Two different frequencies (1 Hz and 0.1 Hz), and two different amplitudes (A1 and A2) at 1 Hz were considered (Fig. 6.2 c). The initial conditions of the transport model during the dynamic loading simulations corresponded to the preconditioned solution of lactate and oxygen at the end of the two days of diurnal cycles (Fig. 6.2 b). Such diurnal cycle will be presented in detail in the next Chapter. The different dynamic loading modes were compared to each other and with a creep compressive loading of 400 seconds (A0 in Fig. 6.2 c).

Table 6.1: Set of poromechanical and transport properties for the simulated healthy disc and degenerated disc.

	ϕ_0	k_0 [$mm^4N^{-1}s^{-1}$]	M	L	G [MPa]	K [MPa]	$\Delta\Pi$ [MPa]	ρ_{cell} [10^6cells mm^{-3}]
Healthy IVD properties ($H^{\ddagger}$ = 13.7 mm)								
Outer AF	0.73*	0.0002$^{\diamond}$	1.18$^{\diamond}$	-	0.28**	0.37**	-	0.063$^{\#}$
Inner AF	0.78*	0.0002$^{\diamond}$	1.18$^{\diamond}$	-	0.28**	0.37**	-	0.048$^{\#}$
NP	0.83*	0.0009$^{\pm}$	8.5^{++}	-	0.12**	0.16**	0.15$^{\spadesuit}$	0.032$^{\#}$
Degenerated IVD properties ($H^{\ddagger}$ = 12.3 mm)								
Outer AF	0.57*	0.0002$^{\diamond}$	1.18$^{\diamond}$	-	0.41**	0.55**	-	0.048$^{\#}$
Inner AF	0.6*	0.0002$^{\diamond}$	1.18$^{\diamond}$	-	0.41**	0.55**	-	0.032$^{\#}$
NP	0.71*	0.0009$^{\pm}$	8.5^{++}	-	0.19**	0.25**	0.05$^{\spadesuit}$	0.02$^{\#}$
Bone and endplates properties								
CEP	0.8^{+}	0.0025^{+}	4.63^{+}	0.08^{+}	7.14†	33.3†	-	-
BEP	0.05^{++}	26800$^{\$}$	-	-	3846^{++}	8333^{++}	-	-
Cortical	0.05^{++}	5$^{\$}$	-	-	3846^{++}	8333^{++}	-	-
Trabecular	0.8^{++}	26800$^{\$}$	-	-	42^{++}	56^{++}	-	-

*Porosity based on an interpretation (78) of experimental results of (40, 42, 75, 76) for healthy and degenerated IVDs. #Cell densities are homogeneous in each subtissue. Data from (34), corrected by a living cell rate of 80% in the case of a healthy disc and 40% in the case of a degenerated disc (192). +Evaluation from (115) based on experimental cartilage results (62). **from (77) for the healthy case and from (45) for the degenerated one. ±From (41) for healthy NP case (values were not altered with degeneration by assuming the same AF permeability behavior (45)). ++Assumed in (13). ♠Based on (41). ‡The height H of the degenerated disc model was reduced by 10% to that of the healthy disc model based on an average 5% of disc height reduction for each gradeof degeneration (43). A moderate degeneration case, c.a. grade 34, was therefore simulated. †Values were taken from (84). $Taken from (96, 193). ◇From (40).

6.3.6 Sensitivity of the transport model to mechanical and metabolic parameters related to DDCs

The parameters shown in Table 6.2 were varied one by one in order to compare oxygen and lactate profiles to a base model (with the healthy properties in Table 6.1), including all mechanical and metabolic couplings. Such changes were related to DDCs reported in experiments to assess the sensitivity of the model under realistic parameter ranges. A reduction in the overall IVD cell density (both AF and NP) from the base model was simulated based on the experimental observation of substantial increase in cell apoptosis (192) and decrease in cell activity (46) with degeneration. Porosity decrease in both AF and NP from healthy to degenerated was also reported (40, 42, 75, 76). Values were thus reduced to simulate degeneration and study the sensitivity of the model within this range. Similarly, since solid phase stiffening during degeneration was reported in both AF (40, 75) and NP (76), the sensitivity of the model predictions was evaluated to global solid phase stiffness increase in both sub-tissues. Finally, a decrease in pH from healthy to degenerated IVDs (182) and a decrease in NP swelling pressure (41) (related to the proteoglycans loss (46)) were studied as detailed in Table 6.1 and 6.2.

Table 6.2: Set of poromechanical and transport properties for the sensitivity study.

	ϕ_0	ρ_{cell} [10^6 cells mm^{-3}]	pH	k_0 [mm^{4}N^{-1}s^{-1}]	G and K [MPa]	$\Delta\Pi$ [MPa]
Base Model						
AFO	0.73	0.063	7.1**	-	G=0.28; K=0.37	-
AFI	0.78	0.048	7.1**	-	G=0.28; K=0.37	-
NP	0.83	0.032	7.1**	-	G=0.12; K=0.16	0.15
CEP	-	-	-	0.0025	G=7.14; K=33.3	-
BEP	-	-	-	-	G=3846; K=8333	-
Altered Model						
AFO	0.57	0.048	6.2**	-	G=0.41; K=0.55	-
AFI	0.6	0.032	6.2**	-	G=0.41; K=0.55	-
NP	0.71	0.02	6.2**	-	G=0.19; K=0.25	0.05
CEP	-	-	-	0.025$^+$	G=2.14‡; K=2.53‡	-
BEP	-	-	-	-	G=384.6†; K=833.3†	-

For all other properties not listed in this table, refer to the "healthy disc" properties in Table 6.1, except:

$^+$Altered value increased of one order of magnitude with degeneration (assumed based on (46)).

**Values from (182).

‡Altered values assumed in (13).

†Altered values assumed in (194)

All the above parameter changes, following the corresponding experimental sources, referred to a grade of degeneration higher than 2.5 in commonly used grading systems (38, 43). The sensitivity of the metabolic transport outcomes was also evaluated with parameters from other IVD computational models (13, 84, 115, 194), even though such values might lack experimental support: (i) cartilage endplate permeability k_0, varied over several orders of magnitude in the literature (30, 46) and thus was increased one order of magnitude (as reported during aging and degeneration (46)); (ii) cartilage endplate stiffness and Poisson's ratio values taken from (84) were both lowered up to the values reported in (13) and (iii) bony endplate (BEP) stiffness, taken in the base model as 10 GPa (13) was decreased one order of magnitude as in (194).

6.3.7 Simulation of multiple disc degenerative changes

The healthy base model was compared with a model in which all the relevant DDC-related material properties reported in Table 6.1 were considered, i.e. disc height, porosity, cell density and swelling pressure reduction, and the solid phase stiffening. However, the histological distinction between the two AF and NP subtissues was preserved, assuming a mild or moderate degenerated disc with a grade of 2.5-3 in the Thompson scale (38, 43).

6.3.8 Comparison against *in vivo* results of oxygen and lactate profiles

The model was also submitted to a validation test, by comparing the results of lactate and oxygen concentrations (in both cases of healthy and degenerated disc properties) to other *in vivo* experiments in the literature (172, 195, 196). Also, the effect of homogenizing the cell density (with Eq. 6.10 (procedure 1, "P1"), which actually reduces the effective cell density by multiplying with the porosity) or accounting for volume change through Eq. 6.11 (procedure 2, "P2") was studied. In both P1 and P2, it was assumed that the number of cells n_{cell} in each subtissue - AFI, AFO or NP - is constant over time and space and therefore equal to its initial number $n_{cell,0}$. In case of P2, Eq. 6.11 can be written as:

$$\rho_{cell,tissue}(t+\Delta t) = \frac{n_{cell}(t+\Delta t)}{V(t+\Delta t)} = \frac{n_{cell,0}}{V_0 J} = \frac{\rho_{cell,tissue,0}}{J}. \tag{6.13}$$

When P2 was used, it was thus simulated that cell density values taken in the present study - from (34) and corrected with living cell rates for both healthy and degenerated cases - were referring to the porous continuum. Absolute minimum and maximum oxygen and lactate concentration values predicted were used to compare against experimental results. Anteroposterior paths were also considered to compare against results of Bartels *et al.* (172). In such case, experimental values were normalized with the boundary (solute) value found for each patient, to reduce the effect of patient-specificity of blood supply conditions on the values of the path.

6.3.9 Simulation of cell death processes within the IVD

6.3.9.1 Verification of the procedure by comparison against *in vitro* experiments

The coupled IVD FE mechano-transport model was modified to include pH- and glucose-dependent cell viability criteria. To verify criteria, a diffusion chamber was simulated following experimental tests on bovine nucleus cell viability (183). A 26 mm width diffusion chamber filled with cells embedded in 1% agarose gel was modeled. Oxygen and lactate diffusivities in water were modified to account for gel porosity - assumed to be $\phi_{agarose} = 0.95$ - trough Eq. 6.6. For glucose, a value of $6.5{\times}10^{-4}$ mm^2/s was used, as found in the literature for agarose gels ranging 1% to 3% porosities

(197, 198). Only half of a thin slice was reproduced due to chamber geometry (Fig. 6.3). Lactate accumulation, oxygen and glucose consumption followed Eqs. 6.7, 6.8 and 6.9. Initial conditions were applied troughout the chamber for the three metabolites to reproduce the experiment: an initial pH of 7.4 (i.e. an initial null lactate concentration), inital oxygen of 21 kPa, and glucose of 5 mM. During simulation, such values were maintained only at the boundary (Fig. 6.3) since such nutrients concentration were maintained in the medium (183) in the experiment. Cell viability was considered by modifying the cell density $\rho_{cell,tissue}$ over time, depending on glucose and pH levels. Based on the same experimental study (183) 1 millions/mL cells in wells start to die exponentially without glucose. Also, at a pH value of 6.8 (183, 184) (and thus, above a lactate concentration of 15.5 nmol/mm^3) cell die over time, though at a different rate. Exponentials of the type

$$\rho_{cell,tissue} = \rho_{cell,tissue,0}\exp(\alpha_i t) \tag{6.14}$$

were implemented for cell death, with α_i being equal to -9.28×10^{-6} for $i = glucose$ and -3.43×10^{-6} for $i = pH$. Such constants were taken from the experiment of cells in wells performed by Horner *et al.* (183). The exponential decays were assumed to start when glucose and pH felt below two critical values. Such "threshold" values that initiated cell death were instead adjusted to reproduce realistically viability temporal and spatial in vitro curves as a function of cell density determined in the above-cited experiment (183).

6.3.9.2 Cell death criteria implemented in whole IVD model with mechanical coupling

By using the fully coupled model, a daily compression was considered (Fig. 6.2 b). Metabolite concentrations at the disc boundaries corresponded (1) to a normal blood supply (NBS) as in Fig. 6.2 d or (2) were reduced (RBS) by 50% of such reference values. In this study, since IVD deformations are considered, cell densities were updated at each integration point by using Eq. 6.11. When criteria of cell viability were not met in time and space, cell density was updated only considering the volume changes and not changes in their number (with Eq. 6.13); otherwise, the number of cells per volume followed exponential decays. Specializing Eq. 6.14, the time incremental scheme was:

$$\rho_{cell,tissue}(t+\Delta t) = \frac{n_{cell}(t+\Delta t)}{V(t+\Delta t)} = \frac{n_{cell,0}\exp(t+\Delta t)}{V_0 J}. \tag{6.15}$$

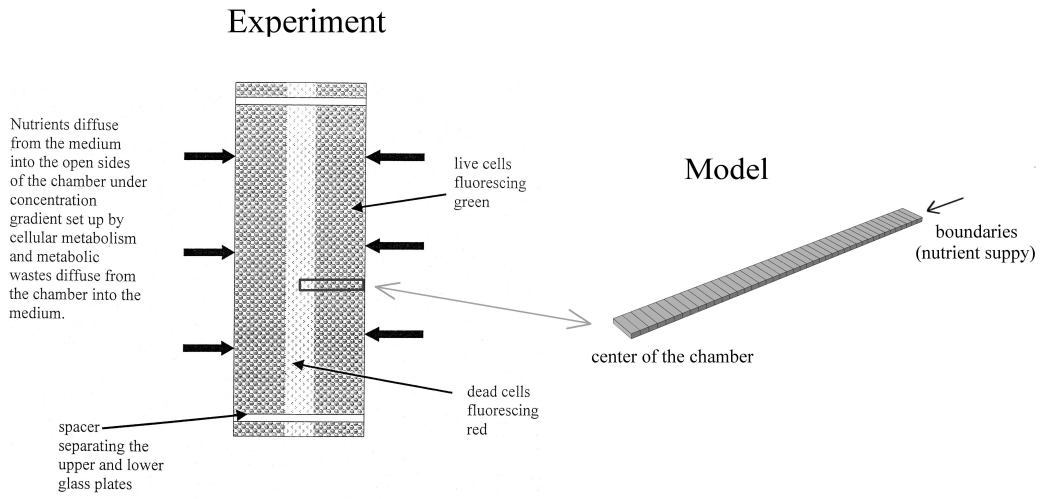

Figure 6.3: Diffusion chamber in the reference experiment (reproduced from (183)) and FE model that accounts for a representative half portion because of the symmetry of the problem.

A preconditioning of 2-days of metabolites diffusion in both cases was applied prior to consider mechanical coupling and viability. Solutions with cell viability only and with both viability and mechanical coupling were compared.

6.4 Results

6.4.1 Verification of the procedure to model advection

Fig. 6.4 shows the implemented FEM advective procedure on a 2D bar, based on user subroutine of Eq. 6.3 (curve "FEM"), against the implementation via Eq. 6.2 (curve "FEM non stabilized") and against the analytical solution (Eq. 6.4), for the unidimensional problem described in 6.3.1. As shown in Fig. 6.4a, both implementation can avoid oscillations in a advection-dominated problem such the one considered, provided the number of increment and elements is quite high. However, when number of increments is reduced (from 200 to 20) the need of using a stabilization term as in Eq. 6.3 was evident, and it provided more reliable results, when compared to the analytical solution after 2 and 5.6 seconds (Figs. 6.4 b and c).

Such procedure implemented in 3D elements to test the same unidimensional problem but with a less refined mesh (only 16 elements) also led to curves that presented

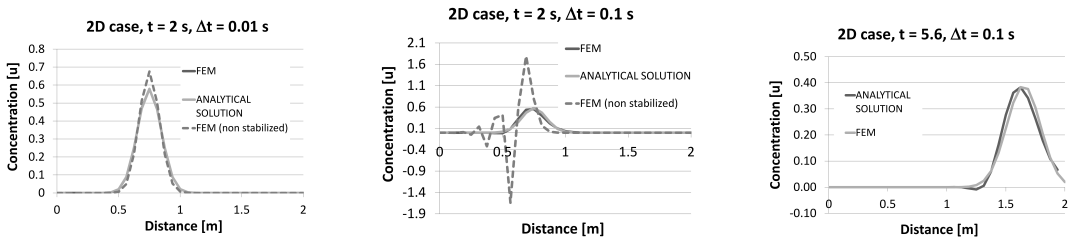

(a) (b) (c)

Figure 6.4: Comparison of the FE implementation of advection in a 2D mesh with a stabilization term (curve "FEM") against results of the FE implementation without stabilization term (curve "FEM non stabilized") and against the analytical solution. a) Case with 200 fixed increments after t = 2 s, b) 20 fixed increments after t = 2 s and c) 20 fixed increments after t = 5.6 s.

negligible differences when compared to the analytical solution, and performed even better than the special-purpose ABAQUS 3D element with such low level of mesh discretization (Fig. 6.5).

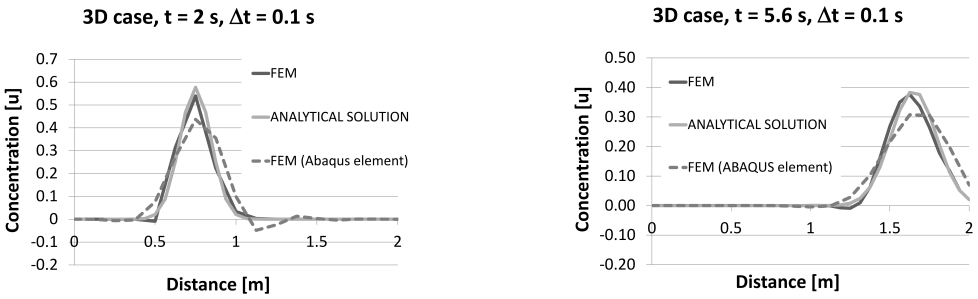

(a) (b)

Figure 6.5: Comparison of the FE implementation of advection in a 3D mesh with a stabilization term (curve "FEM") against results of the FE element technology provided by ABAQUS and against analytical solution. a) Case with 20 fixed increments after t = 2 s and c) after t = 5.6 s.

The comparison of the implemented advection procedure against the verified numerical example of Brooks and Hughes (188) is showed in Fig. 6.6. A good agreement of isolines, expressed as function values, was found for Courant number lower than

0.866.

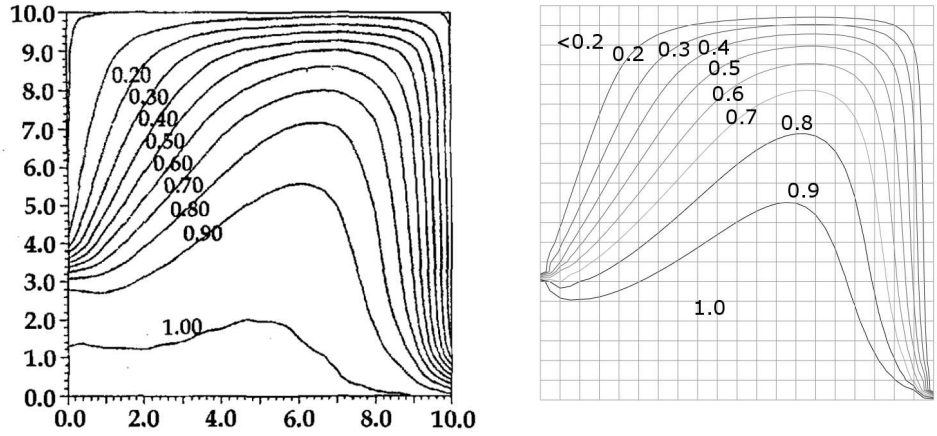

Figure 6.6: Results of the implemented advection procedure (right) compared with a numerical verified example from (188) [plot on the left reproduced from (199)) (left)]. Values are expressed as function units, while dimensions on the edges are in meters.

6.4.2 Coupling with the FE porohyperelastic model

The sequential approach to couple the porohyperelastic model with transport of metabolites was independent of the routine order (i.e. lactate and oxygen FE analyses order in Fig. 6.1). The relative difference comparing oxygen and lactate concentrations calculated at the end of two analyses obtained with inverse order were lower than 1 % for both solutes all over the AF and NP subtissues.

6.4.3 Advective effect in the IVD submitted to cyclic compressive loadings

In Fig. 6.7 the vertical displacement (crano-caudal direction) of a point on the cranial face, in the four cases with different amplitudes and frequencies are shown. Despite the different oscillations due to different amplitudes and frequencies, which are reflected in the displacement field, the average trend in terms of volume changes was very similar to the case without cyclic loading (i.e. A0 case). When looking at the oxygen and lactate distributions in both AF and NP, we computed negligible effects (0.5% relative

differences) of amplitude A1 vs. A2, frequency 1 Hz vs. 0.1 Hz, and amplitude A1 and A2 vs. creep loading amplitude A0.

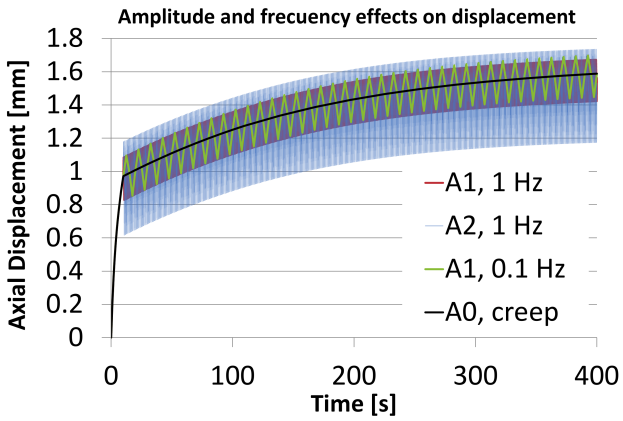

Figure 6.7: Verical displacement of the porohyperelastic IVD FE model with three types of amplitude-frequency combinations and creep loading, correspondent to the boundary conditions depicted in Fig. 6.2 c.

6.4.4 Interaction between mechanics and metabolic oxygen transport in the healthy disc

Fig. 6.8 shows oxygen and lactate distributions in a sagittal section of the disc model with and without poromechanics-transport coupling, and for a transient analysis corresponding to the end of the second 16-hour creep period. For all cases, the anterior annulus fibrosus (AF) presented the lowest oxygen concentrations and the highest lactate levels.

Local oxygen concentration is shown over time (Fig. 6.9 and 6.10) for two nodes at the central NP and the anterior AF (red dots in Fig. 6.2 d). With initial conditions of zero oxygen and lactate within the disc, steady state concentrations were reached in approximately 16-18 hours without mechanical loading. When mechanical deformation was considered, a steady-state solution never occurred. Instead, a repetitive pattern was identified following loading and recovery phases.

In all cases, with mechanical coupling, maximum oxygen and lactate concentration changes occurred at the end of the creep compression. Shortening the diffusion distance by reducing by 10% the undeformed healthy disc height - with constant diffusivities -

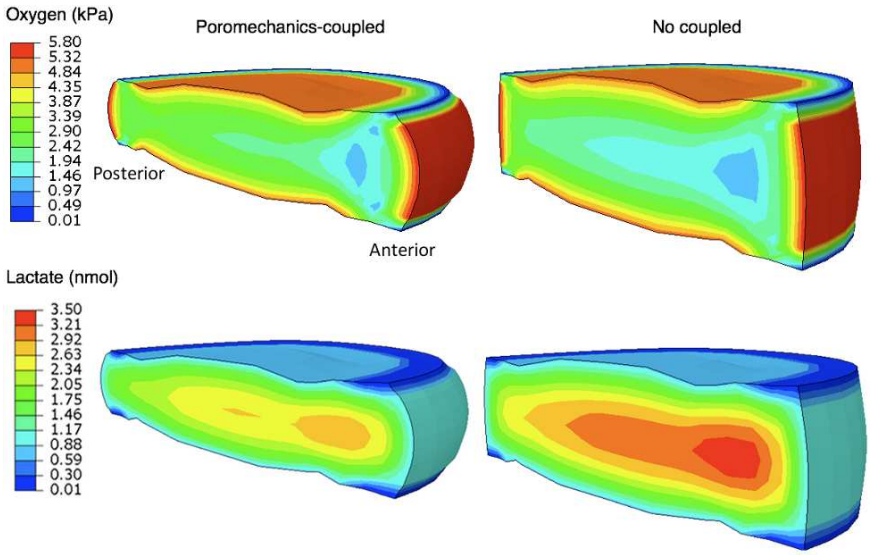

Figure 6.8: Distributions of the interdependent oxygen and lactate concentrations. Distributions are computed at the end of the 16-hour creep, with (left) and without (right) poromechanical coupling. With poromechanical coupling (left) both oxygen and lactate transport equations were solved over time taking into account the current deformed geometry.

increased the oxygen levels in both the central NP (up to 57%) and the anterior AF (up to 11%). Simultaneously, the lactate concentration decreased by a maximum of 27% in the NP and 22% in the AF, when compared to the undeformed case (Fig. 6.9). Including strain-dependent diffusivities resulted in a subsequent oxygen decrease in both the NP (up to 17%) and the AF (up to 18%) with a coupled counter-balanced lactate increase (up to 16% in the NP and 10% in the AF), in comparison to the model with decreased diffusion distances and constant diffusivities. Merging together both strain-dependent diffusivity and diffusion distance changes caused an oscillating increase of oxygen for the central NP with a peak of 31% compared to the undeformed case, while a maximum of 9% oxygen decrease was calculated for the anterior AF. For lactate, with both strain-dependent diffusivities and distance changes, a similar decrease in both the anterior AF and the central NP up to 15% was found, compared to the undeformed case (Fig. 6.9). Advective effects were insignificant. Finally, when neglecting the lactate-dependence (via pH changes) of oxygen reaction, we found a 2.5% decrease in oxygen concentration in the anterior AF and 8% increase in the central NP, with respect to the lactate-coupled

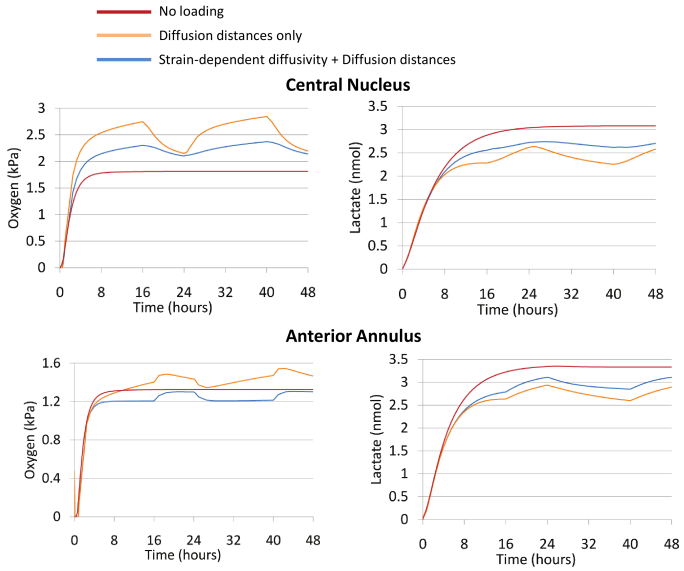

Figure 6.9: Effect of strain-dependent diffusivity and diffusion distances on oxygen and lactate. Comparisons in terms of oxygen and lactate concentration in the AF and NP of the healthy disc model under three cases: no loading, loading with a reduced disc height, and loading with reduced disc height and strain-dependent diffusivity under the diurnal cycle loading mode for two days simulated.

solution without poromechanical coupling (Fig. 6.10).

6.4.5 Sensitivity of the transport model to mechanical and metabolic parameters related to DDCs

Fig. 6.11 shows the sensitivity in terms of solute (oxygen or lactate) concentration under a given parameter change, normalized to the base model value, for both AF and NP. Fig. 6.11 refers to results at the end of the two simulated days. Within both the AF and the NP, oxygen and lactate concentrations were significantly more sensitive to porosity, cell density and swelling pressure changes than to variation of the other parameters, i.e. CEP permeability, pH and solid phase stiffening. In average, over both the AF and the NP, the oxygen concentration decreased by 44% and the lactate concentration increased by 36% when porosity was reduced. When cell density was reduced, the oxygen relatively increased by 42% and the lactate decreased by 21%. When the NP swelling pressure was reduced, a 44% relative increase in oxygen and a 23% relative decrease in lactate concentration were computed. As for the remaining parameters,

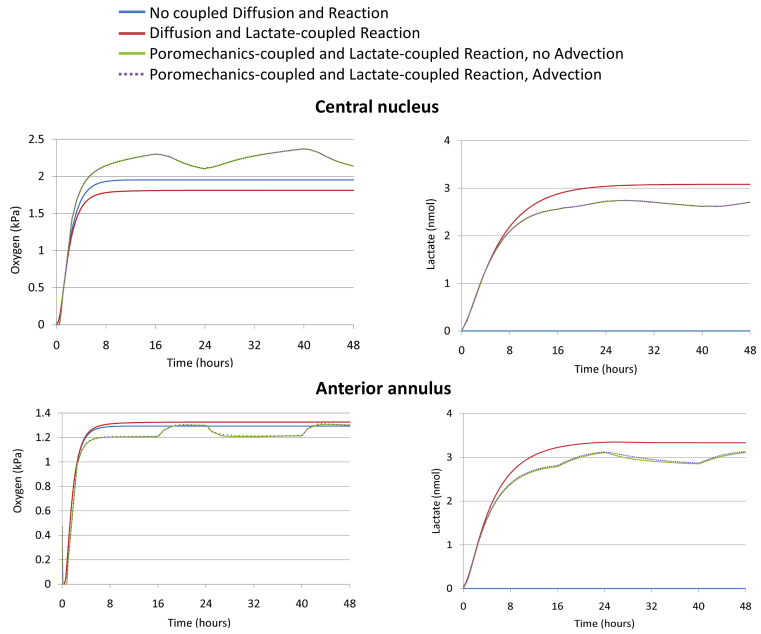

Figure 6.10: Effect of different couplings on oxygen and lactate. Comparisons in terms of oxygen and lactate concentration in the AF and NP of the different combinations studied in terms of couplings under the diurnal cycle loading mode for two days simulated.

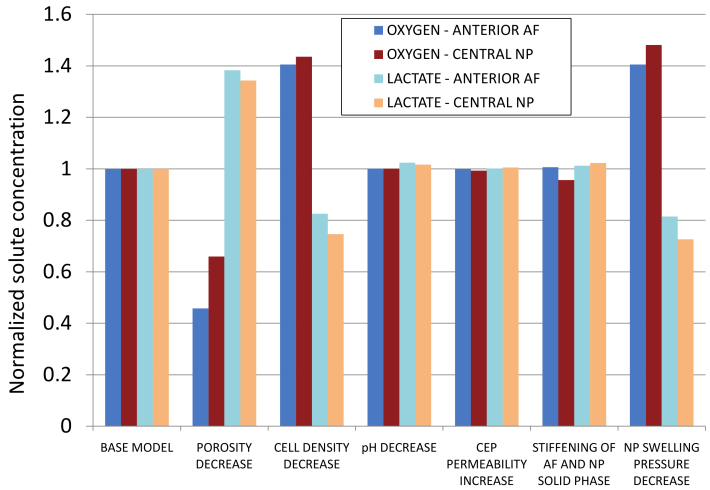

Figure 6.11: Results of the sensitivity study. Oxygen and lactate concentrations in the AF and NP are normalized to the base model.

less than 3% of relative changes in solute concentrations were found. Finally, CEP and BEP stiffness variations gave differences in oxygen and lactate concentrations lower than 0.2% (data not reported in Fig. 6.11). The sensitivity results in Fig. 6.11 were similar to those found at the end of the sustained creep (data not shown).

6.4.6 Simulation of multiple disc degenerative changes

Fig. 6.12 shows the oxygen and lactate concentrations predicted at the end of the second 16-hours creep compression along the mid-transversal anteroposterior paths of both the healthy and degenerated disc models. Transport equations and mechanical deformations were alternatively coupled (deformed) and decoupled (undeformed). While mechanical coupling tended to favor oxygen concentration and limit lactate accumulation within the healthy disc, it had only scarce effects within the degenerated IVD model.

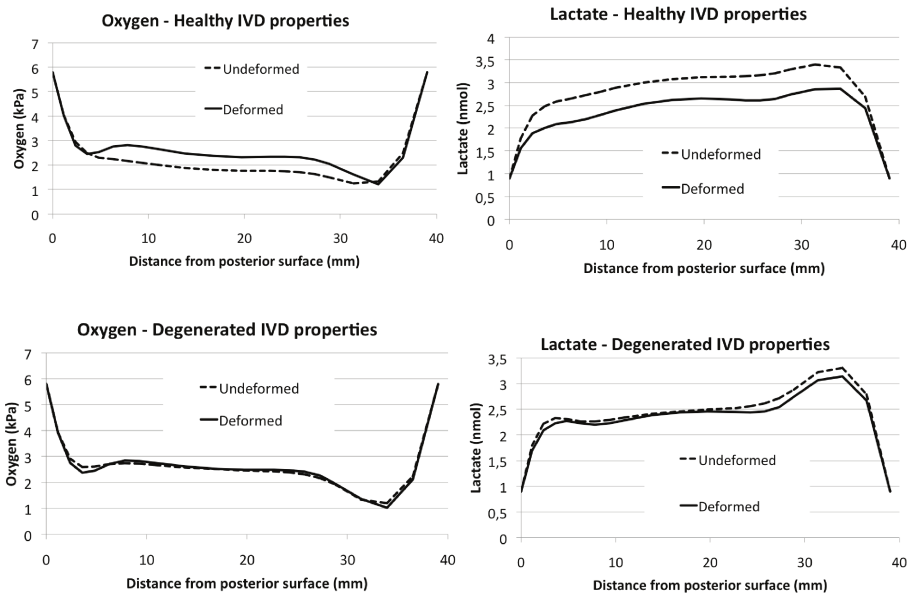

Figure 6.12: Effect of healthy and degenerated disc properties: Oxygen and lactate levels for the IVD mid-height and as a function of the anterior-posterior position for simulated healthy (top) and degenerated (bottom) disc properties.

6.4.7 Comparison against *in vivo* results of oxygen and lactate profiles

Minimum oxygen pressure at disc mid-height was about 1 kPa in all models (healthy and degenerated cases) with P1 procedure. Also, the maximum lactate concentrations, predicted were nearby 3.5 nmol/mm^3. With P2 procedure, which takes into account volume changes without homogenizing with actual porosity (and therefore considering input cell density values as referred to the continuum and not only to the fluid phase), minimum oxygen pressure at disc mid-height was about 0.5 kPa and maximum lactate about 4-4.5 nmol/mm^3. With both P1 and P2, predicted values were close to the experimental range found in literature: Bartels *et al.*(172) found, in patients with scoliotic and back pain a minimum oxygen of 0.71 kPa and a lactate range of range of 2-6 nmol/mm^3. 0.3-1.06 kPa for oxygen concentration was also found in canine NP (195, 196). The location of minimum oxygen and maximum lactate contents were in agreement with other studies (175, 176, 177). Fig. 6.13 shows the results of oxygen and lactate in the present study against the experimental range normalized with the boundary value found for each patient (172). Normalization was performed because the solute concentrations reached within the disc strongly depend on the patient-specific vertebral blood supply. Although the comparison was made only with the lumbar discs, the experimental variability is still very high. However, a similar anteroposterior trend was found between our study and the experimental results for both lactate and oxygen concentrations (in particular for experimental curves in black in Fig. 6.13).

6.4.8 Simulation of cell death processes within the IVD

6.4.8.1 Verification of the procedure by comparison against *in vitro* experiments

In Fig. 6.14, viability profiles predicted by the model are shown, in comparison with the reference experiment, for different cell density, at two time lapses (3 and 6 days of culture). There was a good agreement of the computed cell viability profiles against literature data. The adjusted threshold critical values of glucose and pH were 0.5 and 6.78, respectively.

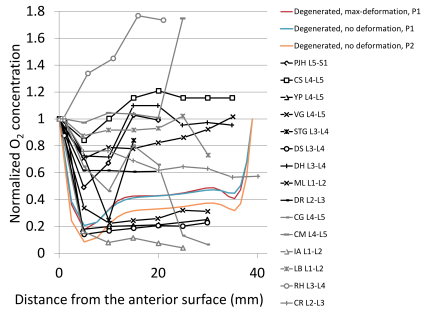

(a)

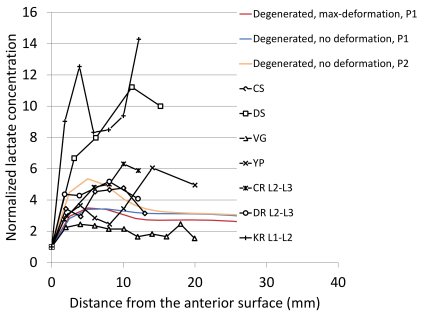

(b)

Figure 6.13: Comparison with oxygen and lactate measurements from literature. Oxygen and lactate normalized concentration from published experimental data on human patient with back pain and scoliosis (172) (patient designation duplicated from followed by the level of the IVD where concentrations were measured) compared with the model results from the present study (case with all DDC simulated) "Maximum deformation" refers to the end of the second sustained compression period and no deformation to the steady state solution. P1 and P2 are the different procedures to update cell densities described in Eqs. 6.10 and 6.11, respectively.

6.4.8.2 Cell death criteria implemented in whole IVD model with mechanical coupling

For the IVD model, NBS condition maintained glucose and pH levels above the critical ones. In case of RBS (Fig. 6.15) cells in the IVD center started to die since critical glucose concentrations were reached. Deformation couplings increased glucose and therefore cell viability. As a consequence, cells stopped dying about 10 hours earlier when mechanical deformations were considered. Also, it is possible to compare the spatial distribution of the exponential function that describes the cell viability at the end

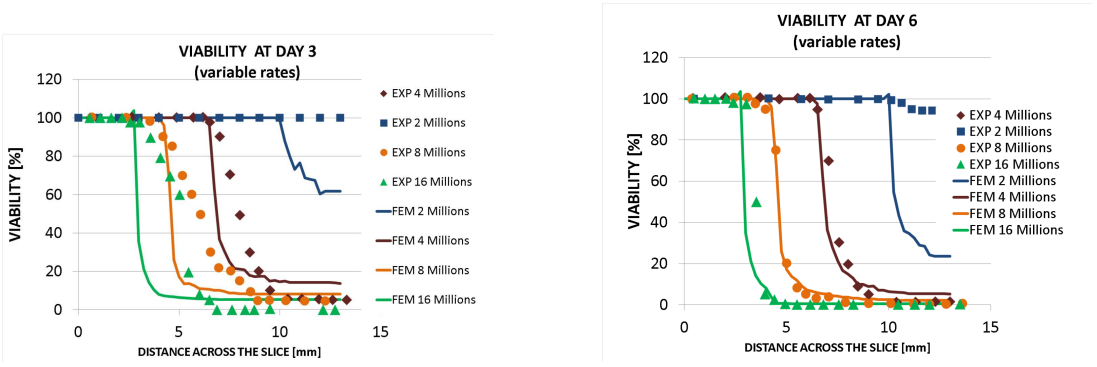

(a) (b)

Figure 6.14: Viability profiles in the simulated half-slice of the chamber and their comparison with experimental results (183), for different cell density (in millions cells/mL). a) Numerical results from FEM computed and compared at day 3. b) at day 6.

of the simulated period in Fig. 6.16 in two cases, with or without mechanical couplings. The most evident change occurred in the central disc, where mechanical deformations increased the glucose concentrations and therefore cell viability was beneficed. However, mechanical couplings also decreased cell viability in the posterior annulus fibrosus due to the prevalence of a strain-dependent effect that reduced diffusivity in this area.

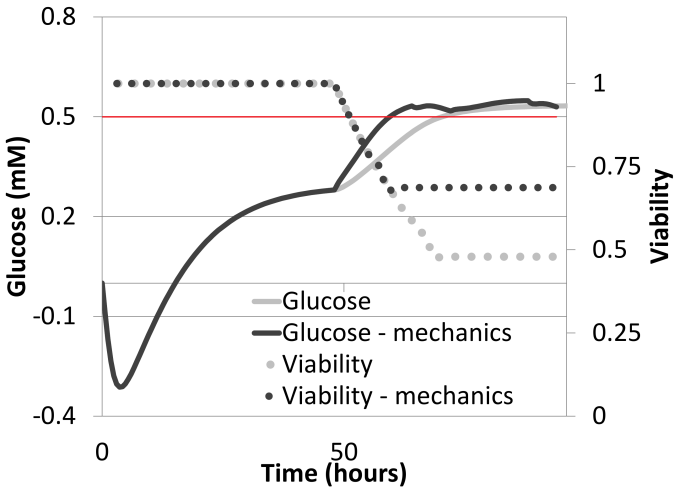

Figure 6.15: RBS case: Glucose and viability in the IVD center with and without mechanical coupling. The first 48 hours refers to preconditioning.

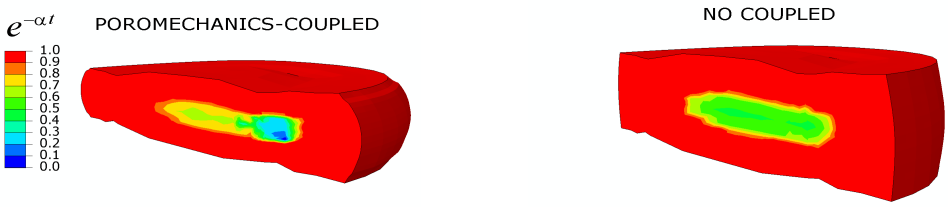

(a) (b)

Figure 6.16: Distributions of the cell viability exponentials $\exp(\alpha_{glucose}t)$ (fraction of surviving cell density). Distributions are computed at the end of the 16-hour creep of the second day simulated, with (left) and without (right) poromechanical coupling. With poromechanical coupling (left) transport and viability equations were solved over time taking into account the current deformed geometry.

6.5 Discussion

In the present chapter, a computational approach based on poromechanics and metabolism was developed and applied to investigate metabolites transport within the human IVD. The FE implementation of the transport model was verified, as was for the coupling procedure. The relevance of the mechanical and metabolic couplings was evaluated. Different degenerative changes were simulated with the proposed method to assess their effects on metabolic oxygen transport. Finally, cell death phenomena were included in case of both normal and reduced supply of metabolites at the endplates, combining with the full poromechanics-transport coupled model.

In the healthy disc, predictions for oxygen distribution were most sensitive to mechanical coupling, this effect being predominant over that of the metabolic coupling. Advective transport by fluid movements was negligible in daily loading modes and after short period of cyclic compression. Mechanical loading affect the solute transport at both local and global scales: locally, by acting directly on porosity changes that updated diffusivities and globally, due to changes in geometry that affected the diffusion distances. Unsurprisingly, mechanical effect was thus mainly observed when large volume changes were present, which was favored by healthy disc material properties. Disc height, cell density, NP swelling pressure and porosity DDCs affected more oxygen transport than AF and NP solid-phase stiffening. Cell number decay and related consequences on metabolic balance, as well as the effect of mechanics were simulated in the IVD. When metabolites supply was disturbed, cells died in the central region, modifying metabolic balance. This process was affected by disc deformation.

Effects of (i) daily disc deformation, and (ii) disc height change due to fluid loss with aging and degeneration on transport were studied. In the central disc, we found a general increase in oxygen and glucose concentration, induced by both sustained compression and permanent geometrical change. Such phenomena occurred in concomitance with a decrease of lactate levels, as a consequence of the chosen metabolic rates. These results are in agreement with other predictions (19) in which oxygen enhancement and lactate reduction were found following a volume loss, simulated by altering the IVD model dimensions. Our study further focused on the dual effect of a permanently reduced height together with daily deformations due to loading, as happens in a degenerated disc under sustained compression. While volume changes in the

simulated healthy IVD during the load-recovery phases had a remarkable effect on solute levels, in the degenerated disc model, such effect was reduced because of decreased fluid content and swelling pressure, as well as increased influence of the solid phase (Fig. 6.12). This outcome could indicate how compression, here related to the fluctuation of solute concentrations, could be seen as a "healthy" condition for the disc (181). Moreover, predicted glucose increase due to mechanical effect was shown to potentially delay cell death processes. Interestingly, the beneficial effect of compression through volumetric deformations could partly explain the fact that no differences in cell density were observed between male and female discs (179): despite the increased diffusion distances in male discs, if the disc is sufficiently healthy, large dimensions would allow for increased deformability and improved disc maintenance through mechano-transport coupling. Moreover, the observed reduction in the normal load-dependent solutes pattern that occurred when degenerated material properties were simulated could be seen as an IVD degenerative catalyst.

Distributions of oxygen and lactate predicted by our 3D model are difficult to validate as this would require invasive and complicated experimental procedures. However, a similar anteroposterior trend can be found between our study and the experimental results (172) for both lactate and oxygen concentrations. Such a comparison strongly suggests that the vertebral blood supply condition is a relevant factor that drives the absolute values predicted by any metabolic transport model and could also be relevant for the onset of possible degenerative changes, as it was seen when cell death criteria were implemented in the model. Such predicted absolute values can thus change with boundary condition chosen but also with initial cell density. The latter is visible in Fig. 6.13, since in procedure P1 cell densities were homogenized with porosities and thus reduced with respect to procedure P2. The fundamental role of cell density is also confirmed by the sensitivity study, which provides - in a model complicated to validate - a reliable picture of the influence of realistic parameter changes as measured in disc degeneration.

The different responses of the AF and NP to mechanical coupling were related to the combination of subtissue-specific deformation modes and changes in diffusivity. In fact, the changes in diffusion distance caused an increase of oxygen and a decrease of lactate in both subtissues. Also, the strain-dependent diffusivity caused a decrease of oxygen and an increase of lactate when compared to a deforming disc with constant

diffusivities, both in the AF and the NP. When strain-dependent diffusivity and shortening of diffusion distance were combined together, changes in solute concentrations were regionally opposite in the two substissues, because AF was significantly less sensitive than the NP to shortening of diffusion distance (blue lines vs. red lines in Fig. 6.9). In the anterior AF where the oxygen availability was already low, changes to diffusion-related parameters resulted in an oxygen deprivation. The location of such critical regions depends strongly on the disc geometry, distance from blood vessels, and regional water content loss, i.e. on patient specific characteristics and boundary conditions. Finally, diffusion distance shortening due to mechanical loads, in the healthy IVD model gave 15% of disc height change after 7 hours under 0.5 MPa compression, which was comparable to in vivo deformations of 10-15% measured with similar loads (200). Fluid velocity enhancement for nutrients was negligible under higher frequency and amplitude loading modes. The highest fluid velocities were around 0.5 μm/s, at 1 Hz frequency and for the A2 load amplitude. Even if a particle was submitted to such velocity magnitude permanently during the simulated 400 seconds, the advective transport distance would have been 0.2 mm. Therefore, within the AF and the NP, considering both the low tissue permeability and the characteristic dimensions two orders of magnitude higher than the advective distance, fluid velocities are unlikely to transport small solutes. Moreover, AF and NP permeability changes (although not simulated as a DDC following the experimental findings of (45)) are known to have a negligible role in the displacement field calculation (15) and thus on the IVD volume changes. Therefore, the solute transport sensitivity is expected to be negligible via load-dependent diffusion. The negligible role of fluid velocity advection is congruent with other computational (13) and experimental evidences (169, 170). Yet, Huang and coworkers (175) predicted small solute enhancements due to dynamic loadings after 200 cycles and at a frequency of 0.1 Hz. However, separate advection and diffusion results were not presented in the study of Huang *et al.* and dynamic vs. static loading differences could be also attributed in part to the loading-dependent diffusion.

The metabolites transport model was also capable to reproduce the experimental results in terms of viability profiles, when criteria for cell death were implemented. The critical values for glucose and pH were based on experimental calibration of cell viability profiles. With the assumptions made in the present study, such values were phenomenological and depended on factors such as diffusivities of solutes in agarose,

and fitted exponential decays over time. Although they are in the range that emerge from the *in vitro* studies (183, 184) and other computational investigations (18), other phenomena, such as oxygen-dependent cell death, cell proliferation and migration could eventually be considered in the future, to explain the differences between in vitro cell viability profiles and results from our phenomenological model. Nevertheless, the delay predicted for cell death due to mechanical effect that increases glucose concentration (and decrease lactate accumulation and pH drop) seems a general effect and it is believed not to depend from such critical values.

Moreover, by implementing such criteria in the whole-IVD FE model the effect of biphasic mechanics coupled with diffusion and transient responses of external loads on cell viability were studied. In the central nucleus, the delay predicted for cell death due to mechanical effect that increases glucose concentration (Fig. 6.16) seems a general effect: We believe that this does not depend from little variations around the critical glucose value that we obtained in our calibration - 0.5 mM -, which is a realistic value when compared to the in vitro results of Horner and Urban (183). Long-term steady-state deformations have been indicated either as a possible enhancement for nutritional processes, due to shortening of transport routes (114) or as detrimental for cell viability in other recent metabolic-coupled IVD FE studies (178). Although loads were applied statically over 16 h in our study, transient mechanical dependency of the cell viability could occur, for instance due to strain-dependent diffusivity and shortening of diffusion distances in an organ of non-negligible dimensions. Our methodology was able to model such phenomena, which are most likely physiologically relevant. Moreover, our study also predicted locally cell viability based on a spatial and temporal variations of porosities, volume changes and metabolism-related nutrient concentrations: In the inner annulus fibrosus, due to the combination of all these factors, cell viability was affected negatively by mechanical loads. This points out on the importance of realistic geometrical models and regional material parameters to increase the ability of the models in predicting local features which could be missed otherwise. However, the mechanical effect considered here and in other FE studies (114, 178) did not address the issue of chemical signals (e.g. inflammatory factors) which could arise due to sustained loads and that could explain the detrimental effect of sustained loads on in vitro cell cultures (201). Thus, future studies should integrate such concerns towards a more comprehensive understanding of mechanobiological phenomena within the IVD.

The study of cell viability changes within the IVD, the sensitivity study, as well as the differences when implementing P1 and P2 procedure, all confirm that cell density disturbance had a significant effect, since it is related with both reactive (metabolic) terms for oxygen lactate and glucose. Cell density decrease has also been related to poor nutrient supply due to abnormalities of the CEP (179). Predicted absolute concentration values will depend greatly on cell density input. For instance, the total number of cells have also been shown to increase with degeneration (46). Our simulated decrease in cell density could be optimistic with respect to a situation in which a non-functional cell number increase would occur and thus, a more severe condition in terms of metabolites consumption and production.

In summary, the developed method to investigate the poromechanics and metabolic-coupled transport revealed that mechanical loads can significantly affect oxygen, glucose and lactate predictions when large and prolonged volume changes are involved. Such phenomenon was caused by the deformation-dependent nature of both tissue diffusivity and diffusion distances. The mechanism was regional- and solute-dependent within the disc. By applying the proposed approach together with IVD degenerative changes, we conclude that cell density drop, disc height reduction and decrease in NP swelling pressure due to loss of proteoglycans would significantly alter the interactions between mechanical loading and disc nutrition and be detrimental to the diffusion of nutrients. In a healthy disc, it was found that mean compressive load variations in a daily cycle could be beneficial to disc maintenance. By combining the effect of disc mechanics with cell number decay and related consequences on metabolic balance, it was found that if metabolites supply is disturbed, as could happen with endplate calcification or circulatory diseases, cells died in the central region, modifying metabolic balance and that such process was delayed when disc deformation was considered. Thus, disc nutrition is most likely part of the synergy suggested between disc degeneration and physical activity (74). The approach could be used in regenerative and preventive medicine as a patient-specific numerical tool to explore the chronology of events in disc degeneration, in which the input parameters (such as geometry, diffusivity, hydration) could be also derived from diagnostic images. The computational framework developed will also serve to study cell-loaded disc substitute materials.

7

Discussion and conclusive remarks

The present thesis was focused on the biomechanics and transport of metabolites of the human intervertebral disc, in healthy and pathological conditions. A computational approach that locally models both phenomena has been presented.

By using poroelasticity, fluid and solid phases in both the discs and the vertebrae were coupled together. The concept of relevance of fluid phase to the local biomechanics as well as to the transport phenomena within the intervertebral disc has been reexamined. In Chapter 3, the permeabilities of the annulus fibrosus and of the cartilage endplate - related with the fluid exchanges at the disc boundaries were shown to influence the local and global biomechanics of the disc. In particular, the cartilaginous part of the endplate route was the most relevant permeability involved, confirming its role for the proper disc mechanics (9, 28, 29). Additionally, in Chapter 5, the local fluid dynamics at the bony part of the endplate was studied based on human vertebral bone microtomographic images confirming that the permeability related to the vertebral bony endplate is much higher than the one of the cartilagineous endplate, also for very low bone porosities, which again points out on the importance of the cartilage at the interface vertebra-disc. Furthermore, as also shown by other authors (18, 29, 177), pathologies related to the cartilagineous part of the endplate such as calcification, could be the main process responsible in altering the exchange of nutrient with the boundaries, by acting on the porosity and thus on the metabolites diffusivity and reducing the supply of such metabolites. Indeed, if the latter phenomena is directly simulated,

as in Chapter 6, cell viability is negatively affected.

The stiffness of both the annulus and nucleus solid phases are highly relevant for the biomechanical response of the disc (Chapter 3). The effective stiffness of the annulus highly depends on the oriented network of collagen fibers. Therefore, collagen fibres orientations were back-calculated (Chapter 4) to reproduce regional differences in mechanical response measured experimentally. Realistic orientations were obtained in the present study, and, when implemented in the poromechanical whole-disc model, pressures and displacements were within the range of those physically experienced by healthy discs. Although relevant to the segmental movements and pressures, the stiffening of the annulus and nucleus solid phases (as degenerative change) appeared later on negligible in affecting the transport of metabolites (Chapter 6), if separated by the other factors. The disc shape, the fluid content, the lost of swelling pressure and the cell density were much more relevant to the diffusion of solutes. Thus, it is proposed that a loss of fluid and osmotic effect is more important to monitor than a biochemical change affecting the stiffness of the solid matrix (through a change of collagen and aggrecan composition mostly) to study the disc degeneration changes through the transport of metabolites within the disc.

Continuum micromechanics was adopted for the human vertebral bone and combined with an experimental set-up to find out anisotropic poromechanical properties that are relevant to the multiscale modeling of spinal segments (Chapter 5). While a useful characterization of the vertebral bone has been accomplished, the theoretical approach is expected to be extended in a near future to the cartilaginous tissues (and therefore coupled to the large strains experienced therein), and fully integrated with the present results.

The multiscale issue of coupling the transport of relevant biomolecule for disc cells with the local continuum poromechanics of the intervertebral disc was studied in Chapter 6. The approach allowed relating the local changes in metabolites concentrations with the application of external forces. Cyclic compressive loads did not enhance advection phenomena in the healthy disc. Only in the case of large mechanical volume changes - occurring under sustained compressive loads and with healthy disc properties - non-negligible changes in concentrations were calculated because of mechanically-dependent diffusive phenomena, such as the shortening of diffusion distances during compression and the local changes of porosity that affect diffusivity. It was found out

that, depending on subtissues properties, such mechanical effect can enhance nutrients and reduce metabolic waste accumulation (as happened in the central disc). Therefore, as final biologically-relevant issue, this effect was related with the cell viability, showing how the central disc could benefit from such poromechanics-dependent variation in metabolites concentrations.

The present study has major limitations to discuss. First, the mechanical model must be validated more extensively, in particular in its capacity to correctly reproduce the pressures and velocities experienced *in vivo*. For that, more sophisticated constitutive models could be used to describe the osmotic swelling and the intrinsic viscoelasticity of both the nucleus and the annulus, more accurate for loads at high-frecuencies as those experienced *in vivo*. Second, the procedure to couple the mechanical and the transport model could be further investigated, since modeling the transport of solutes in a deformable, porous media is still an open issue, and several theoretical approaches are currently available in the literature (202, 203). Third, the metabolic transport model was compared to few measurements of oxygen and lactate in the literature, due to the intrinsic experimental difficulty of these types of measurements, as discussed in Chapter 6. Moreover, it should also be considered that several parameters are used in the coupled model taken from different experimental works, and that this can reduce the reliability of the model predictions.

It is worth to note, however, that the present approach succeeded in unraveling important features within the complexity of the multiscale problem that is meant to reproduce. In doing this, the approach was able to model local phenomena in a simplified, homogenized continuum. Namely, porosity changes after loading were related to the hydraulic permeability changes and to the solute diffusivity changes. These phenomena were in turn related to the local spatial and transient output of solute concentrations. Such coupling, being relevant to explore new mechanobiological connections can provide valuable insights, despite the particular values chosen for the parameters. However, in the case when a comprehensive validation is difficult to perform, a detailed picture of the sensitivity of the model to the changes in values is mandatory.

Indeed, the sensitivity studies performed throughout the present work are clearly pointing out the most important parameter to monitor. Both sensitivity studies were conducted varying the parameters over realistic ranges, related with both healthy and pathological cases. The response of the model to such parameter changes gave robust

arguments of discussion, even in absence of a more comprehensive validation. For instance, the relevance of the porosity in the response of the transport model can be clinically useful to give indications based on image-derived fluid content measurements. Another example can be made for the sensitivity of the model to the cell density parameter: The concentrations of metabolites highly depended on the spatial and temporal evolution of cell densities within the disc. As a consequence, the present work highlights the need of a high accuracy in model and measure reliable cell distributions over time and space. In general these sensitivity results provided a list of parameters - cell density, porosity, osmotic pressure, disc height - among several interconnected factors and their pathological evolutions that emerged as possible degenerative catalysts.

Relevantly to the field of *regenerative medicine*, the same parameters consequently could be indicated as key factors for the success of regenerative strategies. Also, the studies on cartilage endplate properties indicated that a normal fluid resistance capability is mandatory for the disc biomechanics, and that cartilage endplate also guarantees a normal supply and cellular metabolic balance for cells. Therefore, the restoration to a "healthy" cartilaginous endplate could be fundamental to guarantee a mechanical but also nutritional balance in the human intervertebral disc. Furthermore, a normal disc height and shape combined with a high compliance appeared also as fundamental for maintaining a mechanical effect on transport of metabolites and could be related as well with the success of regenerative therapies. This mechanical effect could be analyzed over time and space in our study, and it was found that it could enhance glucose and oxygen concentration and reduce lactate accumulation, thus ensuring a benefit for cell viability in the central disc region. This aspect could be controlled when designing biomaterial substitutes, providing further arguments against the current techniques that involve vertebral fixation and implants that would limit compliance and flexibility of the intervertebral articulations.

The model developed in the present work was also *methodologically* innovative since it showed how mechanical and biological complexities could be coupled together and how they interact. Recognizing and understanding the physics of the mechanical effect on transport will open new strategies, and the present work helps in designing a reliable numerical procedure to associate the local disc mechanics to the cellular environment. For instance, such "indirect" mechanical effect can be considered together with the one

directly sensed by disc cells (e.g. via solid deformation and fluid shear stresses) and open an unprecedented path in the field of mechanobiological models of soft tissues.

Finally, there are several procedures developed in the present work that could have *clinical applications*. Medical, patient-specific images could be used to obtain fiber angles and thus accurately reproduce the particular local annulus mechanics of a given patient by using the approach of Chapter 4. Tomographic images could be used to map trabecular bone mean orientation and bone volume fraction and, in combination with the elasticity and poroelasticity quantities obtained in Chapter 5 for the human vertebral solid bone matrix, to investigate in a patient-specific fashion the local load sharing between vertebra and disc. Bone volume fraction from high resolution CT scans could also be used to obtain hydraulic permeability values at the thin interfaces vertebra-disc thanks to the porosity-permeability relationships provided for the human vertebral bone. As a final application, the coupled mechano-transport model can be combined with medical images in order to be applied to patient-specific geometries and image-derived fluid content and diffusivities to understand in real, specific situations the mechanical and geometrical effects on metabolic transport and to support clinical decision-making processes related to disc pathologies and regenerative strategies.

References

[1] L Womersley and S May. **Sitting posture of subjects with postural backache.** *Journal of Manipulative and Physiological Therapeutics*, **29**(3):213–218, 2006. 1

[2] W Dankaerts, P O'Sullivan, A Burnett, and L Straker. **Differences in sitting postures are associated with nonspecific chronic low back pain disorders when patients are subclassified.** *Spine*, **31**(6):698–704, 2006. 1

[3] K Luoma, H Riihimäki, R Luukkonen, R Raininko, E Viikari-Juntura, and A Lamminen. **Low back pain in relation to lumbar disc degeneration.** *Spine*, **25**(4):487–492, 2000. 1

[4] A Maetzel and L Li. **The economic burden of low back pain: a review of studies published between 1996 and 2001**. *Best Practice & Research Clinical Rheumatology*, **16**(1):23–30, 2002. 1

[5] N Maniadakis and A Gray. **The economic burden of back pain in the UK.** *Pain*, **84**(1):95–103, 2000. 1

[6] B F Walker, R Muller, and W D Grant. **Low back pain in Australian adults: the economic burden.** *AsiaPacific journal of public health AsiaPacific Academic Consortium for Public Health*, **15**(2):79–87, 2003. 1

[7] J A Buckwalter. **Aging and degeneration of the human intervertebral disc.** *Spine*, **20**(11):1307–1314, 1995. 1, 12, 14

[8] S Holm and A Nachemson. **Nutrition of the intervertebral disc: acute effects of cigarette smoking. An experimental animal study.** *Upsala Journal of Medical Sciences*, **93**(1):91–99, 1988. 1

[9] J P G Urban, S Smith, and J C T Fairbank. **Nutrition of the intervertebral disc.** *Spine*, **29**(23):2700–9, December 2004. 1, 10, 13, 14, 101, 105, 131

[10] Y M Lu, W C Hutton, and V M Gharpuray. **Do bending, twisting, and diurnal fluid changes in the disc affect the propensity to prolapse? A viscoelastic finite element model.** *Spine*, **21**(22):2570–2579, 1996. 1, 52

[11] M A Adams, B J Freeman, H P Morrison, I W Nelson, and P Dolan. **Mechanical initiation of intervertebral disc degeneration.** *Spine*, **25**(13):1625–1636, 2000. 1

[12] M A Swartz and M E Fleury. **Interstitial flow and its effects in soft tissues.** *Annual review of biomedical engineering*, **9**:229–56, January 2007. 2

[13] S J Ferguson, K Ito, and L P Nolte. **Fluid flow and convective transport of solutes within the intervertebral disc**. *Journal of Biomechanics*, **37**(2):213–221, February 2004. 2, 23, 28, 29, 31, 46, 52, 53, 62, 100, 103, 110, 111, 128

[14] A H Hsieh, D R Wagner, L Y Cheng, and J C Lotz. **Dependence of Mechanical Behavior of the Murine Tail Disc on Regional Material Properties: A Parametric Finite Element Study**. *Journal of Biomechanical Engineering*, **127**(7):1158, 2005. 2, 43

[15] A Malandrino, J A Planell, and D Lacroix. **Statistical factorial analysis on the poroelastic material properties sensitivity of the lumbar intervertebral disc under compression, flexion and axial rotation.** *Journal of biomechanics*, **42**(16):2780–8, December 2009. 2, 53, 67, 69, 128

[16] M Argoubi and A Shirazi-Adl. **Poroelastic creep response analysis of a lumbar motion segment in compression.** *Journal of biomechanics*, **29**(10):1331–9, October 1996. 2, 23, 29, 30, 38, 44, 45, 46

[17] Y Schroeder, W Wilson, J M Huyghe, and F P T Baaijens. **Osmoviscoelastic finite element model of the intervertebral disc.** *European spine journal : official publication of the European Spine Society, the European Spinal Deformity Society, and the European Section of the Cervical Spine Research Society*, **15 Suppl 3**:S361–71, August 2006. 2, 38, 46

[18] A Shirazi-Adl, M Taheri, and J P G Urban. **Analysis of cell viability in intervertebral disc: Effect of endplate permeability on cell population**. *Journal of biomechanics*, pages 1–7, 2010. 2, 100, 102, 108, 129, 131

[19] D M Mokhbi Soukane, A Shirazi-Adl, and J P G Urban. **Computation of coupled diffusion of oxygen, glucose and lactic acid in an intervertebral disc**. *Journal of Biomechanics*, **40**(12):2645–2654, 2007. 2, 100, 126

[20] Wikipedia. **Lumbar vertebrae — Wikipedia, The Free Encyclopedia**, 2012. [Online; accessed 10-February-2012]. 6

[21] I A Kapandji. *The Physiology of the Joints, 5th ed.* Churchill Livingstone, 1987. 6, 7

[22] Wikipedia. **Intervertebral disc — Wikipedia, The Free Encyclopedia**, 2011. [Online; accessed 10-February-2012]. 7

[23] M L Goins, D W Wimberley, P S Yuan, L N Fitzhenry, and A R Vaccaro. **Nucleus pulposus replacement: an emerging technology.** *The spine journal official journal of the North American Spine Society*, **5**(6 Suppl):317S–324S, 2005. 8

[24] D R Eyre. **Biochemistry of the intervertebral disc.** *International review of connective tissue research*, **8**:227–91, January 1979. 8, 12

[25] M L Schollum, P A Robertson, and N D Broom. **ISSLS prize winner: microstructure and mechanical disruption of the lumbar disc annulus: part I: a microscopic investigation of the translamellar bridging network.** *Spine*, **33**(25):2702–10, December 2008. 9

REFERENCES

[26] J M Cloyd and D M Elliott. **Elastin content correlates with human disc degeneration in the anulus fibrosus and nucleus pulposus.** *Spine*, **32**(17):1826–31, August 2007. 9

[27] M B Coventry, R K Ghormley, and J W Kernohan. **The Intervertebral Disc : Its Microscopic Anatomy And Pathology : Part I . Anatomy , Development , and Physiology**. *The Journal of Bone and Joint Surgery*, **27**(1):105–112, 1945. 9

[28] S Roberts, J Menage, and J P Urban. **Biochemical and structural properties of the cartilage end-plate and its relation to the intervertebral disc.** *Spine*, **14**(2):166–174, 1989. 9, 131

[29] D C Ayotte, K Ito, and S Tepic. **Direction-dependent resistance to flow in the endplate of the intervertebral disc: an ex vivo study.** *Journal of orthopaedic research : official publication of the Orthopaedic Research Society*, **19**(6):1073–7, November 2001. 9, 27, 67, 71, 84, 95, 131

[30] F Accadbled, J M Laffosse, D Ambard, A Gomez-Brouchet, J S de Gauzy, and P Swider. **Influence of location, fluid flow direction, and tissue maturity on the macroscopic permeability of vertebral end plates.** *Spine*, **33**(6):612–9, March 2008. 9, 71, 95, 111

[31] A H Hsieh and J D Twomey. **Cellular mechanobiology of the intervertebral disc: new directions and approaches.** *Journal of biomechanics*, **43**(1):137–45, January 2010. 9, 101

[32] T R Oegema. **Biochemistry of the intervertebral disc.** *Clinics in Sports Medicine*, **12**(3):419–439, 1993. 9

[33] C Neidlinger-Wilke, A Liedert, K Wuertz, Z Buser, C Rinkler, W Käfer, A Ignatius, L Claes, S Roberts, and Johnson W E. **Mechanical stimulation alters pleiotrophin and aggrecan expression by human intervertebral disc cells and influences their capacity to stimulate endothelial migration**. *Spine*, **34**(7):663– 669, 2009. 9, 45

[34] A Maroudas, R a Stockwell, A Nachemson, and J P G Urban. **Factors involved in the nutrition of the human lumbar intervertebral disc: cellularity and diffusion of glucose in vitro.** *Journal of anatomy*, **120**(Pt 1):113–30, September 1975. 9, 110, 112

[35] S R S Bibby, D A Jones, R B. Lee, J Yu, and J P G Urban. **Pathophysiology of the intervertebral disc**. *Joint Bone Spine*, **68**:537–42, February 2001. 10, 11, 14, 23

[36] Wikipedia. **Glycolysis — Wikipedia, The Free Encyclopedia**, 2011. [Online; accessed 5-September-2011]. 11

[37] H Ishihara and J P Urban. **Effects of low oxygen concentrations and metabolic inhibitors on proteoglycan and protein synthesis rates in the intervertebral disc.** *Journal of Orthopaedic Research*, **17**(6):829–835, 1999. 11

[38] J P Thompson, R H Pearce, M T Schechter, M E Adams, I K Tsang, and P B Bishop. **Preliminary evaluation of a scheme for grading the gross morphology of the human intervertebral disc.** *Spine*, **15**(5):411–415, 1990. 12, 13, 111

[39] C W Pfirrmann, A Metzdorf, M Zanetti, J Hodler, and N Boos. **Magnetic resonance classification of lumbar intervertebral disc degeneration.** *Spine*, **26**(17):1873–1878, 2001. 12, 13

[40] J C Iatridis, L a Setton, M Weidenbaum, and V C Mow. **Alterations in the mechanical behavior of the human lumbar nucleus pulposus with degeneration and aging.** *Journal of orthopaedic research : official publication of the Orthopaedic Research Society*, **15**(2):318–22, March 1997. 12, 13, 110

[41] W Johannessen and D M Elliott. **Effects of degeneration on the biphasic material properties of human nucleus pulposus in confined compression.** *Spine*, **30**(24):E724–9, December 2005. 12, 13, 23, 25, 27, 29, 48, 49, 51, 59, 64, 110

[42] W Y Gu, X G Mao, R J Foster, M Weidenbaum, V C Mow, and B A Rawlins. **The anisotropic hydraulic permeability of human lumbar anulus fibrosus. Influence of age, degeneration, direction, and water content.** *Spine*, **24**(23):2449–55, December 1999. 12, 13, 22, 27, 29, 110

[43] C W A Pfirrmann, A Metzdorf, A Elfering, J Hodler, and N Boos. **Effect of Aging and Degeneration on Disc Volume and Shape : A Quantitative Study in Asymptomatic Volunteers**. *Journal of Orthopaedic Research*, (May):1086–1094, 2006. 12, 110, 111

[44] A M Nguyen, W Johannessen, J H Yoder, A J Wheaton, E J Vresilovic, A Borthakur, and D M Elliott. **Noninvasive quantification of human nucleus pulposus pressure with use of T1rho-weighted magnetic resonance imaging.** *The Journal of bone and joint surgery. American volume*, **90**(4):796–802, April 2008. 12

[45] J C Iatridis, L a Setton, R J Foster, B a Rawlins, M Weidenbaum, and V C Mow. **Degeneration affects the anisotropic and nonlinear behaviors of human anulus fibrosus in compression.** *Journal of biomechanics*, **31**(6):535–44, June 1998. 13, 23, 25, 27, 45, 101, 110, 128

[46] A G Rodriguez, C K Slichter, F L Acosta, A E Rodriguez-Soto, A J Burghardt, S Majumdar, and J C Lotz. **Human Disc Nucleus Properties and Vertebral Endplate Permeability.** *Spine*, **36**(7):512–520, January 2011. 13, 14, 110, 111, 130

[47] L M Benneker, P F Heini, M Alini, S E Anderson, and K Ito. **2004 Young Investigator Award Winner: vertebral endplate marrow contact channel occlusions and intervertebral disc degeneration.** *Spine*, **30**(2):167–73, January 2005. 14

[48] S Rajasekaran, J N Babu, R Arun, B R W Armstrong, A P Shetty, and S Murugan. **ISSLS prize winner: A study of diffusion in human lumbar discs: a serial magnetic resonance imaging study documenting the influence of the endplate on diffusion in normal and degenerate discs.** *Spine*, **29**(23):2654–2667, 2004. 14

[49] A G Rodriguez, A E Rodriguez-Soto, A J Burghardt, S Berven, S Majumdar, and J C Lotz. **Morphology of the human vertebral endplate.** *Journal of Orthopaedic Research*, pages 1–8, 2011. 14

[50] V C Mow, S C Kuei, W M Lai, and C G Armstrong. **Biphasic creep and stress relaxation of articular cartilage in compression? Theory and experiments**. *Journal of Biomechanical Engineering*, **102**(1):73–84, 1980. 15, 19

[51] C Truesdell and R A Toupin. *The Classical Field Theories*, **III/1** of *Handbuch der Physik*, pages 226–793. Springer, 1960. 15, 19

[52] S C Cowin. **The specific growth rates of tissues: a review and a re-evaluation.** *Journal of biomechanical engineering*, **133**(4):041001, April 2011. 15

[53] M A Biot. **General Theory of Three-Dimensional Consolidation**. *Journal of applied physics*, **12**(2):155–164, 1941. 15, 18, 19, 80, 94

[54] E Almeida and R Spilker. **Mixed and Penalty Finite Element Models for the Nonlinear Behavior of Biphasic Soft Tissues in Finite Deformation: Part I Alternate Formulations**. *Computer Methods in Biomechanics and Biomedical Engineering*, **1**(1):25–46, 1997. 17, 47, 48

[55] B R Simon. **Multiphase Poroelastic Finite Element Models for Soft Tissue Structures**. *Applied Mechanics Reviews*, **45**(6):191–218, 1992. 18

[56] Jacques M Huyghe and J D Janssen. **Quadriphasic Mechanics of Swelling Incompressible Porous Media**. *International Journal of Engineering Science*, **35**(8):793–802, 1997. 18, 20, 45, 46

[57] K Terzaghi. *Theoretical Soil Mechanics*. John Wiley and Sons, 1943. 19

[58] C Mccutchen. **The frictional properties of animal joints**. *Wear*, **5**(1):1–17, 1962. 19

[59] I Fatt and B O Hedbys. **Flow conductivity of human corneal stroma.** *Experimental Eye Research*, **10**(2):237–242, 1970. 19

[60] D E Kenyon. **A mathematical model of water flux through aortic tissue.** *Bulletin of Mathematical Biology*, **41**(1):79–90, 1979. 19

[61] B R Simon, J S S Wu, M W Carlton, J H Evans, and L E Kazarian. **Structural models for human spinal motion segments based on a poroelastic view of the intervertebral disk**. *Journal of Biomechanical Engineering*, **107**(4):327–335, 1985. 19

[62] M H Holmes and V C Mow. **The nonlinear characteristics of soft gels and hydrated connective tissues in ultrafiltration.** *Journal of Biomechanics*, **23**(11):1145–1156, 1990. 19, 47, 110

[63] E S Almeida and R L Spilker. **Finite element formulations for hyperelastic transversely isotropic biphasic soft tissues**. *Computer Methods in Applied Mechanics and Engineering*, **151**(3-4):513–538, 1998. 19

[64] M H Holmes. **Finite deformation of soft tissue: analysis of a mixture model in uni-axial compression.** *Journal of Biomechanical Engineering*, **108**(4):372–381, 1986. 20, 30, 48

[65] W M Lai and V C Mow. **Drag-induced compression of articular cartilage during a permeation experiment.** *Biorheology*, **17**(1-2):111–123, 1980. 20, 30

[66] W M Lai, J S Hou, and V C Mow. **A triphasic theory for the swelling and deformation behaviors of articular cartilage.** *Journal of biomechanical engineering*, **113**(3):245–58, August 1991. 20

[67] W Wilson, C C van Donkelaar, and J M Huyghe. **A Comparison Between Mechano-Electrochemical and Biphasic Swelling Theories for Soft Hydrated Tissues**. *Journal of Biomechanical Engineering*, **127**(1):158, 2005. 20, 46, 50, 51, 64

[68] Y Lanir. **Biorheology and fluid flux in swelling tissues. I. Bicomponent theory for small deformations, including concentration effects.** *Biorheology*, **24**(2):173–187, 1987. 20, 46, 50, 51

[69] A Nachemson. **Lumbar intradiscal pressure. Experimental studies on post-mortem material.** *Acta orthopaedica Scandinavica Supplementum*, **43**:1–104, 1960. 21

[70] A Nachemson and J Morris. **In Vivo Measurements of Intradiscal Pressure**. *Journal of Bone and Joint Surgery*, **46-A**(5):1077–1092, 1964. 21

[71] H J Wilke, P Neef, M Caimi, T Hoogland, and L E Claes. **New in vivo measurements of pressures in the intervertebral disc in daily life.** *Spine*, **24**(8):755–62, April 1999. 21, 31

[72] D S McNally and M Adams. **Internal intervertebral disc mechanics as revealed by stress profilometry**. *Spine*, **17**(1):66–73, 1992. 21

[73] D S McNally, M A Adams, and A E Goodship. **Development and validation of a new transducer for intradiscal pressure measurement.** *Journal of Biomedical Engineering*, **14**(6):495–498, 1992. 21

[74] M A Adams, P Dolan, and D S McNally. **The internal mechanical functioning of intervertebral discs and articular cartilage, and its relevance to matrix biology.** *Matrix biology : journal of the International Society for Matrix Biology*, **28**(7):384–9, September 2009. 21, 101, 130

[75] B A Best, F Guilak, L A Setton, W Zhu, F Saed-Nejad, A Ratcliffe, M Weidenbaum, and V C Mow. **Compressive mechanical properties of the human anulus fibrosus and their relationship to biochemical composition**. *Spine*, **19**(2):212, 1994. 21, 45, 48, 110

[76] J C Iatridis, M Weidenbaum, L A Setton, and V C Mow. **Is the nucleus pulposus a solid or a fluid? Mechanical behaviors of the nucleus pulposus of the human intervertebral disc.** *Spine*, **21**(10):1174–1184, 1996. 22, 110

REFERENCES

[77] D Périé, D Korda, and J C Iatridis. **Confined compression experiments on bovine nucleus pulposus and annulus fibrosus: sensitivity of the experiment in the determination of compressive modulus and hydraulic permeability.** *Journal of biomechanics*, **38**(11):2164–71, November 2005. 22, 45, 49, 53, 62, 110

[78] R N Natarajan, J R Williams, and G B J Andersson. **Modeling changes in intervertebral disc mechanics with degeneration.** *The Journal of bone and joint surgery. American volume*, **88 Suppl 2**:36–40, April 2006. 23, 25, 27, 28, 29, 110

[79] J C Gan, P Ducheyne, E Vresilovic, and I M Shapiro. **Bioactive glass serves as a substrate for maintenance of phenotype of nucleus pulposus cells of the intervertebral disc.** *Journal of biomedical materials research*, **51**(4):596–604, September 2000. 23

[80] P a Revell, E Damien, L Di Silvio, N Gurav, C Longinotti, and L Ambrosio. **Tissue engineered intervertebral disc repair in the pig using injectable polymers.** *Journal of materials science. Materials in medicine*, **18**(2):303–8, February 2007. 23

[81] J C Iatridis, J P Laible, and M H Krag. **Influence of fixed charge density magnitude and distribution on the intervertebral disc: applications of a poroelastic and chemical electric (PEACE) model.** *Journal of Biomechanical Engineering*, **125**(1):12–24, 2003. 23

[82] J P Laible, D S Pflaster, M H Krag, B R Simon, and L D Haugh. **A poroelastic-swelling finite element model with application to the intervertebral disc.** *Spine*, **18**(5):659–670, 1993. 23, 45

[83] R N Natarajan, J R Williams, and G B J Andersson. **Recent advances in analytical modeling of lumbar disc degeneration.** *Spine*, **29**(23):2733–41, December 2004. 23

[84] J R Williams, R N Natarajan, and G B J Andersson. **Inclusion of regional poroelastic material properties better predicts biomechanical behavior of lumbar discs subjected to dynamic loading.** *Journal of biomechanics*, **40**(9):1981–7, January 2007. 23, 53, 110, 111

[85] M Viceconti, S Olsen, L P Nolte, and K Burton. **Extracting clinically relevant data from finite element simulations.** *Clinical biomechanics (Bristol, Avon)*, **20**(5):451–4, June 2005. 24

[86] A A Rao and G A Dumas. **Influence of material properties on the mechanical behaviour of the L5-S1 intervertebral disc in compression: a nonlinear finite element study.** *Journal of Biomedical Engineering*, **13**(2):139–151, 1991. 24, 40

[87] M J Fagan, S Julian, D J Siddall, and A M Mohsen. **Patient-specific spine models. Part 1: Finite element analysis of the lumbar intervertebral disc–a material sensitivity study.** *Proceedings of the Institution of Mechanical Engineers Part H Journal of engineering in medicine*, **216**(5):299–314, 2002. 24

[88] H W Ng, E C Teo, and V S Lee. **Statistical factorial analysis on the material property sensitivity of the mechanical responses of the C4-C6 under compression, anterior and posterior shear.** *Journal of biomechanics*, **37**(5):771–7, May 2004. 24, 40

[89] D C Montgomery. **Design and Analysis of Experiments**. *Design*, **48**(1):158–158, 2001. 25, 28, 29, 30, 32

[90] J Noailly, H J Wilke, J A Planell, and D Lacroix. **How does the geometry affect the internal biomechanics of a lumbar spine bi-segment finite element model? Consequences on the validation process.** *Journal of biomechanics*, **40**(11):2414–25, January 2007. 25, 26, 28, 44, 45, 51, 52, 53, 97

[91] J Noailly. *Model developments for in silico studies of the lumbar spine biomechanics*. PhD thesis, Universidad Politécnica de Cataluña, Barcelona, Spain, 2009. 25, 51

[92] F Heuer, H Schmitt, H Schmidt, L Claes, and H J Wilke. **Creep associated changes in intervertebral disc bulging obtained with a laser scanning device.** *Clinical biomechanics (Bristol, Avon)*, **22**(7):737–44, August 2007. 26, 53, 59, 60, 61, 64

[93] M H Krag, M C Cohen, L D Haugh, and M H Pope. **Body height change during upright and recumbent posture.** *Spine*, **15**(3):202–207, 1990. 26

[94] A R Tyrrell, T Reilly, and J D Troup. **Circadian variation in stature and the effects of spinal loading.** *Spine*, **10**(2):161–164, 1985. 26, 31, 32

[95] B Reynaud and T M Quinn. **Anisotropic hydraulic permeability in compressed articular cartilage.** *Journal of biomechanics*, **39**(1):131–7, January 2006. 27, 29

[96] E A Nauman, K E Fong, and T M Keaveny. **Dependence of intertrabecular permeability on flow direction and anatomic site.** *Annals of biomedical engineering*, **27**(4):517–24, 1999. 27, 29, 90, 95, 96, 110

[97] Inc Minitab. **Minitab Statistical Software**, 2007. 29, 31, 86

[98] W Schmoelz, J F Huber, T Nydegger, L Claes, and H J Wilke. **Influence of a dynamic stabilisation system on load bearing of a bridged disc: an in vitro study of intradiscal pressure.** *European spine journal : official publication of the European Spine Society, the European Spinal Deformity Society, and the European Section of the Cervical Spine Research Society*, **15**(8):1276–85, August 2006. 31

[99] K B Broberg. **Slow deformation of intervertebral discs.** *Journal of Biomechanics*, **26**(4-5):501–512, 1993. 38

[100] P E Riches and D S McNally. **A one-dimensional theoretical prediction of the effect of reduced end–plate permeability on the mechanics of the intervertebral disc.** *Proceedings of the Institution of Mechanical Engineers Part H Journal of engineering in medicine*, **219**(5):329–335, 2005. 40

[101] R Eberlein, G A Holzapfel, and C A J Schulze-Bauer. **An Anisotropic Model for Annulus Tissue and Enhanced Finite Element Analyses of Intact Lumbar Disc Bodies**. *Computer Methods in Biomechanics and Biomedical Engineering*, **4**(3):209–229, 2001. 43, 45, 49, 63

[102] D R Wagner and J C Lotz. **Theoretical model and experimental results for the nonlinear elastic behavior of human annulus fibrosus.** *Journal of orthopaedic research : official publication of the Orthopaedic Research Society*, **22**(4):901–9, July 2004. 43

[103] B R Simon, M V Kaufmann, M A McAfee, A L Baldwin, and L M Wilson. **Identification and determination of material properties for porohyperelastic analysis of large arteries**. *Journal of biomechanical engineering*, **120**:188–194, 1998. 43

[104] S Ebara, J C Iatridis, L A Setton, R J Foster, V C Mow, and M Weidenbaum. **Tensile properties of nondegenerate human lumbar anulus fibrosus.** *Spine*, **21**(4):452–461, 1996. 44, 49, 58

[105] G a Holzapfel, C A J Schulze-Bauer, G Feigl, and P Regitnig. **Single lamellar mechanics of the human lumbar anulus fibrosus.** *Biomechanics and modeling in mechanobiology*, **3**(3):125–40, March 2005. 44, 45, 58, 62, 63

[106] D Zhu, G Gu, W Wu, H Gong, W Zhu, T Jiang, and Z Cao. **Micro-structure and mechanical properties of annulus fibrous of the L4-5 and L5-S1 intervertebral discs.** *Clinical Biomechanics*, **23 Suppl 1**:S74–S82, 2008. 44, 63

[107] J J Cassidy, A Hiltner, and E Baer. **Hierarchical Structure of the Intervertebral Disc**. *Connective Tissue Research*, **23**(1):75–88, January 1989. 44, 58, 62, 63

[108] J Noailly, J A Planell, and D Lacroix. **On the collagen criss-cross angles in the annuli fibrosi of lumbar spine finite element models.** *Biomechanics and Modeling in Mechanobiology*, 2010. 44, 45, 62, 63

[109] F Marchand and A M Ahmed. **Investigation of the laminate structure of lumbar disc anulus fibrosus.** *Spine*, **15**(5):402–410, 1990. 44

[110] R Eberlein, G A Holzapfel, and M Fröhlich. **Multi-segment FEA of the human lumbar spine including the heterogeneity of the annulus fibrosus**. *Computational Mechanics*, **34**(2):147–163, April 2004. 44

[111] H Schmidt, F Heuer, U Simon, A Kettler, A Rohlmann, L Claes, and H J Wilke. **Application of a new calibration method for a three-dimensional finite element model of a human lumbar annulus fibrosus.** *Clinical biomechanics (Bristol, Avon)*, **21**(4):337–44, May 2006. 44, 52, 62

[112] S Wognum, J M Huyghe, and F P T Baaijens. **Influence of osmotic pressure changes on the opening of existing cracks in 2 intervertebral disc models.** *Spine*, **31**(16):1783–1788, 2006. 45

[113] S Olsen and A Oloyede. **A finite element analysis methodology for representing the articular cartilage functional structure.** *Computer Methods in Biomechanics and Biomedical Engineering*, **5**(6):377–386, 2002. 46

[114] F Galbusera, A Mietsch, H Schmidt, H J Wilke, and C Neidlinger-Wilke. **Effect of intervertebral disc degeneration on disc cell viability: a numerical investigation**. *Computer Methods in Biomechanics and Biomedical Engineering*, **0**(0):1–10, 0. 46, 64, 129

[115] E S Almeida and R L Spilker. **Mixed and Penalty Finite Element Models for the Nonlinear Behavior of Biphasic Soft Tissues in Finite Deformation: Part II - Nonlinear Examples**. *Computer Methods in Biomechanics and Biomedical Engineering*, **1**(2):151–170, 1997. 47, 53, 55, 110, 111

[116] T Christian Gasser, R W Ogden, and G A Holzapfel. **Hyperelastic modelling of arterial layers with distributed collagen fibre orientations.** *Journal of the Royal Society, Interface / the Royal Society*, **3**(6):15–35, March 2006. 49

[117] V K Goel, B T Monroe, L G Gilbertson, and P Brinckmann. **Interlaminar shear stresses and laminae separation in a disc. Finite element analysis of the L3-L4 motion segment subjected to axial compressive loads.** *Spine*, **20**(6):689–698, 1995. 52

[118] F Heuer, H Schmidt, and H J Wilke. **The relation between intervertebral disc bulging and annular fiber associated strains for simple and complex loading.** *Journal of biomechanics*, **41**(5):1086–94, January 2008. 53, 60

[119] D Brickley-Parsons and M J Glimcher. **Is the chemistry of collagen in intervertebral discs an expression of Wolffs Law? A study of the human lumbar spine**. *Spine*, **9**(2):148–163, 1984. 62

[120] E W Hsu and L A Setton. **Diffusion tensor microscopy of the intervertebral disc anulus fibrosus.** *Magnetic Resonance in Medicine*, **41**(5):992–999, 1999. 63

[121] M A Adams, P Pollintine, J H Tobias, G K Wakley, and P Dolan. **Intervertebral Disc Degeneration Can Predispose to Anterior Vertebral Fractures in the Thoracolumbar Spine**. *Journal of Bone and Mineral Research*, **21**(9), 2006. 67

[122] A Fritsch and C Hellmich. **'Universal' microstructural patterns in cortical and trabecular, extracellular and extravascular bone materials: micromechanics-based prediction of anisotropic elasticity.** *Journal of theoretical biology*, **244**(4):597–620, February 2007. 68, 69, 70, 74, 75, 77, 87, 93

[123] J L Katz, H S Yoon, S Lipson, R Maharidge, A Meunier, and P Christel. **The effects of remodeling on the elastic properties of bone.** *Calcified Tissue International*, **36 Suppl 1**:S31–S36, 1984. 68

[124] A Boyde and S J Jones. **Scanning Electron Microscopic Studies of the Formation of Mineralized Tissues**. In H C Slavkin and L A Bavetta, editors, *The Developmental Aspects of Oral Biology*, chapter 11, page 426. Academic Press, 1972. 69

REFERENCES

[125] S Weiner and H D Wagner. **The material bone: Structure mechanical function relations**. *Annual Review of Materials Science*, **28**:271–298, 1998. 69, 74

[126] G E Fantner, O Rabinovych, G Schitter, P J Thurner, J H Kindt, M Finch, J C Weaver, L S Golde, D E Morse, E A Lipman, I W Rangelow, and P K Hansma. **Hierarchical interconnections in the nano-composite material bone: fibrillar cross-links resist fracture on several length scales**. *Composites Science and Technology*, **66**(9):1205–1211, 2006. 69

[127] A J Fields, G L Lee, and T M Keaveny. **Mechanisms of initial endplate failure in the human vertebral body.** *Journal of Biomechanics*, **43**(16):3126–3131, 2010. 69

[128] C Hellmich, F J Ulm, and L Dormieux. **Can the diverse elastic properties of trabecular and cortical bone be attributed to only a few tissue-independent phase properties and their interactions? Arguments from a multiscale approach.** *Biomechanics and modeling in mechanobiology*, **2**(4):219–38, June 2004. 69

[129] G Boivin and P J Meunier. **The degree of mineralization of bone tissue measured by computerized quantitative contact microradiography.** *Calcified Tissue International*, **70**(6):503–511, 2002. 70, 93

[130] J K Weaver. **The microscopic hardness of bone.** *The Journal of Bone and Joint Surgery*, **48**(2):273–288, 1966. 70

[131] C E Hoffler, K E Moore, K Kozloff, P K Zysset, and S A Goldstein. **Age, gender, and bone lamellae elastic moduli.** *Journal of Orthopaedic Research*, **18**(3):432–437, 2000. 70

[132] J Y Rho, P Zioupos, J D Currey, and G M Pharr. **Microstructural elasticity and regional heterogeneity in human femoral bone of various ages examined by nano-indentation.** *Journal of Biomechanics*, **35**(2):189–198, 2002. 70

[133] E Schoenau, C M Neu, F Rauch, and F Manz. **Gender-specific pubertal changes in volumetric cortical bone mineral density at the proximal radius.** *Bone*, **31**(1):110–113, 2002. 70

[134] C Bergot, Y Wu, E Jolivet, L Q Zhou, J D Laredo, and V Bousson. **The degree and distribution of cortical bone mineralization in the human femoral shaft change with age and sex in a microradiographic study.** *Bone*, **45**(3):435–442, 2009. 70

[135] P Roschger, H S Gupta, A Berzlanovich, G Ittner, D W Dempster, P Fratzl, F Cosman, M Parisien, R Lindsay, J W Nieves, and K Klaushofer. **Constant mineralization density distribution in cancellous human bone.** *Bone*, **32**(3):316–323, 2003. 70

[136] J Vuong and C Hellmich. **Bone fibrillogenesis and mineralization: Quantitative analysis and implications for tissue elasticity.** *Journal of Theoretical Biology*, **287**(1):115–130, 2011. 70, 71, 75, 77, 78, 79, 87, 93

[137] R B Ashman, S C Cowin, W C Van Buskirk, and J C Rice. **A Continuous Wave Technique for the Measurement of the Elastic Properties of Cortical Bone**. *Journal of biomechanics*, **1**(5):349–361, 1984. 70

[138] R P Widmer and S J Ferguson. **On the interrelationship of permeability and structural parameters of vertebral trabecular bone: a parametric computational study**. *Computer Methods in Biomechanics and Biomedical Engineering*, **[Epub ahead of print]**. 72, 96

[139] J M Carcione. *Wave fields in Real Media: Wave Propagation in Anisotropic, Anelastic and Porous media (first edition)*. Elsevier, 2001. 72, 74

[140] C Kohlhauser, C Hellmich, C Vitale-Brovarone, A R Boccaccini, A Rota, and J Eberhardsteiner. **Ultrasonic Characterisation of Porous Biomaterials Across Different Frequencies**. *Strain*, **45**(1):34–44, February 2009. 73

[141] A Zaoui. **Continuum Micromechanics˜: Survey**. *Journal of Engineering Mechanics*, **128**(8):808–816, 2002. 74, 75, 76, 79, 81

[142] R Hill. **Elastic properties of reinforced solids: some theoretical principles**. *Journal of the Mechanics and Physics of Solids*, **11**(Hill 1962):357–372, 1963. 75

[143] J D Eshelby. **The Determination of the Elastic Field of an Ellipsoidal Inclusion, and Related Problems**. *Proceedings of the Royal Society A: Mathematical, Physical and Engineering Sciences*, **241**(1226):376–396, August 1957. 75, 79

[144] C Hellmich and F J Ulm. **Drained and Undrained Poroelastic Properties of Healthy and Pathological Bone: A Poro-Micromechanical Investigation**. *Transport in Porous Media*, **58**(3):243–268, March 2005. 76, 80, 81, 82, 83, 94

[145] S Lees. **Considerations regarding the structure of the mammalian mineralized osteoid from viewpoint of the generalized packing model.** *Connective Tissue Research*, **16**(4):281–303, 1987. 77

[146] S Lees, M Pineri, and M Escoubes. **A generalized packing model for type I collagen**. *International Journal of Biological Macromolecules*, **6**(3):133–136, 1984. 77

[147] A J Hodge and A J Petruska. **Recent studies with the electron microscope on ordered aggregates of the tropocollagen molecule**. In G N Ramachandran, editor, *Aspects of Protein Chemistry*, pages 289–300. Academic Press, 1963. 77

[148] J L Katz and K Ukraincik. **On the anisotropic elastic properties of hydroxyapatite.** *Journal of Biomechanics*, **4**(3):221–227, 1971. 78

[149] S Cusack and A Miller. **Determination of the Elastic Constants of Collagen by Brillouin Light Scattering**. *Journal of Molecular Biology*, **135**:39–51, 1979. 78

[150] C Hellmich, C Kober, and B Erdmann. **Micromechanics-based conversion of CT data into anisotropic elasticity tensors, applied to FE simulations of a mandible.** *Annals of biomedical engineering*, **36**(1):108–22, January 2008. 78, 79, 83, 97

[151] T Mori and K Tanaka. **Average stress in matrix and average elastic energy of materials with misfitting inclusions**. *Acta Metallurgica*, **21**(5):571–574, 1973. 79

[152] J L Auriault and E Sanchez-Palencia. **Etude du comportement macroscopique d'un milieu poreux saturé déformable**. *Journal de Mécanique*, **16**(4):575–603, 1977. 80

[153] X Chateau and L Dormieux. **Micromechanics of saturated and unsaturated porous media**. *International Journal for Numerical and Analytical Methods in Geomechanics*, **26**(8):831–844, 2002. 80

[154] O Coussy. *Poromechanics*. Wiley, 2004. 82, 83

[155] S C Cowin. *Bone Mechanics Handbook*. CRC Press, 2001. 86, 94, 96

[156] S Lees and K Prostak. **The locus of mineral crystallites in bone.** *Connective Tissue Research*, **18**(1):41–54, 1988. 93

[157] M A Rubin and I Jasiuk. **The TEM characterization of the lamellar structure of osteoporotic human trabecular bone.** *Micron Oxford England 1993*, **36**(7-8):653–664, 2005. 93

[158] L C Bonar, S Lees, and H A Mook. **Neutron diffraction studies of collagen in fully mineralized bone.** *Journal of Molecular Biology*, **181**(2):265–270, 1985. 93

[159] T Brynk, C Hellmich, A Fritsch, P Zysset, and J Eberhardsteiner. **Experimental poromechanics of trabecular bone strength: role of Terzaghi's effective stress and of tissue level stress fluctuations.** *Journal of Biomechanics*, **44**(3):501–508, 2011. 94

[160] K Tai, M Dao, S Suresh, A Palazoglu, and C Ortiz. **Nanoscale heterogeneity promotes energy dissipation in bone.** *Nature Materials*, **6**(6):454–462, 2007. 94

[161] A Nur and J D Byerlee. **An exact effective stress law for elastic deformation of rock with fluids**. *Journal of Geophysical Research*, **76**(26):6414–6419, 1971. 94

[162] T H Smit, J M Huyghe, and S C Cowin. **Estimation of the poroelastic parameters of cortical bone.** *Journal of biomechanics*, **35**(6):829–35, June 2002. 94

[163] T H Lim and J H Hong. **Poroelastic properties of bovine vertebral trabecular bone.** *Journal of orthopaedic research : official publication of the Orthopaedic Research Society*, **18**(4):671–7, July 2000. 94, 95

[164] M J Grimm and J L Williams. **Measurements of permeability in human calcaneal trabecular bone**. *Journal of Biomechanics*, **30**(7):743–745, 1997. 95

[165] P W Hui, P C Leung, and A Sher. **Fluid conductance of cancellous bone graft as a predictor for graft-host interface healing.** *Journal of Biomechanics*, **29**(1):123–132, 1996. 95

[166] A J Beaudoin, W M Mihalko, and W R Krause. **Finite element modelling of polymethylmethacrylate flow through cancellous bone.** *Journal of Biomechanics*, **24**(2):127–136, 1991. 95

[167] Z Yosibash, N Trabelsi, and C Hellmich. **Subject-Specific p-FE Analysis of the Proximal Femur Utilizing Micromechanics-Based Material Properties**. *International Journal for Multiscale Computational Engineering*, **6**(5):483–498, 2008. 97

[168] S R S Bibby, D A Jones, R M Ripley, and J P G Urban. **Metabolism of the intervertebral disc: effects of low levels of oxygen, glucose, and pH on rates of energy metabolism of bovine nucleus pulposus cells.** *Spine*, **30**(5):487–96, March 2005. 100, 105, 106

[169] J P G Urban, S Holm, A Maroudas, and A Nachemson. **Nutrition of the intervertebral disc: effect of fluid flow on solute transport**. *Clinical Orthopaedics and Related Research*, **170**(170):296, 1982. 100, 128

[170] M M Katz, A R Hargens, and S R Garfin. **Intervertebral disc nutrition: diffusion versus convection**. *Clinical orthopaedics and related research*, **210**(210):243–245, 1986. 100, 128

[171] R Arun, B J C Freeman, B E Scammell, D S McNally, E Cox, and P Gowland. **2009 ISSLS Prize Winner: What influence does sustained mechanical load have on diffusion in the human intervertebral disc?: an in vivo study using serial postcontrast magnetic resonance imaging.** *Spine*, **34**(21):2324–2337, 2009. 100

[172] E M Bartels, J C T Fairbank, C P Winlove, and J P G Urban. **Oxygen and lactate concentrations measured in vivo in the intervertebral discs of patients with scoliosis and back pain**. *Spine*, **23**(1):1–7, 1998. 100, 112, 122, 123, 127

[173] D M Soukane, A Shirazi-Adl, and J P G Urban. **Analysis of Nonlinear Coupled Diffusion of Oxygen and Lactic Acid in Intervertebral Discs**. *Journal of Biomechanical Engineering*, **127**(7):1121, 2005. 100, 106

[174] E Sélard, A Shirazi-Adl, and J P G Urban. **Finite element study of nutrient diffusion in the human intervertebral disc.** *Spine*, **28**(17):1945–53; discussion 1953, September 2003. 100

[175] C Y Huang and W Y Gu. **Effects of mechanical compression on metabolism and distribution of oxygen and lactate in intervertebral disc.** *Journal of biomechanics*, **41**(6):1184–96, January 2008. 100, 122, 128

[176] C Magnier, O Boiron, S Wendling-Mansuy, P Chabrand, and V Deplano. **Nutrient distribution and metabolism in the intervertebral disc in the unloaded state: a parametric study.** *Journal of biomechanics*, **42**(2):100–8, January 2009. 100, 106, 122

[177] D Mokhbi Soukane, A Shirazi-Adl, and J P G Urban. **Investigation of solute concentrations in a 3D model of intervertebral disc.** *European spine journal : official publication of the European Spine Society, the European Spinal Deformity Society, and the European Section of the Cervical Spine Research Society*, **18**(2):254–62, February 2009. 100, 122, 131

REFERENCES

[178] A R Jackson, C Y Huang, M D Brown, and W Y Gu. **3D Finite Element Analysis of Nutrient Distributions and Cell Viability in the Intervertebral Disc: Effects of Deformation and Degeneration.** *Journal of Biomechanical Engineering*, **133**(9):091006, 2011. 100, 129

[179] B Vernon-Roberts, R J Moore, and R D Fraser. **The natural history of age-related disc degeneration: the influence of age and pathology on cell populations in the L4-L5 disc.** *Spine*, **33**(25):2767–73, December 2008. 101, 127, 130

[180] D W McMillan, G Garbutt, and M A Adams. **Effect of sustained loading on the water content of intervertebral discs: implications for disc metabolism.** *Annals of the rheumatic diseases*, **55**(12):880–7, December 1996. 101

[181] C L Korecki, J J MacLean, and J C Iatridis. **Dynamic Compression Effects on Intervertebral Disc Mechanics and Biology**. *Spine*, **33**(13):1403–1409, 2008. 101, 127

[182] K Wuertz, K Godburn, and J C Iatridis. **Biochemical and Biophysical Research Communications MSC response to pH levels found in degenerating intervertebral discs**. *Biochemical and Biophysical Research Communications*, **379**(4):824–829, 2009. 102, 110, 111

[183] H A Horner and J P Urban. **2001 Volvo Award Winner in Basic Science Studies: Effect of nutrient supply on the viability of cells from the nucleus pulposus of the intervertebral disc.** *Spine*, **26**(23):2543–9, December 2001. 102, 105, 112, 113, 114, 124, 129

[184] S R S Bibby and J P G Urban. **Effect of nutrient deprivation on the viability of intervertebral disc cells.** *European spine journal official publication of the European Spine Society the European Spinal Deformity Society and the European Section of the Cervical Spine Research Society*, **13**(8):695–701, 2004. 102, 113, 129

[185] J Crank. *The mathematics of diffusion*, **16**. Oxford University Press, 1975. 103

[186] R W Roland W Lewis, P Nithiarasu, and K N Seetharamu. *Fundamentals of the finite element method for heat and fluid flow*. John Wiley & Sons Inc, 2004. 103

[187] C C Yu and J C Heinrich. **Petrov–Galerkin methods for the time-dependent convective transport equation**. *International Journal for Numerical Methods in Engineering*, **23**(5):883–901, 1986. 104

[188] A N Brooks and T J R Hughes. **Streamline upwind/Petrov-Galerkin formulations for convection dominated flows with particular emphasis on the incompressible Navier-Stokes equations**. *Computer Methods in Applied Mechanics and Engineering*, **32**(1-3):199–259, 1982. 104, 115, 116

[189] P H Feenstra and C A Taylor. **Drug transport in artery walls: a sequential porohyperelastic–transport approach.** *Computer methods in biomechanics and biomedical engineering*, **12**(3):263–76, June 2009. 105

[190] J S Mackie and P Meares. **The Diffusion of Electrolytes in a Cation-Exchange Resin Membrane. I. Theoretical**. *Proceedings of the Royal Society of London. Series A: Mathematical and physical sciences*, **232**(1191):498–509, November 1955. 105

[191] J S Mackie and P Meares. **The Diffusion of Electrolytes in a Cation-Exchange Resin Membrane. II. Experimental**. *Proceedings of the Royal Society A Mathematical Physical and Engineering Sciences*, **232**(1191):510–518, 1955. 105

[192] H E Gruber and E N Hanley. **Analysis of aging and degeneration of the human intervertebral disc. Comparison of surgical specimens with normal controls.** *Spine*, **23**(7):751–757, 1998. 110

[193] R M Dillaman, R D Roer, and D M Gay. **Fluid movement in bone: theoretical and empirical.** *Journal of Biomechanics*, **24 Suppl 1**(Suppl. 1):163–177, 1991. 110

[194] C M Whyne, S S Hu, and J C Lotz. **Parametric finite element analysis of vertebral bodies affected by tumors.** *Journal of biomechanics*, **34**(10):1317–24, October 2001. 111

[195] S Holm, A Maroudas, J P G Urban, G Selstam, and A Nachemson. **Nutrition of the Intervertebral Disc: Solute Transport and Metabolism**. *Connective Tissue Research*, **8**(2):101–119, January 1981. 112, 122

[196] A Ejeskär and S Holm. **Oxygen tension measurements in the intervertebral disc. A methodological and experimental study.** *Upsala Journal of Medical Sciences*, **84**(1):83–93, 1979. 112, 122

[197] L Weng, S Liang, L Zhang, X Zhang, and J Xu. **Transport of Glucose and Poly(ethylene glycol)s in Agarose Gels Studied by the Refractive Index Method**. *Macromolecules*, **38**(12):5236–5242, 2005. 113

[198] W Y Gu, H Yao, A L Vega, and D Flagler. **Diffusivity of ions in agarose gels and intervertebral disc: effect of porosity.** *Annals of biomedical engineering*, **32**(12):1710–7, December 2004. 113

[199] L Xikui and W Wenhua. **Characteristic Galerkin Method For Cconvection-Diffusion Equations And Implicit Algorithm Using Precise Integration**. *Acta Mechanica Sinica*, **15**(4):371–382, 1999. 116

[200] D J Botsford, S I Esses, and D J Ogilvie-Harris. **In vivo diurnal variation in intervertebral disc volume and morphology**. *Spine*, 1994. 128

[201] H Miyamoto, M Doita, K Nishida, T Yamamoto, M Sumi, and M Kurosaka. **Effects of cyclic mechanical stress on the production of inflammatory agents by nucleus pulposus and anulus fibrosus derived cells in vitro.** *Spine*, **31**(1):4–9, 2006. 129

[202] R L Mauck, C T Hung, and G A Ateshian. **Modeling of Neutral Solute Transport in a Dynamically Loaded Porous Permeable Gel: Implications for Articular Cartilage Biosynthesis and Tissue Engineering**. *Journal of Biomechanical Engineering*, **125**(5):602, 2003. 133

[203] P Royer and F Cherblanc. **Homogenisation of advectivediffusive transport in poroelastic media**. *Mechanics Research Communications*, **37**(2):133–136, March 2010. 133